

A083950

LEVEL

SGI-R-79-012

6

SEISMIC AMPLITUDE
AND WAVEFORM RESEARCH

R. S. HART
D. M. HADLEY
G. R. MELLMAN
R. BUTLER

DTIC
ELECTED
APR 30 1980

FINAL TECHNICAL REPORT

SPONSORED BY

DEFENSE ADVANCED RESEARCH PROJECTS AGENCY (DOD)
ARPA ORDER No. 2551

This research was supported by the Advanced Research Projects Agency of the Department of Defense and was monitored by AFTAC/VSC, Patrick AFB, FL 32925, under Contract No. F08606-79-C-0009.

The views and conclusions contained in this document are those of the authors and should not be interpreted as necessarily representing the official policies, either expressed or implied, of the Advanced Research Projects Agency, the Air Force Technical Applications Center, or the United States Government.

APPROVED FOR PUBLIC RELEASE, DISTRIBUTION UNLIMITED

October 1979



SIERRA GEOPHYSICS, INC.

150 N. SANTA ANITA AVENUE • ARCADIA, CALIFORNIA 91006 • (213) 574-7052

80 4 28 120

FILE COPY

AFTAC Project Authorization: VT/9710

ARPA Order: 2551

Effective Date of Contract: November 22, 1978

Contract Expiration Date: September 30, 1979

Contract No: F08606-79-0009

Principal Investigators and Phone No:

Dr. Robert S. Hart

Dr. David M. Hadley

Dr. Rhett Butler

(213) 574-7052

Program Manager and Phone No:

Mr. Michael J. Shore

(202) 325-7581

C6

SEISMIC AMPLITUDE
AND WAVEFORM RESEARCH

R. S. HART
D. M. HADLEY
G. R. MELLMAN
R. BUTLER

DTIC
ELECTR
APR 3 1980

FINAL TECHNICAL REPORT

SPONSORED BY

DEFENSE ADVANCED RESEARCH PROJECTS AGENCY (DOD)

ARPA ORDER No. 2551

This research was supported by the Advanced Research Projects Agency of the Department of Defense and was monitored by AFTAC/VSC, Patrick AFB, FL 32925, under Contract No. F08606-79-C-0009.

The views and conclusions contained in this document are those of the authors and should not be interpreted as necessarily representing the official policies, either expressed or implied, of the Advanced Research Projects Agency, the Air Force Technical Applications Center, or the United States Government.

APPROVED FOR PUBLIC RELEASE, DISTRIBUTION UNLIMITED

October 1979

UNCLASSIFIED

SECURITY CLASSIFICATION OF THIS PAGE (When Data Entered)

REPORT DOCUMENTATION PAGE		READ INSTRUCTIONS BEFORE COMPLETING FORM
1. REPORT NUMBER	2. GOVT ACCESSION NO.	3. RECIPIENT'S CATALOG NUMBER
	AD-A083 950	
4. TITLE (and Subtitle)	5. TYPE OF REPORT & PERIOD COVERED	
Seismic Amplitude and Waveform Research,	(9) Final Report	
	6. PERFORMING ORG. REPORT NUMBER	
	(14) SGI-R-79-012	
7. AUTHOR(s)	8. CONTRACT OR GRANT NUMBER(s)	
R. S. Hart, D. M. Hadley, G. R. Mellman, R. Butler	(15) F08606-79-0009 C-0009 ARPA Order-2551	
9. PERFORMING ORGANIZATION NAME AND ADDRESS	10. PROGRAM ELEMENT, PROJECT, TASK AREA & WORK UNIT NUMBERS	
Sierra Geophysics, Inc. / 150 N. Santa Anita Ave. Arcadia, CA. 91006	(12) 183 L ARPA Order No. 2551	
11. CONTROLLING OFFICE NAME AND ADDRESS	12. REPORT DATE	
VELA Seismological Center 312 Montgomery Street Alexandria, Virginia 22314	October 25, 1979	
14. MONITORING AGENCY NAME & ADDRESS (if different from Controlling Office)	13. NUMBER OF PAGES	
(11) 25 Oct 79		
	15. SECURITY CLASS. (of this report)	
	393821	
	15a. DECLASSIFICATION DOWNGRADING SCHEDULE	
16. DISTRIBUTION STATEMENT (of this Report)		
Approved for public release, distribution unlimited.		
17. DISTRIBUTION STATEMENT (of the abstract entered in Block 20, if different from Report)		
(10) Robert S. Hart David M. Hadley G. R. Mellman Rhett Butler		
18. SUPPLEMENTARY NOTES		
19. KEY WORDS (Continue on reverse side if necessary and identify by block number)		
Underground Nuclear Explosions Seismic Source Functions Attenuation Body Waves Frequency Dependent Q		
20. ABSTRACT (Continue on reverse side if necessary and identify by block number)		
<p>This technical report summarizes the research done in a 12 month program directed toward understanding observed m_b and yield biases at the Nevada Test Site. This program has necessarily included work on seismic source functions, variations in attenuation, frequency dependence of Q, regional amplitude and waveform variations, and shallow structural influences on seismic wave propagation. The report is divided into six sections, each describing an individual research effort on one or more of these issues. — to p. i</p>		

DD FORM 1 JAN 73 1473

EDITION OF 1 NOV 65 IS OBSOLETE

UNCLASSIFIED

SECURITY CLASSIFICATION OF THIS PAGE (When Data Entered)

TABLE OF CONTENTS

	<u>Page</u>
Introduction	1
(I.) Seismic Source Functions and Attenuation from Observations of Pahute Mesa Events ;	3
(II.) Observational Studies of the Piledriver and Hard Hat Tests ;	5
(III.) Frequency Dependence of Seismic Attenuation: A Mechanism to Unite Amplitude and Spectral Ratio Techniques ;	7
IV. Estimation of Receiver Functions for Stations Located at the NTS ;	24
4.1 Theory	24
4.2 Application to Data	30
4.3 Interpretation of the YF Receiver Functions	48
V. Studies of Outgoing Seismic Energy from Yucca Flats, NTS ; and	54
VI. Amplitude Studies of the Stations OB2, RKON and HNME Relative to the WWSSN Mean	62
References	97

Acquisition For	
NTIS Grant	<input checked="" type="checkbox"/>
DOC TAB	<input type="checkbox"/>
U. S. Army and	<input type="checkbox"/>
Joint Staff	
By	
Distribution/	
Availability Codes	
Dist	Station/or Special
A	

INTRODUCTION

During the past ten months, Sierra Geophysics has been conducting a research program aimed at understanding the m_b biases observed for underground tests located at the Nevada Test Site (NTS). This report summarizes this ARPA-supported research which was monitored by AFTAC/VSC.

The research program was divided into three principal tasks. The first task was an analysis of both incoming and outgoing seismic energy at NTS to determine how the waveforms are affected by local geologic structure and intrinsic attenuation. The second task involved a theoretical analysis of wave propagation with models representing the complex, three-dimensional structure at the NTS. The final task was to combine the results of the first two tasks and to estimate the sensitivity of the data to variations in the structural model for the region or parts of the region.

The program summarized in this report does not represent a final answer to the question of NTS m_b bias. Additional work on this problem, including the acquisition and integration of seismic data from other Special Data Collection Systems (SDCS) stations (NT-NV, GQ-NV, etc.) and the inclusion of additional structural information (expected shortly from studies by Herrin), is needed.

This report is divided into six sections. The first two sections summarize research on teleseismic source functions appropriate for NTS events and on teleseismic attenuation measurements. These first two summaries have been extracted from the Quarterly Reports SGI-R-79-002 and SGI-R-79-003. The third section deals with on-going studies of the frequency dependence of seismic attenuation and the implications for yield

determination and discrimination. The fourth section discusses research conducted on both incoming seismic energy recorded by the SDCS stations at Yucca Flats and at Climax Stock and outgoing energy from tests at Yucca Flats. The fifth section is a discussion of model studies of wave propagation at Yucca Flats and a comparison of those results with the conclusions reached in the data analysis of the YF-NT data (Section IV). Finally, the last section reports on amplitude comparisons between the SDCS stations OB2-NV, RK-ON, and HN-ME and WWSSN stations within the continental United States.

distance the initial seismic energy represents diving rays and hence is suitable for comparison with more distant regional and teleseismic observations. Using a modified Von Seggern and Blandford (1972) source representation, and including near-field terms, it has been possible to obtain source functions which not only accurately model close-in records but also match teleseismic observations. Having once defined the explosion source description, it is a straightforward task to determine the effective t^* for teleseismic observations without the usual ambiguity of what are the source influences as opposed to the anelastic effects. For WWSSN short period observations of these events, we obtain an average t^* of about 1.3 for compressional waves with a scatter of about ± 0.2 . There are systematic azimuthal trends in the observed t^* values which are not strongly correlated with the Silent Canyon caldera but may be correlated with part of the central Rocky Mountains. It is not possible at this time to rule out systematic receiver function biases as the cause of the amplitude variations. A principal, although for present purposes not critical, limitation on the source function determination made in this study is the uncertainties in the precise crustal structure and seismological properties along the 8 km paths between the events and the strong motion sites. Since these uncertainties directly affect the resolved source function, this structure needs to be more precisely defined in the efforts to reduce the observed yield variations at NTS. A complete description of this research project is contained in the Sierra Geophysics Quarterly Technical Report "Seismic Source Functions and Attenuation from Local and Teleseismic Observations of the NTS Events Jorum and Handley" (SGI-R-79-002).

II. OBSERVATIONAL STUDIES OF THE PILEDRIVER AND HARD HAT TESTS

This study represents the second part of a project to define both the teleseismic path-averaged attenuation operator appropriate for sources located at NTS and the deviation from the average associated with distinct geologic structures. In section I of this report we summarized the first part of this program. In this section we summarize research on the Piledriver and Hard Hat tests conducted in granite at Climax Stock. A detailed description of this work may be found in the Sierra Geophysics Quarterly Technical Report "Seismic Studies of the Nevada Test Site," Section 3 (SGI-R-79-003).

In this study, we have tried to relate the near-field and teleseismic data for the test Piledriver (yield ~56 kt; Springer and Kinnaman, 1971). Data from a second event, Hard Hat (yield ~5.9 kt) were also examined as a check on the Piledriver results. Hard Hat was located within the Climax Stock and was separated in distance from Piledriver by about three hundred meters. Although this shot was much too small to be recorded by the WWSSN array, both Hard Hat and Piledriver were well recorded by the short period Benioff instruments operated in Southern California ($\Delta \sim 500$ km) by Caltech. This research project combined and interrelated near-field data from Piledriver, scaling relations for a 56 kt source, teleseismic waveforms from Piledriver, regional amplitude data from both Hard Hat and Piledriver and RDP's from Hard Hat. Unfortunately, these data sets are not internally consistent and the results must depend, to some extent, on which data are heavily weighted in the analysis.

If the velocity records recorded at the distances of 204 m and 470 m from Piledriver are employed to calculate an effective RDP for the source, we find that the teleseismic short period P waves predict a t^* of 1.3. However, some question remains as to the degree in which these near-field records have been contaminated by non-linear effects. The calculation of an effective RDP implicitly assumes that such contamination is negligible.

This source description was also compared via several source scaling techniques to the experience from other tests. On the basis of this comparison, the RDP strength derived from the close-in velocity records appears to be a factor of 2 too high. This factor is roughly equivalent to that obtained from a comparison of regional amplitude data recorded in southern California from the Hard Hat and Piledriver tests. The reduction in the RDP strength would reduce the predicted t^* from 1.3 to about 1.0. The present information does not provide a conclusive basis to decide which data set should be given the most weight. For periods of about 1 sec., the present data only constrain t^* to the range [1.0-1.3] for sources located at Climax Stock.

III. FREQUENCY DEPENDENCE OF SEISMIC ATTENUATION: A MECHANISM TO UNITE AMPLITUDE AND SPECTRAL RATIO TECHNIQUES

The attenuation of short-period body waves, commonly described by the parameter t^* (the ratio of travel time to Q), is an extremely important factor in both the detection problem and in the source description analysis of underground nuclear explosions. The attenuation of short period seismic energy has been the source of major controversy within the seismological community. A large part of the disagreements may be traced to differences in technique and the frequency bands being considered. The time domain determinations of t^* are dominated by .5 to 2 hertz energy, the frequency domain estimates have concentrated on higher frequencies and have resulted in smaller t^* values.

We have approached the problem of defining a useful attenuation model by first modeling the time domain waveforms, and then narrow-band filtering (center frequency = 1, 2, 4, Hz) the observations and the synthetics, and by comparing spectral amplitudes. This dual approach provides both a time domain and frequency domain check on the interpretations. This study was initiated primarily to investigate the trade-offs between the frequency behavior of the attenuation operator and absolute (M_b) amplitudes of synthetic teleseismic waveforms. The study to date has been necessarily limited to just five tests recorded at OB2, HNME and RKON. Within this report we will restrict the discussion to the simplest event and to just the RKON and HNME data. The generation of the synthetic seismograms requires a source description and a t^* operator. Following previous work, we have used a von Seggern and Blandford (1972) source parameterization

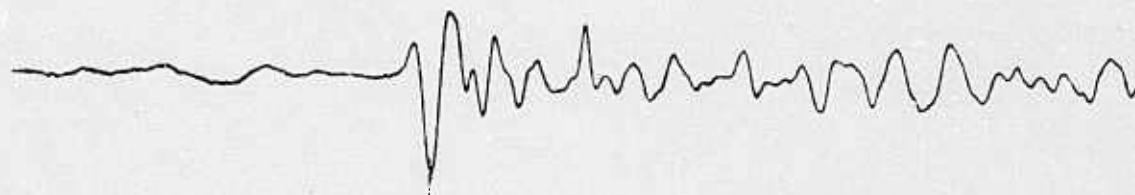
and have adjusted the rise time, on the basis of the Piledriver/Hard Hat/Shoal experience, to be approximately representative of a 100 Kt underground explosion (K-7.6).

Figures 1 and 2 show the raw seismograms (top traces) for a Russian underground explosion. This event was located at the Northern Novaya Zemlya test site and the date was September 1, 1977. Traces 2-4 are narrow band-passed (zero phase shifted) filtered records computed after the raw data were corrected for the instrument response. The log spectral amplitude plots, Figures 3 and 4, show the instrument corrected data. For HNME very little 4 Hz energy arrived at the P-wave onset. However, for RKON the 4 Hz energy arrived with the 1 sec P-wave. Next, synthetic seismograms were computed for these two records. The t^* chosen for each station was based on the observed amplitude variations for Russian underground explosions, i.e. $RKON/OB2 = 4$ and $HNME/OB2 = 1.7$ (see Section VI). Assuming $t^*_{OB2} = 1.3$, these observations approximately translate to $t^*_{RKON} \approx 0.65$ and $t^*_{HNME} \approx 1.05$. The pP reflection time was adjusted in order to obtain the best visual fit. Finally, the synthetics were superimposed on the noise preceeding the observed records and the resulting seismograms analyzed with the same program used on the actual data, Figures 5 and 7. Perhaps as expected, these synthetics visually fit the observations quite well. Note also that the chosen t^* values (and hence m_b) predict the observed amplitude ratios between RKON and HNME (data = 3.4, synthetics = 3.7). For HNME the amplitude observed in each frequency band is fairly consistent with the synthetic. The spectral plot, Figure 6, indicates that the synthetic is slightly depleted at frequencies around 3 Hz. However, the synthetics for RKON, Band 4 Hz, Figure 7, are down about a factor of five from the data. The spectral plot, Figure 8, shows that the discrepancy is somewhat larger than a full decade. Although this is only one example, significant

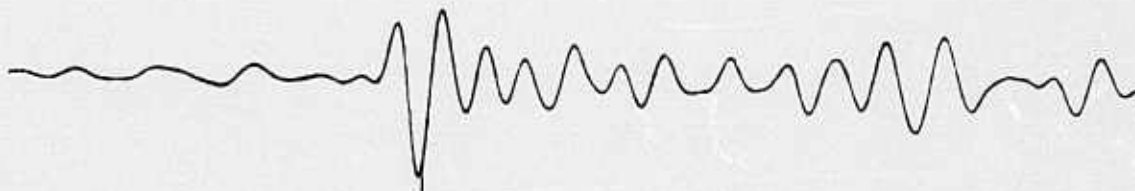
CODE: 770109HN-ME

XMAX= 100.812

RATIO



CENTER FREQUENCY: 1 HZ, XMAX= 79.453



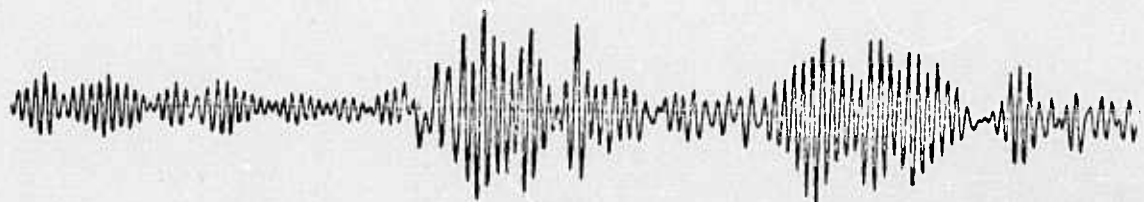
.79

CENTER FREQUENCY: 2 HZ, XMAX= 12.941



.13

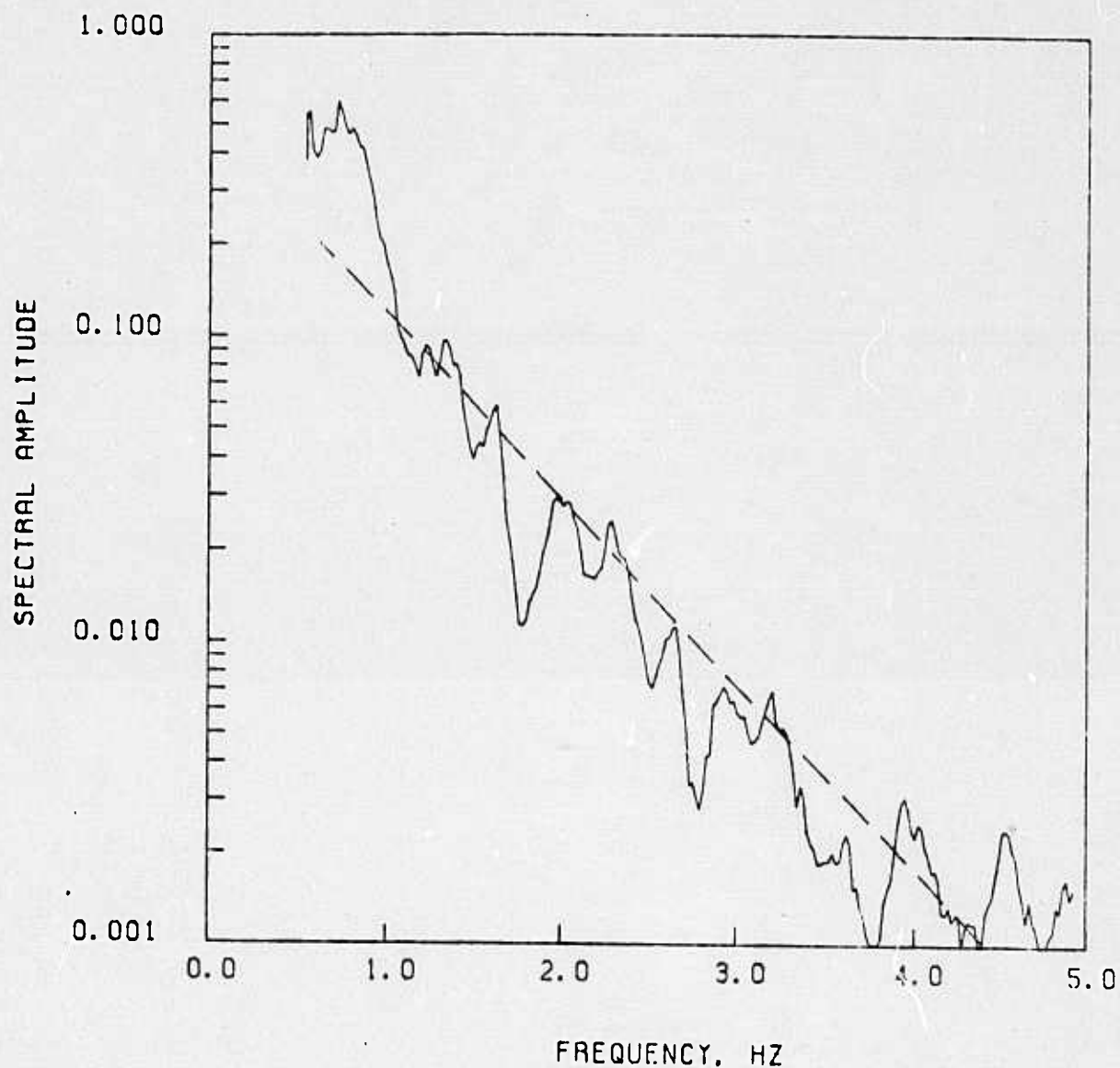
CENTER FREQUENCY: 4 HZ, XMAX= 0.521



.002-.005

Figure 1: Waveform recorded at HNME from a Russian test. The lower three traces have been narrow band-pass filtered after correcting the top trace for the instrument response. The ratio is the maximum amplitude of the filtered trace divided by the maximum of the recorded record.

LOG SPECTRUM PLOT: 770109HN-ME



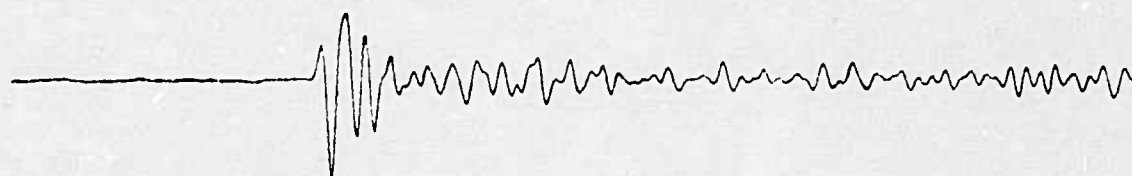
SLOPE=10. * * (-0.608)/HZ

Figure 2: Fourier transform of the trace shown at the top of Figure 1. The spectrum has been corrected for the instrument response. The dashed line is a least squares fit to the spectrum over the range [1.5-5 Hz].

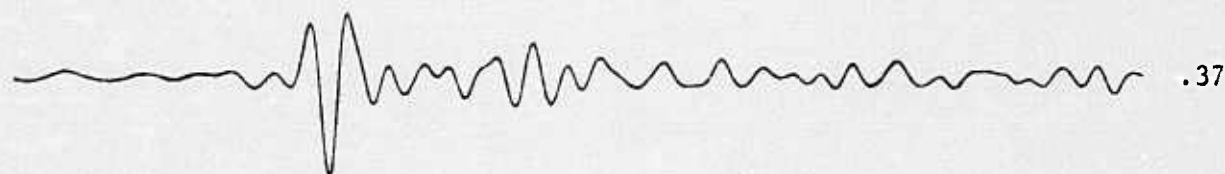
CODE: 770109RK-0N

XMAX= 342.566

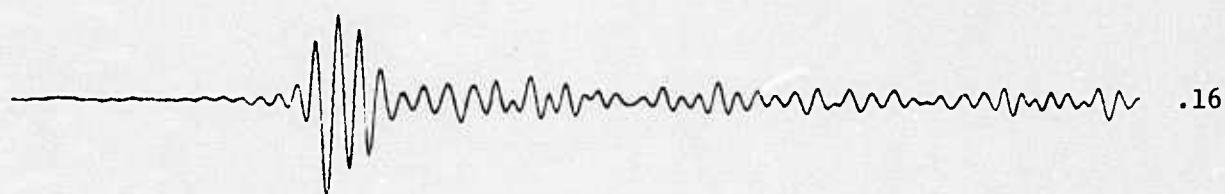
RATIO



CENTER FREQUENCY: 1 HZ. XMAX= 127.396



CENTER FREQUENCY: 2 HZ. XMAX= 55.931



CENTER FREQUENCY: 4 HZ. XMAX= 3.410

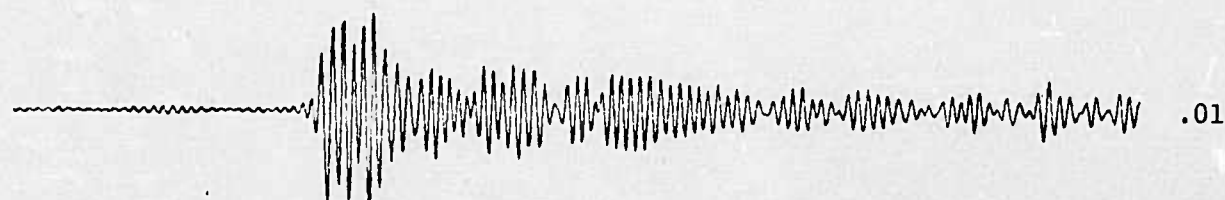
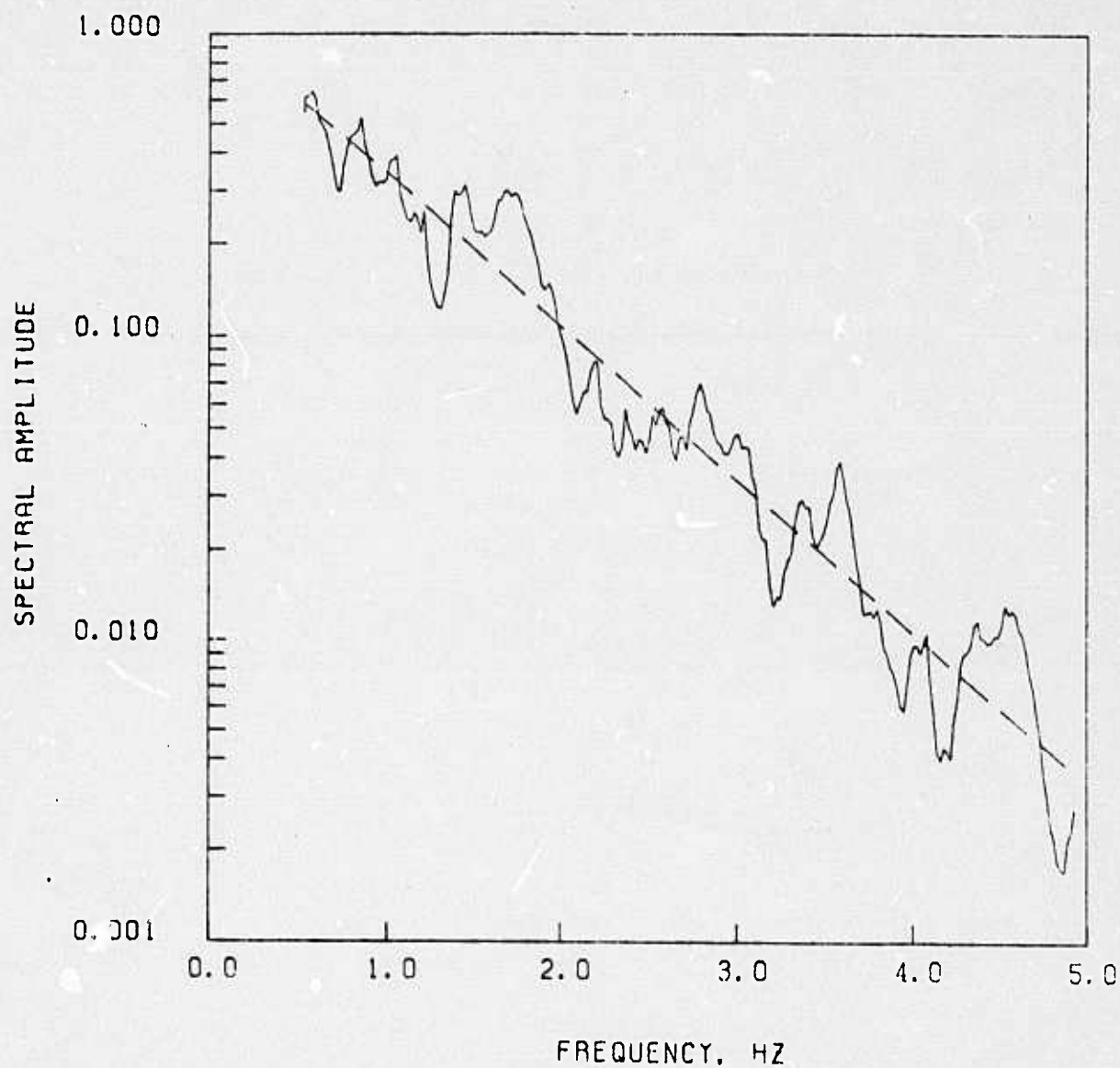


Figure 3: Waveform recorded at RKON from a Russian underground explosion.

LOG SPECTRUM PLOT: 770109RK-0N



SLOPE=10. ** (-0.500)/HZ

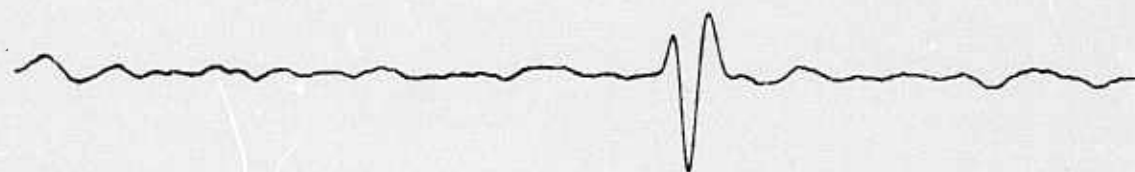
Figure 4: Fourier transform of the trace shown at the top of Figure 3.

15

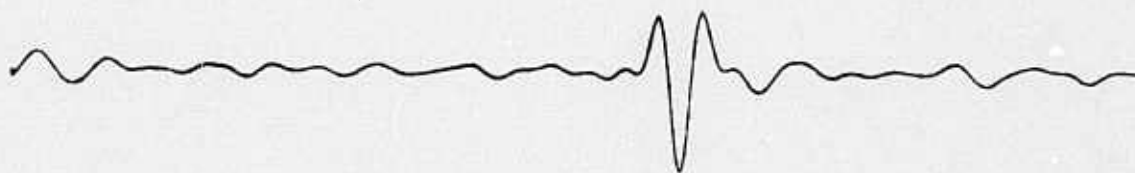
HNME-SYNTHETIC

XMAX= 89.027

RATIO



CENTER FREQUENCY: 1 HZ, XMAX= 73.732



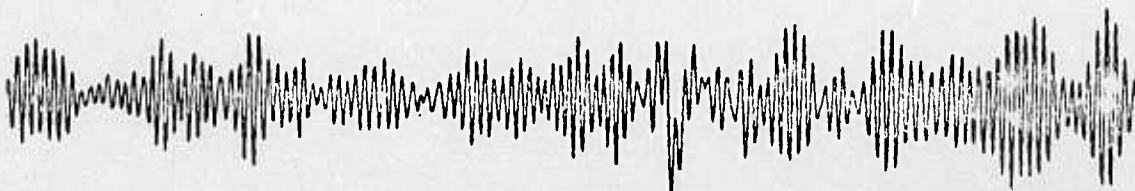
.82

CENTER FREQUENCY: 2 HZ, XMAX= 11.245



.125

CENTER FREQUENCY: 4 HZ, XMAX= 0.172



.002

Figure 5: Synthetic waveform for the record at HNME. The waveform has been added to the noise preceding the actual P-wave arrival at HNME. The synthetics were calculated with a von Seggern and Blandford source ($K=7.6$, $B=1.5$), t^* (independent of frequency) = 1.05 and pP was lagged .25 sec.

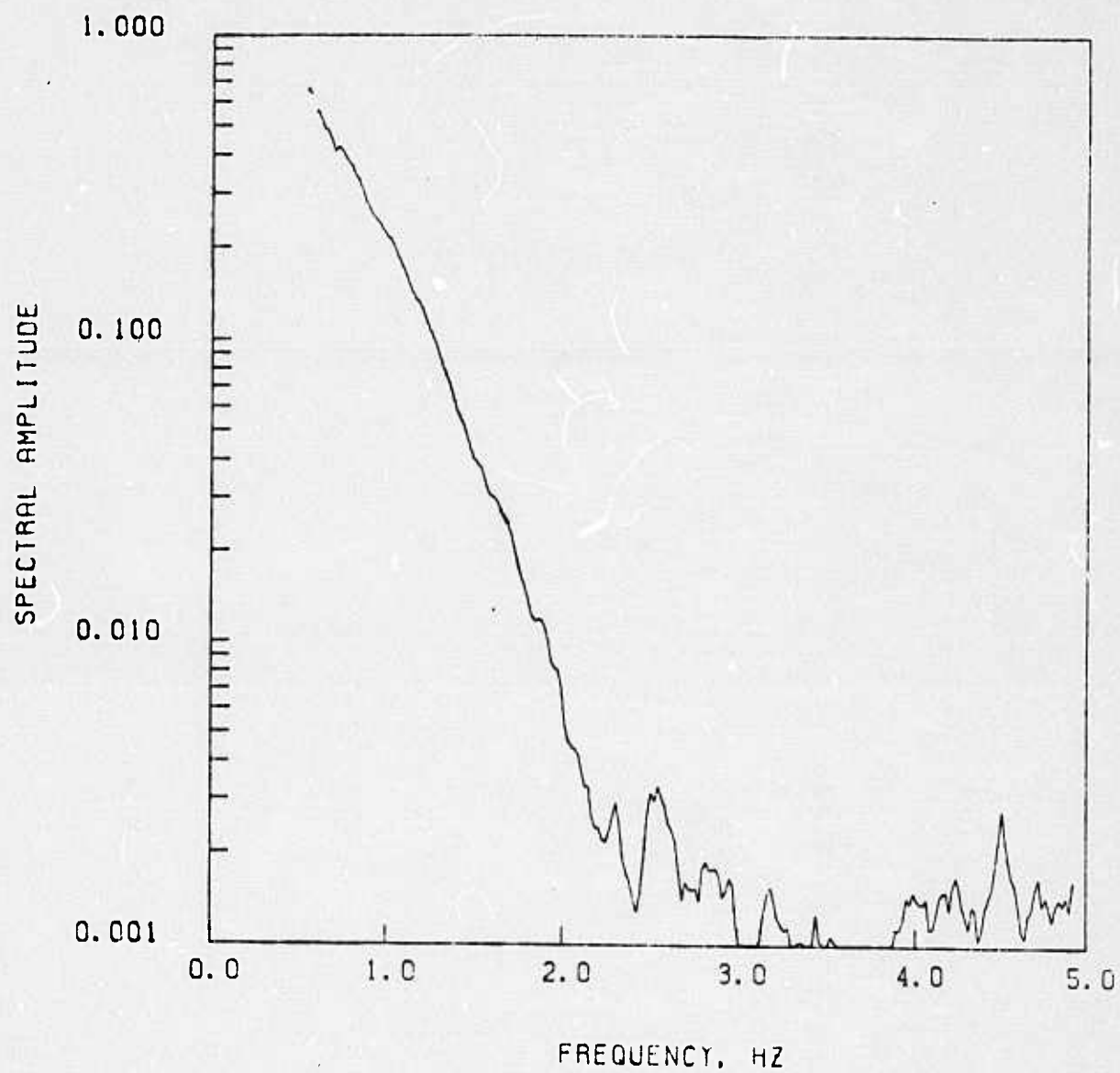


Figure 6: Fourier transform of the top trace shown on Figure 5.

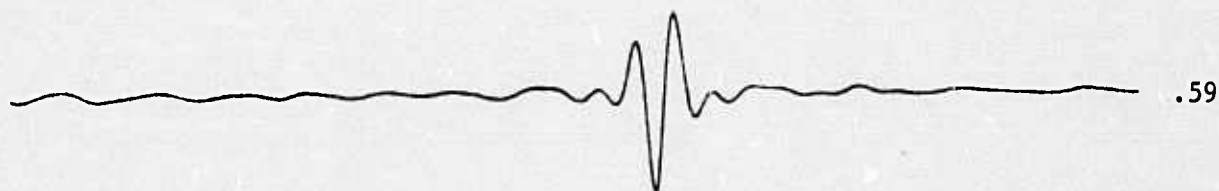
RKON-SYNTHETIC

XMAX= 329.170

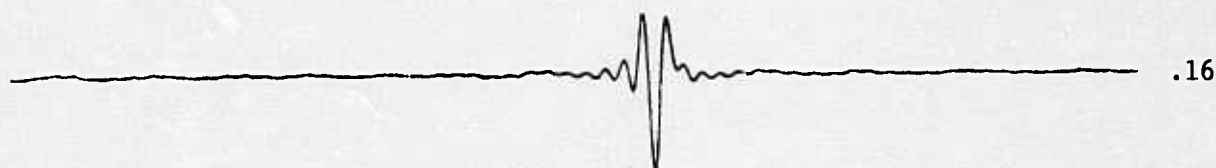
RATIO



CENTER FREQUENCY: 1 HZ. XMAX= 194.178



CENTER FREQUENCY: 2 HZ. XMAX= 52.890



CENTER FREQUENCY: 4 HZ. XMAX= 0.625

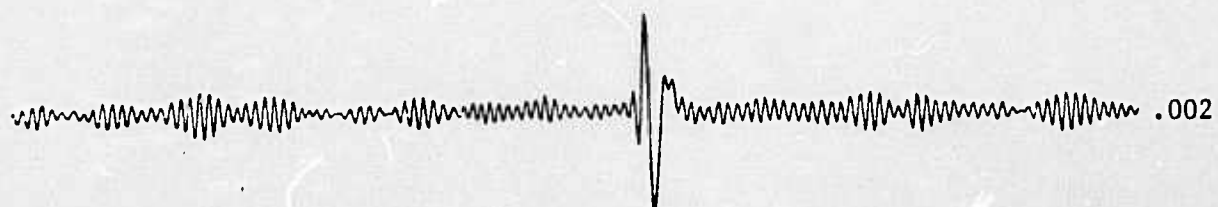


Figure 7:

Synthetic waveform for the record at RKON. The source model is identical to that described on Figure 5 $t^* = .65$.

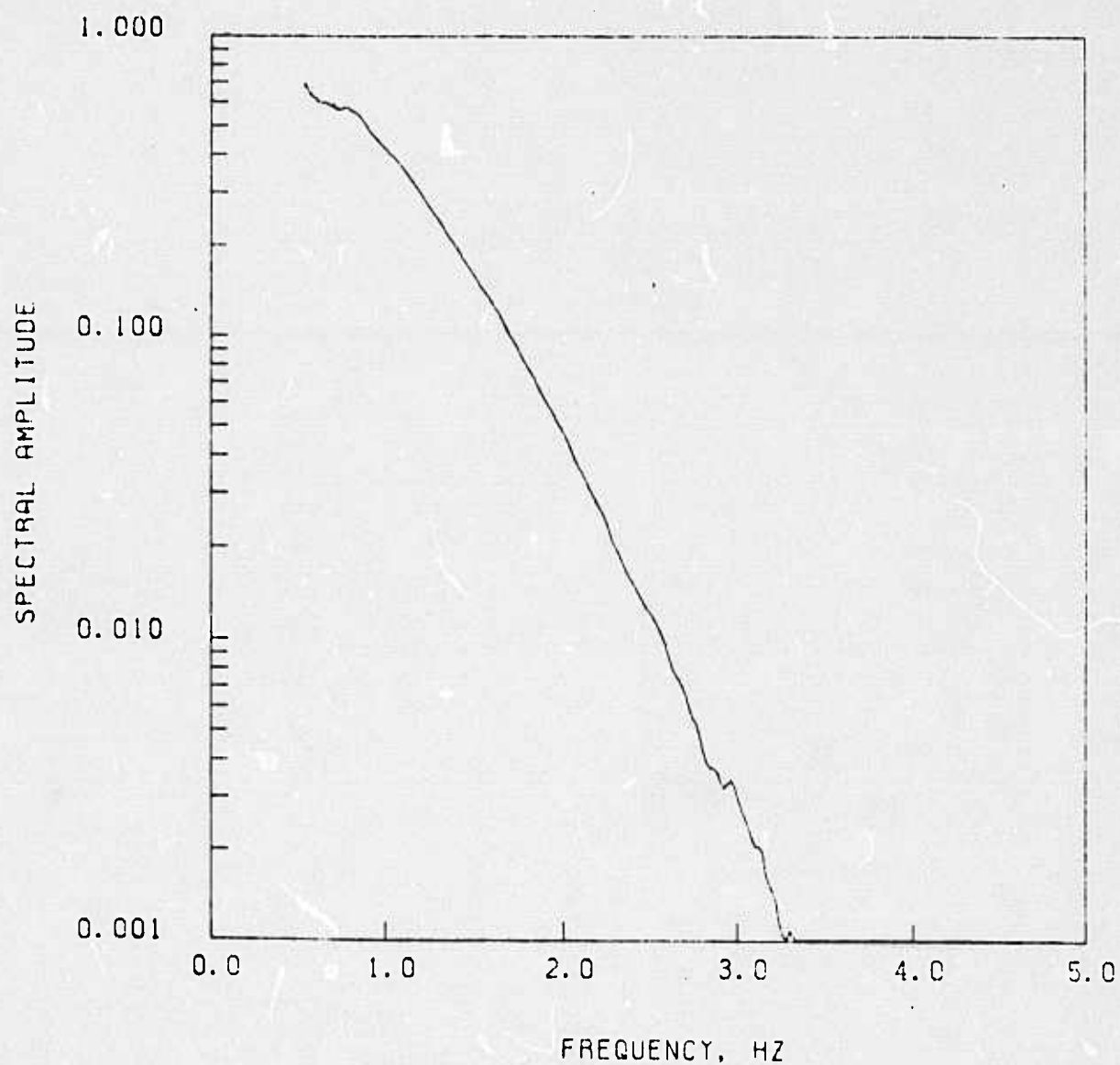


Figure 8: Fourier transform of the top trace shown on Figure 7.

4 Hz energy is routinely observed (Der and McElfresh, 1975). However, decreasing t^* to accommodate the 4 Hz data would strongly violate the observations at 1 sec. The RDP's at 1 sec are reasonably accurate and the teleseismic amplitudes require an operator with the characteristics described by $t^* \sim 1$. One reasonable compromise discussed by Liu, Anderson, and Kanamori (1976); Kanamori and Anderson (1977); Anderson, Kanamori, Hart, and Liu (1976); Anderson and Hart (1977, 1978); and Hart (1977) is to move the high frequency edge of the absorption band into the range 2.5 Hz. We have coded the Minster (1978a, b) description of an attenuation operator defined by an absorption band model. The relative spectral amplitudes of this operator as a function of τ_m ($\sim 1/2\pi f$), are shown in Figure 9. The attenuation for 5 possible positions of the absorption band and $t^* = 1.0$ are shown. Note that this range affects the 1 Hz data by about a factor of two but can potentially alter the 4 Hz data by many decades. For the data presented for RKON, moving the edge of the absorption band to about 2 Hz ($\tau \sim 0.08$) would more than account for the high frequency energy. As an example, synthetics for RKON ($t^* = .75$) and for HNME ($t^* = 1.15$) for $\tau_m = 0.08$ are shown in Figures 10 and 11. A comparison between either of the band-passed records or the spectral plots, Figures 12 and 13, and the actual data show that the synthetics now have too much high frequency energy. For this single example it seems that the position of the absorption band is not constant: HNME is fairly well modeled with $\tau_m \sim .001$ for RKON $\tau_m < 0.08$.

Currently there are two distinct methodologies in the analysis of seismic attenuation: Amplitude data from both short and long period

40

4 Hz energy is routinely observed (Der and McElfresh, 1975). However, decreasing t^* to accommodate the 4 Hz data would strongly violate the observations at 1 sec. The RDP's at 1 sec are reasonably accurate and the teleseismic amplitudes require an operator with the characteristics described by $t^* \sim 1$. One reasonable compromise discussed by Liu, Anderson, and Kanamori (1976); Kanamori and Anderson (1977); Anderson, Kanamori, Hart, and Liu (1976); Anderson and Hart (1977, 1978); and Hart (1977) is to move the high frequency edge of the absorption band into the range 2.5 Hz. We have coded the Minster (1978a, b) description of an attenuation operator defined by an absorption band model. The relative spectral amplitudes of this operator as a function of τ_m ($\sim 1/2\pi f$), are shown in Figure 9. The attenuation for 5 possible positions of the absorption band and $t^* = 1.0$ are shown. Note that this range affects the 1 Hz data by about a factor of two but can potentially alter the 4 Hz data by many decades. For the data presented for RKON, moving the edge of the absorption band to about 2 Hz ($\tau \sim 0.08$) would more than account for the high frequency energy. As an example, synthetics for RKON ($t^* = .75$) and for HNME ($t^* = 1.15$) for $\tau_m = 0.08$ are shown in Figures 10 and 11. A comparison between either of the band-passed records or the spectral plots, Figures 12 and 13, and the actual data show that the synthetics now have too much high frequency energy. For this single example it seems that the position of the absorption band is not constant: HNME is fairly well modeled with $\tau_m \sim .001$ for RKON $\tau_m < 0.08$.

Currently there are two distinct methodologies in the analysis of seismic attenuation: Amplitude data from both short and long period

Attenuation vs Tau m, $t^* = 1$.

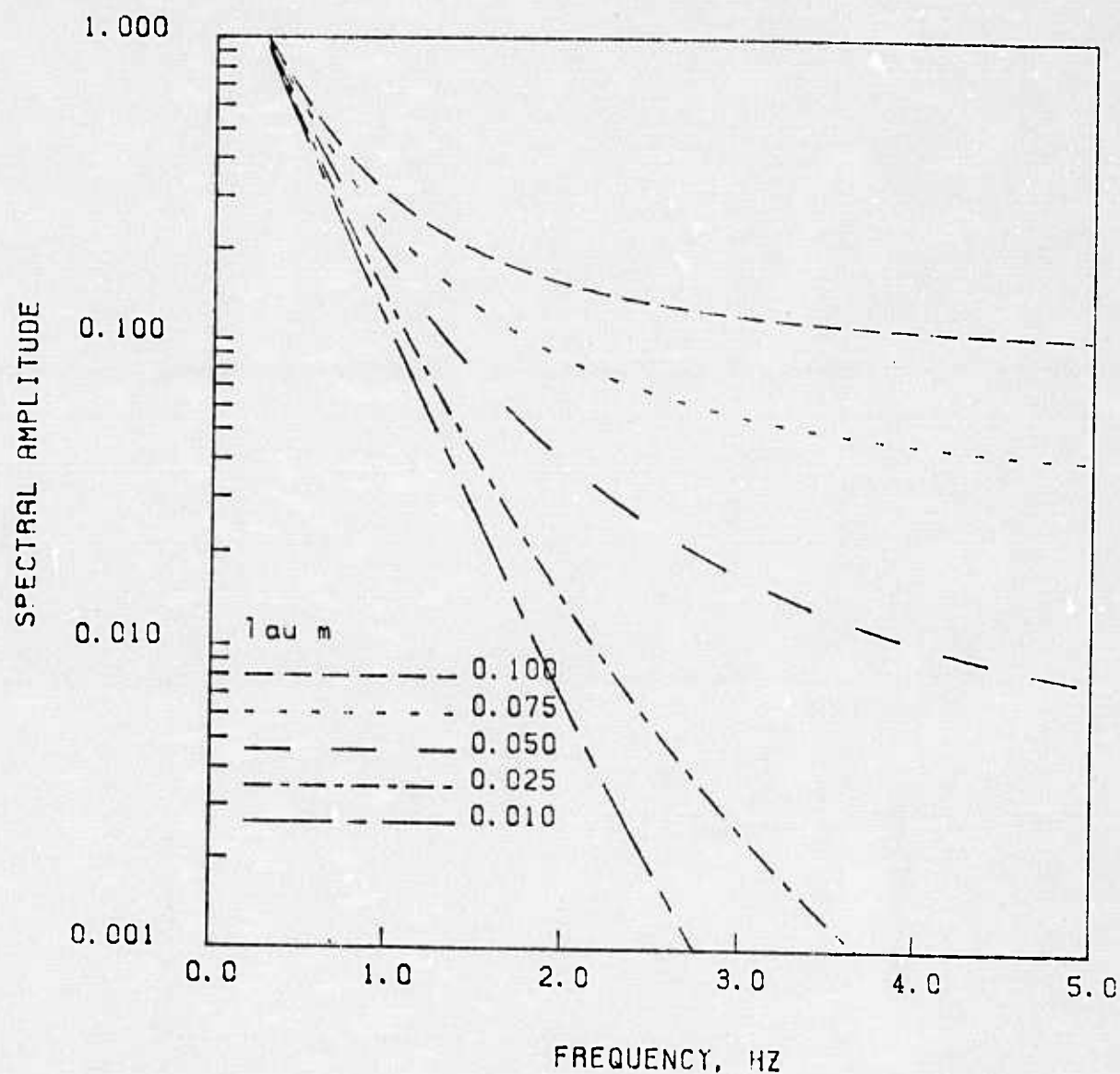


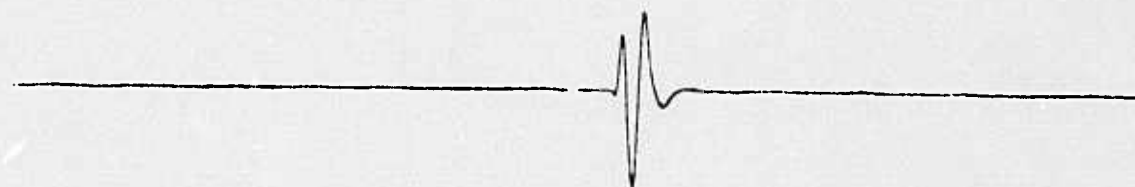
Figure 9:

Spectral amplitudes of attenuation operators described by an absorption band model. Five possible positions of the high frequency corner of the band are shown.

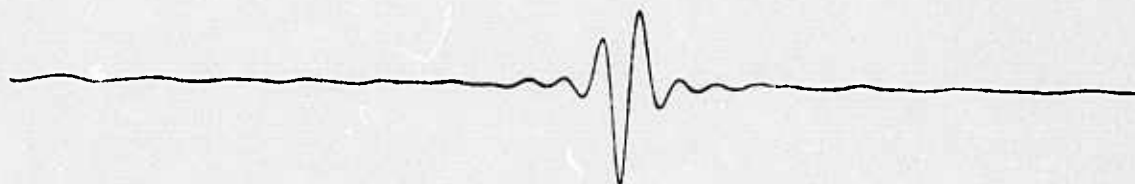
RKON SYNTHETIC

XMAX= 909.010

RATIO

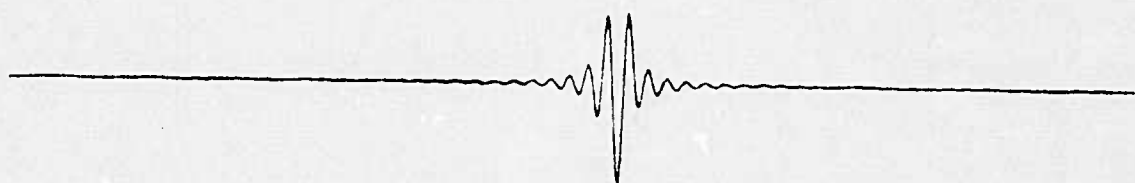


CENTER FREQUENCY: 1 HZ, XMAX= 351.182



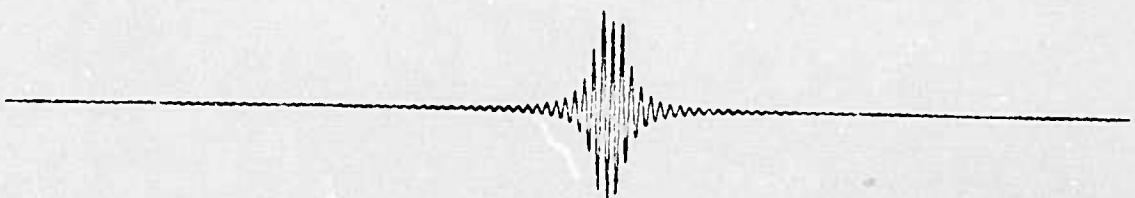
.36

CENTER FREQUENCY: 2 HZ, XMAX= 164.593



.17

CENTER FREQUENCY: 4 HZ, XMAX= 22.319



.02

Figure 10: Synthetic waveforms for the record at RKON. The attenuation operator used is described by $t^* = .75$ and $\tau_m = .08$. The source model is the same as described on Figure 5.

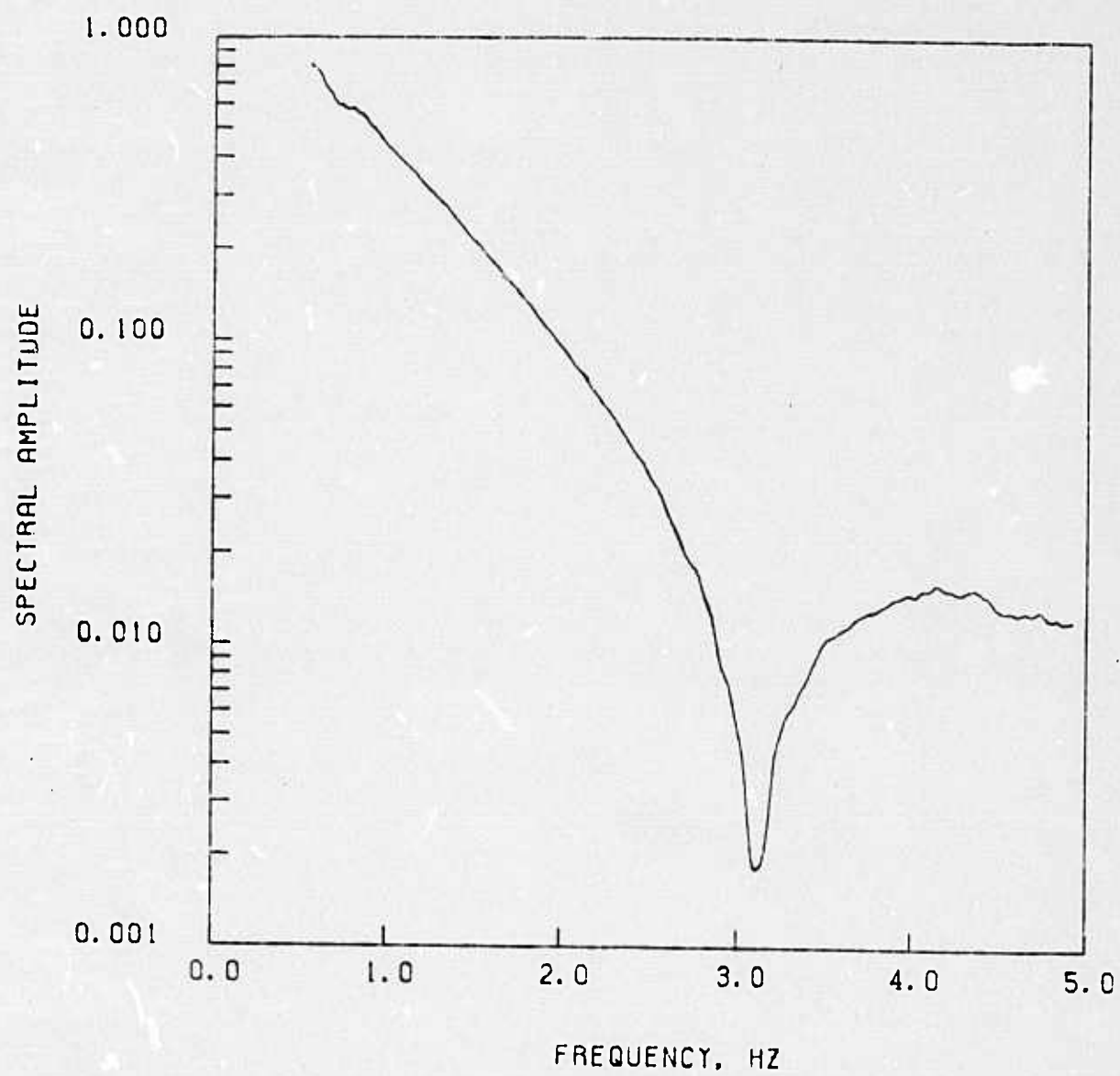
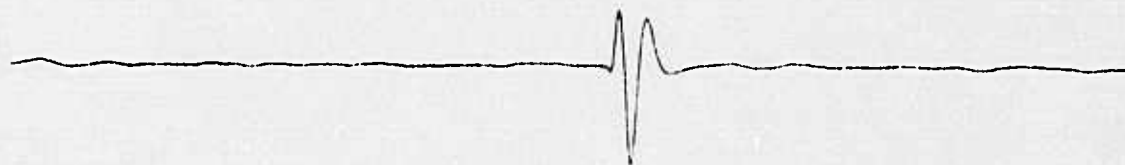


Figure 11: Fourier transform of the top trace shown on Figure 10.

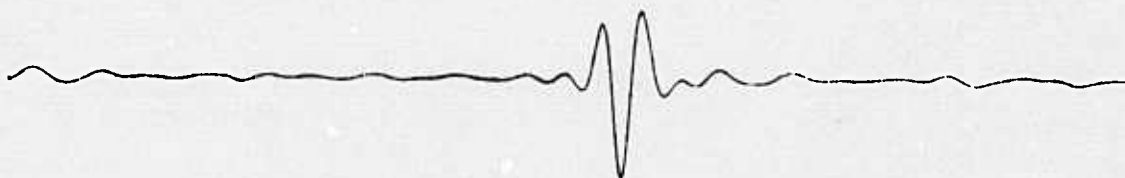
HNME-SYNTHETIC

XMAX= 316.080

RATIO

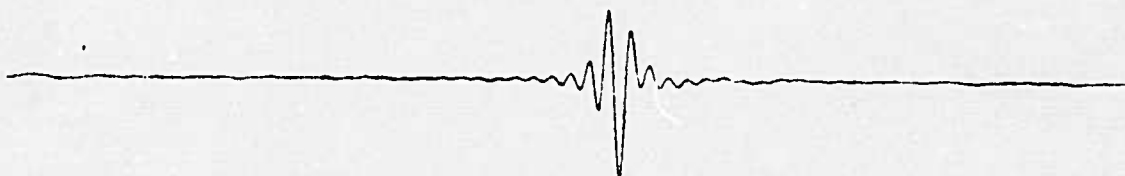


CENTER FREQUENCY: 1 HZ, XMAX= 154.527



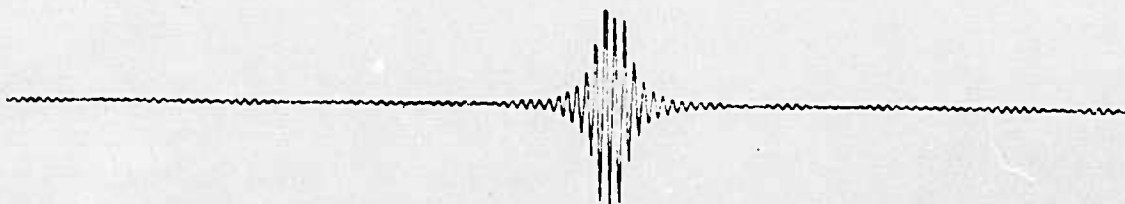
.48

CENTER FREQUENCY: 2 HZ, XMAX= 54.124



.17

CENTER FREQUENCY: 4 HZ, XMAX= 4.814



.015

Figure 12:

Synthetic waveforms for the record at HNME. The attenuation operator used is described by $t^*=1.15$ and $\tau_m=.08$. The reflection time for pP was changed to 0.35 sec. The source model is the same as described on Figure 5.

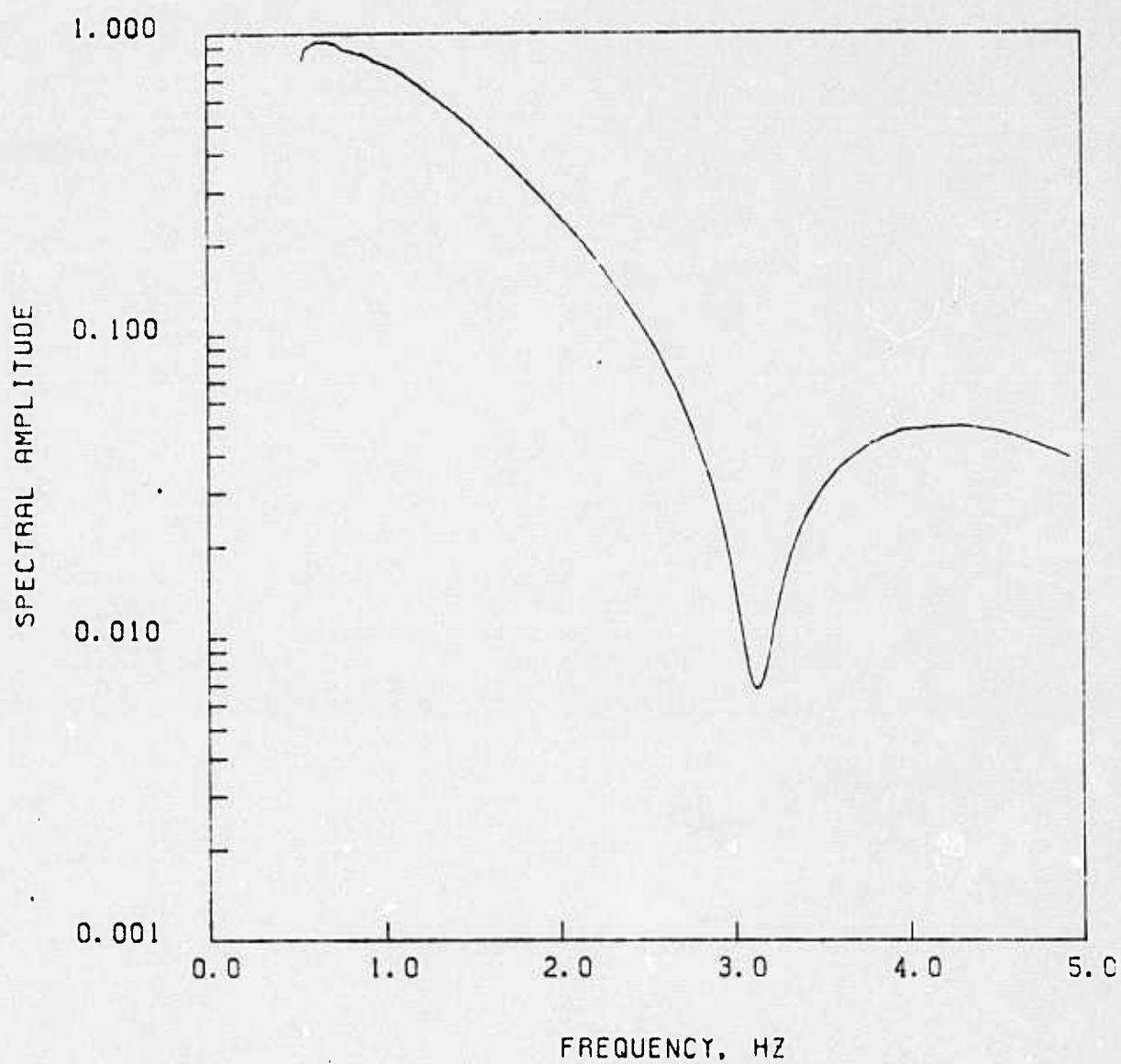


Figure 13: Fourier transform of the top trace shown on Figure 12.

seismographs (which are closely related to m_b) and spectral ratios. The amplitude data for each source region and each site have been shown by Butler (1979) to be quite stable. For the first-order estimate of m_b , this amplitude data is crucial. However, towards the goal of modeling a range of seismic bands (i.e., 1, 2, and 4 Hz) the spectral slope data should be incorporated into the absolute level estimates at ~ 1 Hz. The above paragraphs discuss a smooth model that can connect the 1 and 4 Hz observations. Since the absorption band model represents a temperature activated process, we expect some relationship between temperature, the position of the band, and t^* , i.e., high temperatures imply large attenuation and short diffusion times (small τ_m). As discussed above, this model is well founded in previous theoretical works.

The limited modeling study presented above should not be interpreted as demonstrating the existence of frequency-dependent attenuation. The principal objective of this study has been to examine for a few simple cases the proposition that a frequency dependent Q operator can unite the diverse views of t^* . Consideration of Figure 9 and the results from the modeling of a simple source strongly suggest that a frequency-dependent attenuation model can unify the current divergent views.

IV. ESTIMATION OF RECEIVER FUNCTIONS FOR STATIONS LOCATED AT THE NTS

4.1 THEORY

The method that has been used in estimating receiver functions is a two stage procedure. The first stage uses deconvolution and complex log spectral stacking to produce transfer functions that map seismograms recorded at a reference station into those recorded at other stations. The second stage uses a Minimum Entropy Deconvolution method (Wiggins, 1978) to estimate receiver functions for all stations, including the reference station, from the transfer functions obtained in stage one.

In order to obtain a transfer function relating near receiver responses of a reference station to another station we must remove the effects of the source and near source structure. This may be done by deconvolution if the apparent source, including near source structure effects, is the same for both stations. To ensure this condition is met, we must either use stations that are close together, and thus have similar source receiver azimuths and ray parameters, or use non-directional sources. Further, due to the presence of near receiver lateral inhomogeneities, we should limit events in any stack to a relatively narrow azimuth range.

Assuming that the above conditions are met, deconvolution of the reference seismogram from the seismograms recorded at other stations will effectively remove source, instrument and some attenuation effects. Let $\bar{s}_0^i(\omega)$ and $\bar{s}_j^i(\omega)$ be, respectively, the Fourier transforms of the seismogram of the i th event at the reference and j th station. The deconvolution for the i th event and j th station is just $\bar{d}_j^i(\omega) = \bar{s}_j^i(\omega) / \bar{s}_0^i(\omega)$

We may now produce an average transfer function $\bar{t}^j(\omega)$ for the j th station relative to the reference station by a complex log spectral stack.

$$\log \bar{t}_j(\omega) = \frac{1}{n} \sum_{i=1}^n \log \bar{d}_j^i(\omega) \quad (2)$$

It should be noted that the same formal estimate for $t_j(\omega)$ may be obtained by stacking the log spectra of the seismograms first and then deconvolving the stacked seismograms. However, by performing the deconvolution first it is possible to avoid the phase unwinding problems that usually plague complex log spectral methods. While there is no problem determining $\log |\bar{t}_j(\omega)| = \frac{1}{n} \sum_i \log |\bar{d}_j^i(\omega)|$, determining the phase is somewhat problematic, due to $2\pi i$ ambiguities in the complex log function. However, by deconvolving first and detrending the $\bar{d}_j^i(\omega)$ over a specified frequency band, which corresponds merely to an absolute time shift of $s_j^i(t)$ with respect to $s_0^i(t)$ it is possible to concentrate the $\bar{d}_j^i(\omega)$ in one half of the complex plane or less for a given ω . Phases may then be averaged and problems of $\frac{2\pi m}{n}$ phase shifts are avoided, since the same $2\pi m$ absolute phase shifts are ignored for all n deconvolved signals.

An alternative approach to producing the functions $\bar{t}_j(\omega)$ is the standard deconvolution procedure. This involves determining $\bar{t}^i(\omega)$ that minimizes the functionals $e_j = \sum_i ||\bar{s}_j^i(\omega) - \bar{t}_j(\omega) \bar{s}_0^i||^2$. There are several advantages to using the log spectral stack, as opposed to standard deconvolution methods. The first is the relative insensitivity of the log spectral method to absolute timing information. This permits higher frequency information to be retained than is possible with conventional methods. Also, while

standard methods are effective in dealing with random additive noise, the principal noise in many seismograms is not stationary additive noise but rather signal controlled noise. Such noise may be modeled by convolution in the time domain. Since time domain convolutions become additions in the log spectral domain, we see that log spectral stacking tends to effectively cancel such noise processes. Causes of such noise include amplitude and moveout changes of later arrivals due to local near receiver inhomogeneities, azimuthal changes from event to event, and changes in the apparent source from station to station for a single event.

The transfer functions $\bar{t}_j(\omega)$ obtained from the deconvolution and stacking procedure contain not only the desired receiver functions, $\bar{r}_j(\omega)$, but also the inverse of the reference station receiver function, $\bar{r}_0(\omega)$ thus, we may write

$$\bar{t}_j(\omega) = \bar{r}_j(\omega) / \bar{r}_0(\omega) \quad j \geq 1 \quad (3)$$

$$\bar{t}_0(\omega) = 1$$

In order to recover $\bar{r}_0(\omega)$, and hence $\bar{r}_j(\omega)$ we must impose an additional constraint on the problem. The constraint we shall use is that the $r_j(t)$ be, on the average, as simple or "delta-like" as possible. This may be done by minimizing a weighted varimax norm

$$V = \sum_{i=0}^n w_i v_i = \sum_i w_i \frac{\int r_i^4(t) dt}{\left(\int r_i^2(t) dt \right)^2} \quad (4)$$

This procedure, known as Minimum Entropy Deconvolution (MED) and the properties of the varimax norm have been discussed by Wiggins (1978). In addition to producing the "simplest" possible estimates of $r_0 \dots r_n$, the MED procedure has the property of rejecting incoherent high frequency energy. Thus, while the ratios of $\bar{r}_j(\omega)/\bar{r}_0(\omega)$ are fixed by the \bar{r}_j 's, the absolute amount of energy in any frequency band for $r_0 \dots r_n$ is determined by the coherence of the \bar{r}_j 's in that band. In this way, the MED process aids in stabilizing the results of the deconvolution and stacking procedure.

It may be shown that minimization of the functional in equation 4 is equivalent to solving the system of non-linear simultaneous equations

$$r_0 * \sum_i \frac{v_i w_i}{u_i} (t_i * t_i) = \sum_i \frac{w_i}{u_i} (r_i^3 * t_i) \quad (5)$$

where $u_i = \int r_i^2(t) dt$, $*$ denotes convolution and \star denotes correlation.

These equations may be solved for r_0 iteratively, either in the frequency or time domain. Wiggins had adopted a modified Levinson recursion algorithm in order to obtain a time domain solution. However, since we expect that the time duration of $r_0(t)$ may well be comparable to the duration of the $r_i(t)$, we have adopted a frequency domain solution. Through the use of FFT algorithms, it is possible to save considerable computer time in this manner.

In the frequency domain, we may express equation 5 as

$$\bar{r}_0^*(\omega) = \frac{\sum_i \frac{w_i}{u_i} \bar{r}_i^*(\omega) \bar{t}_i(\omega)}{\sum_i \frac{v_i w_i}{v_i} \bar{r}_i^*(\omega) \bar{r}_i(\omega)}$$

where $R_i(t) = r_i^3(t)$ and f^* denotes the complex conjugate of f . This equation may be solved iteratively by first assuming $r_0(t) = \delta(t-t_0)$, and hence $R_i(t) = t_i^3(t-t_0)$. We may then solve for $r_0(\omega)$ and in this way generate a new estimate of $R_i(t)$. In general, this procedure must be repeated only 4 or 5 times before convergence is obtained. By replacing $R_i(t)$ with $R_i(t) H(t)$, $H(t)$ is a heavy side function, at each iterative step, we may introduce some semblance of causality into our solution, without, in general, adversely affecting the convergence rate.

It should be noted that, while the minimum obtained in iteratively solving (7) is not unique, a useful minimum may easily be obtained by adjusting the weighting functions w_i . In general, however, experience has shown that the solution obtained is not critically dependent on the choice of w_i 's. It should also be noted that, except for possible problems with multiple minima, the entire stacking and MED process is invariant to the choice of which station is to be used as the reference station. That is, with proper choice of w_i , the same set of r_i functions is obtained, independent of the choice of the reference station.

It should also be noted that there is no guarantee that the simplicity criterion of MED in fact produces the true receiver functions for the set of stations. In particular, if some feature is common to all receivers, it will probably be removed from all receiver estimates. This, however, is not considered a likely occurrence. One possible check is provided by comparing the varimax norms for synthetic seismograms at all stations produced using a reasonable source function, attenuation operator, etc., with the norms computed for a simple event, well recorded at all stations. If the degrees of complexity, as indicated by the varimax norms, agree for data and synthetic, then this is an indication that no large scale common

structure has been eliminated. Additional tests are possible for sources where independent near field estimates of the source are available.

4.2 APPLICATION TO DATA

The methods of the previous section have been applied to events recorded by the SDCS stations located at Yucca Flats, denoted by YF1 through YF4, and a station OB2 located at Climax Stock. In general, seismograms recorded at the YF stations, which are located in a dipping basin, show far greater complexity than do the same events recorded at OB2. Events from 3 azimuthal windows (northwest, southwest and southeast) have been examined in detail.

In order to test the deconvolution and stacking procedure, transfer functions obtained from the procedure were used to predict the seismograms at the YF stations from those recorded at OB2. This also provides a check on the assumption that near station structure varies sufficiently slowly that variations in azimuth and ray parameter from event to event within each azimuth window do not produce large amounts of scatter in the receiver function estimates.

As may be seen from Figures 14, 15, and 16 there is very good agreement between observed and predicted waveforms for the YF stations. While many of the differences that do exist may be attributed to the presence of high frequency noise at the YF stations, there are variations associated with small changes in azimuth or ray parameter that must result from three dimensional near receiver structure. These appear primarily as large, incoherent arrivals late in the record. Since a large degree of interference is present late in the record, particularly for complex sources, it is not surprising that deviations from an "average" transfer function become apparent in this portion of the record.

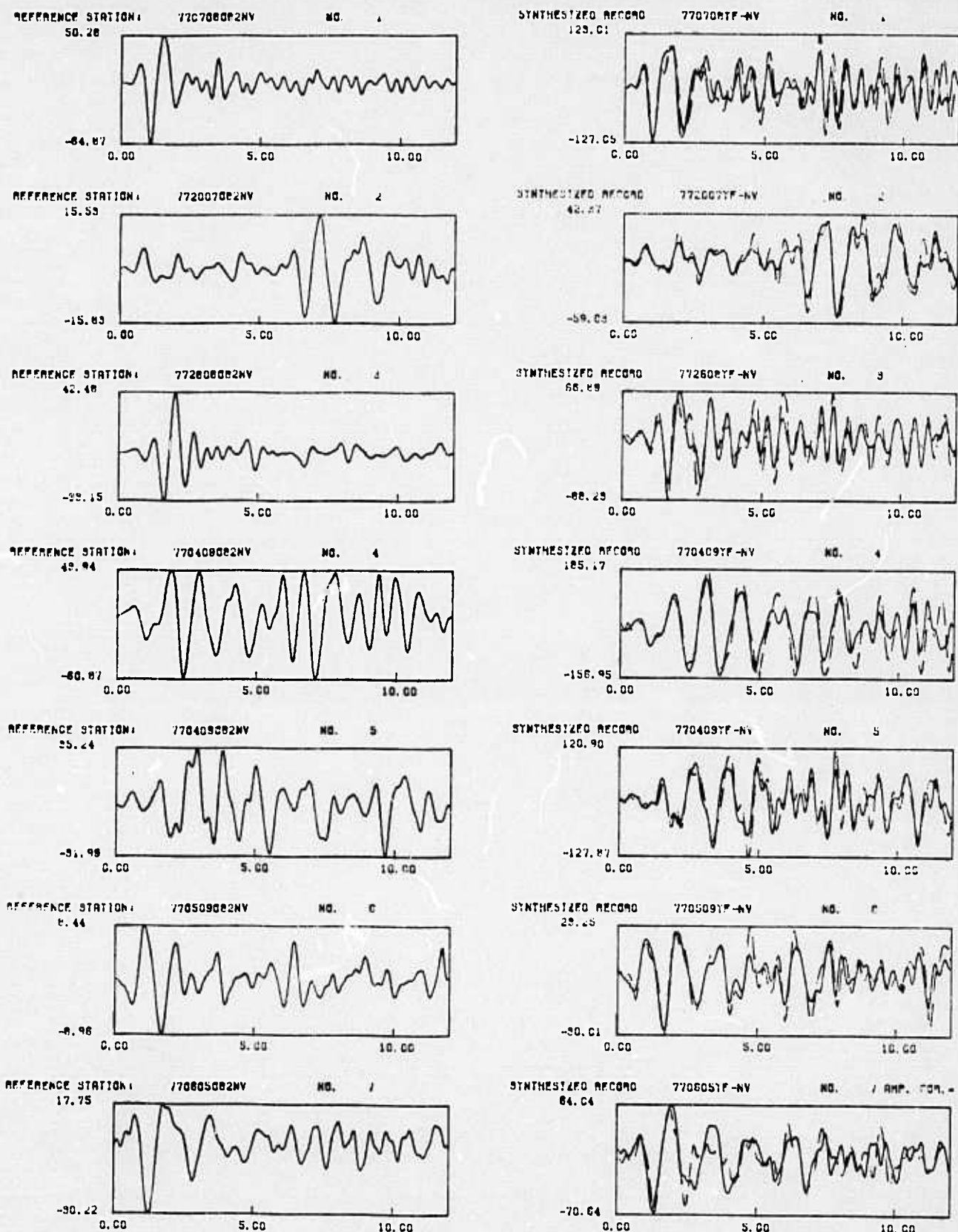
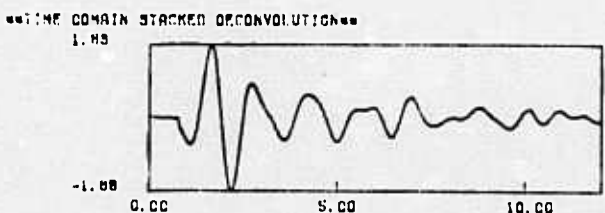
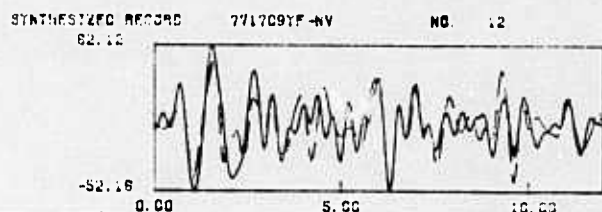
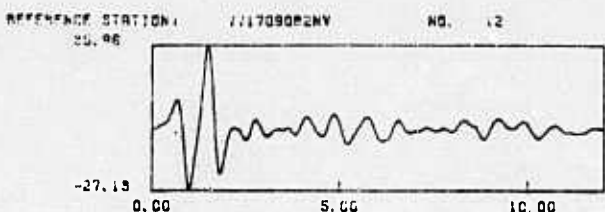
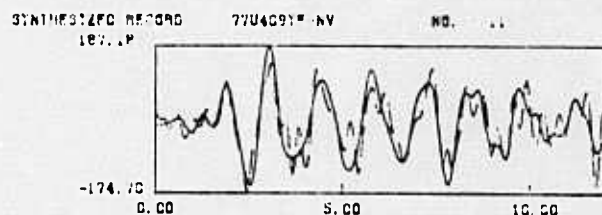
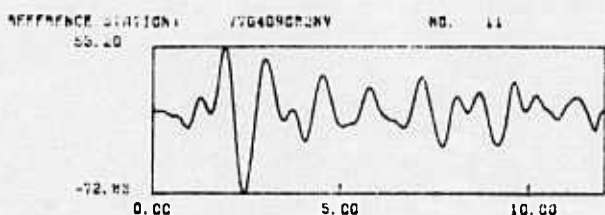
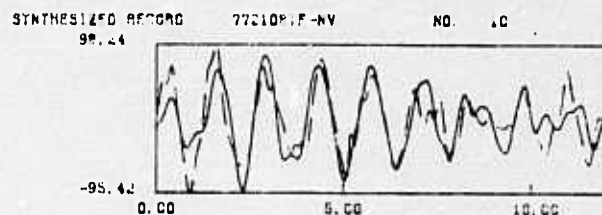
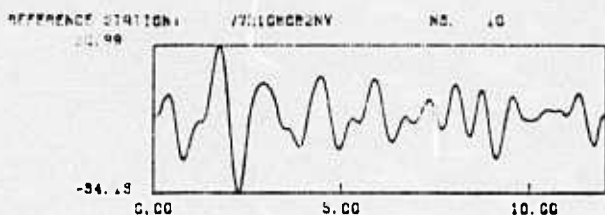
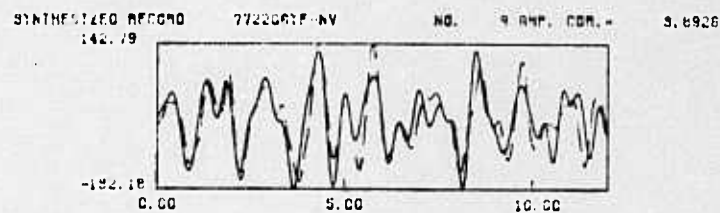
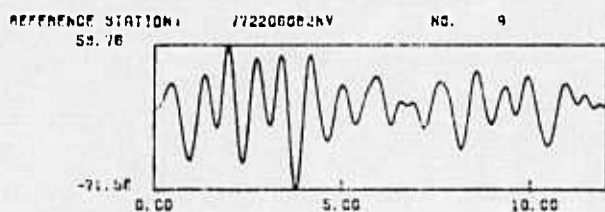
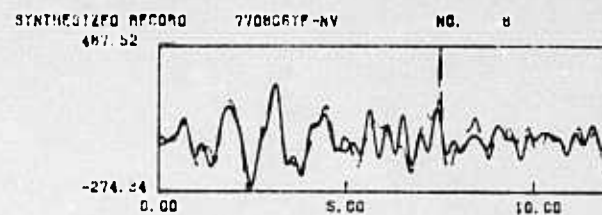
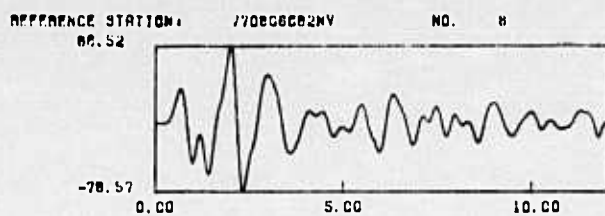


Figure 14. Observed seismograms at stations OB2NV (left) and YF2NV (right, dashed) from events to the northwest. Synthetic seismograms (right, solid) for station YF2NV produced by convolving the OB2NV observation with the YF2 receiver functions appropriate to a northwest azimuth.



THIS PAGE IS BEST QUALITY PRACTICABLE
FROM COPY FURNISHED TO DDC

Figure 14. (Continued)

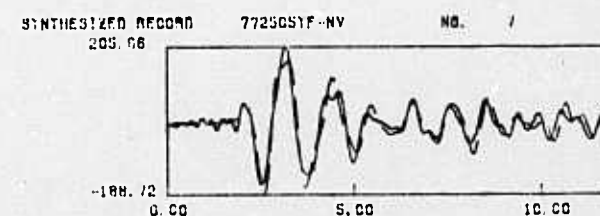
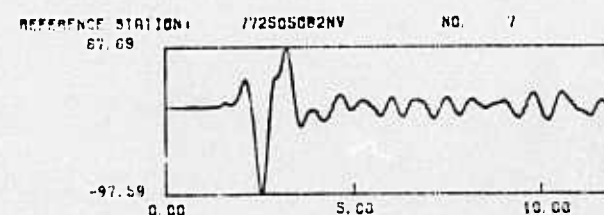
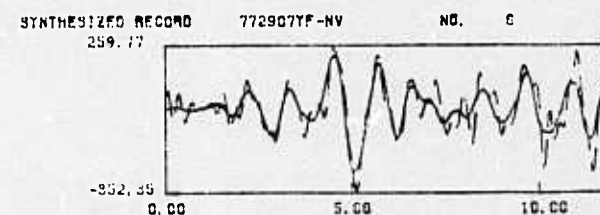
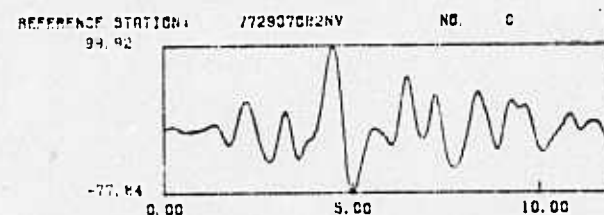
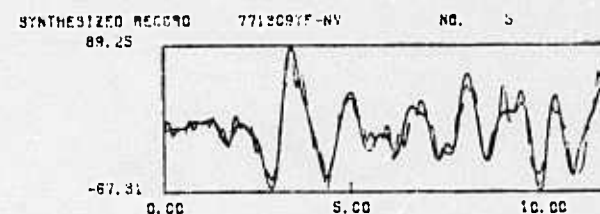
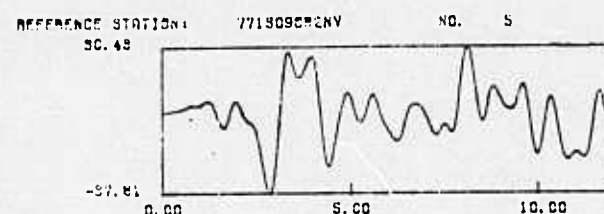
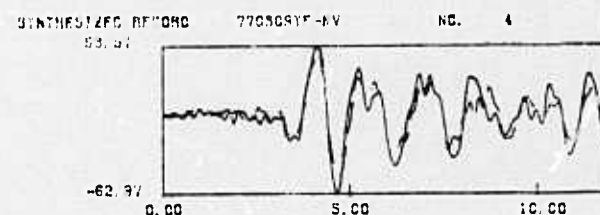
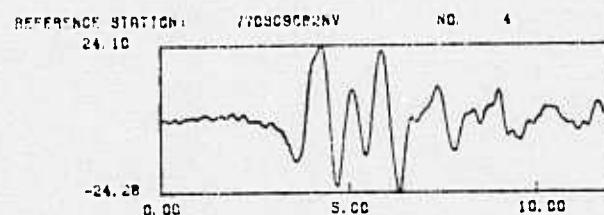
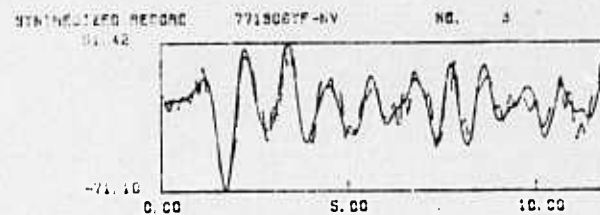
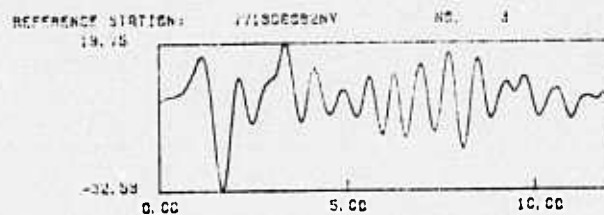
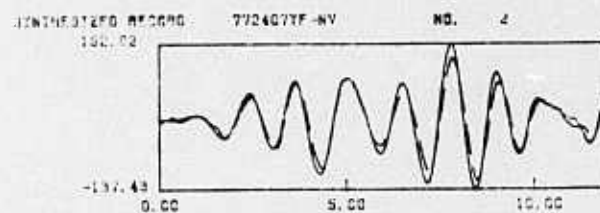
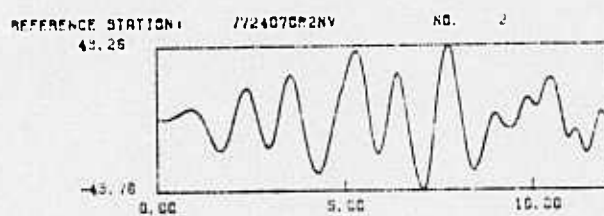
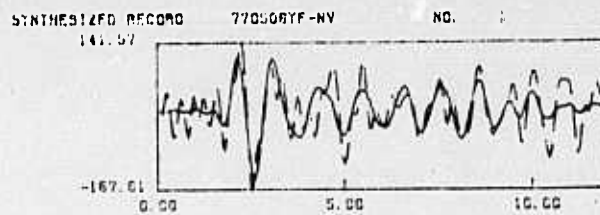
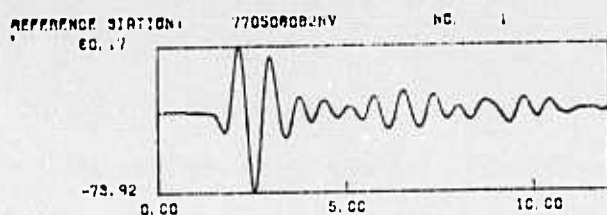
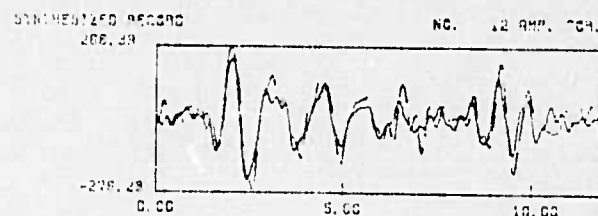
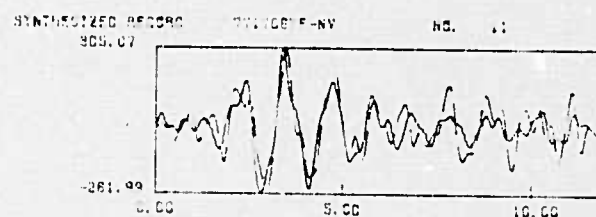
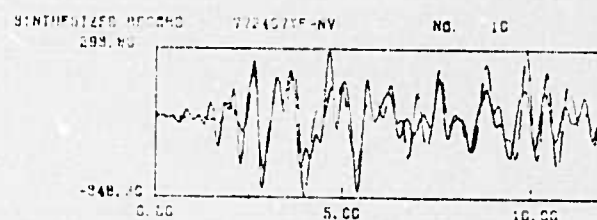
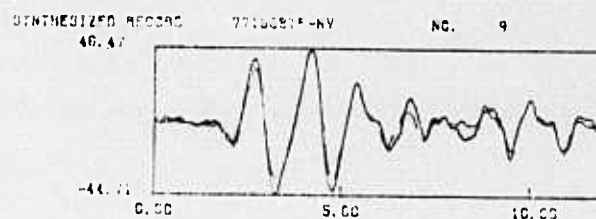
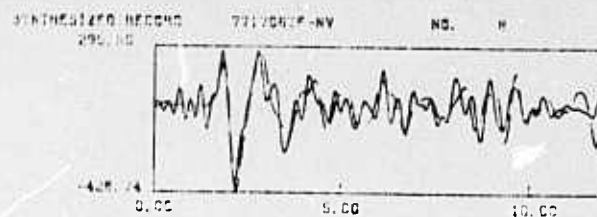
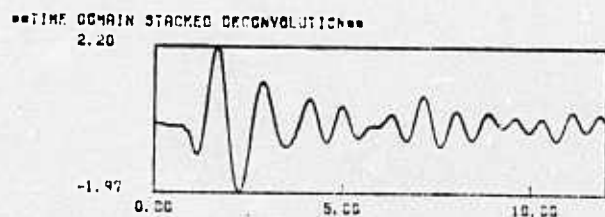
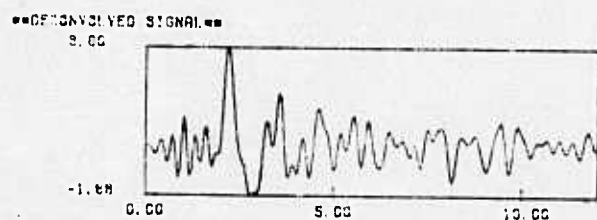
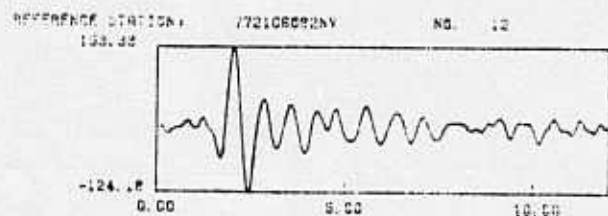
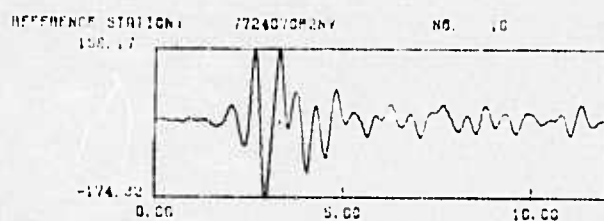
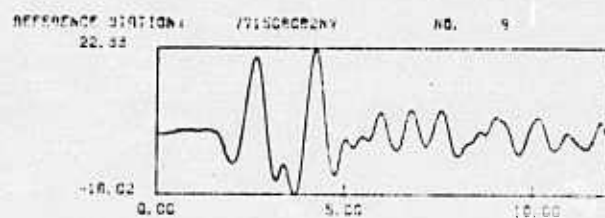
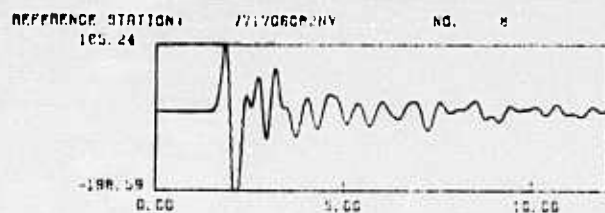


Figure 15. Same as Figure 14 except the events are from the southwest and the receiver function is adjusted accordingly.



4.8443

THIS PAGE IS BEST QUALITY PRACTICABLE
FROM COPY FURNISHED TO DDC

Figure 15. (Continued)

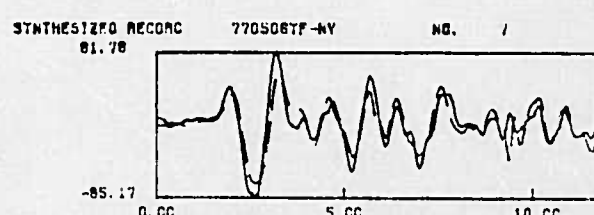
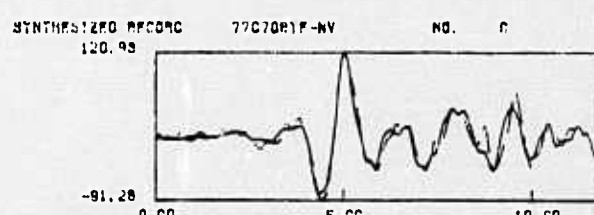
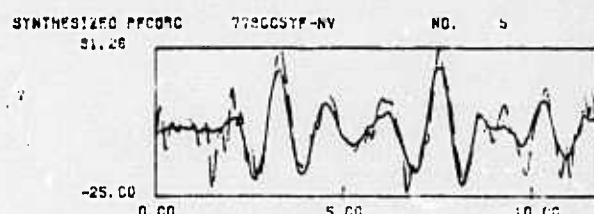
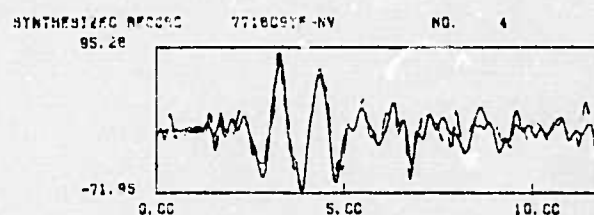
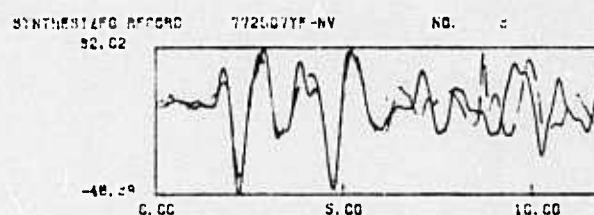
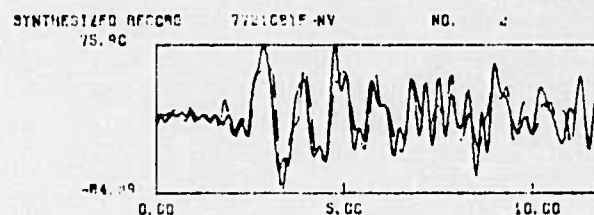
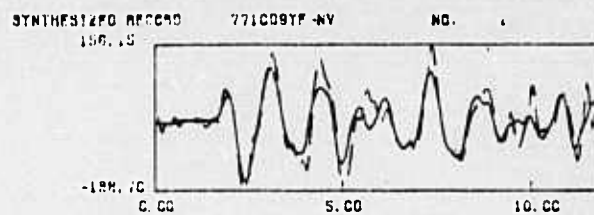
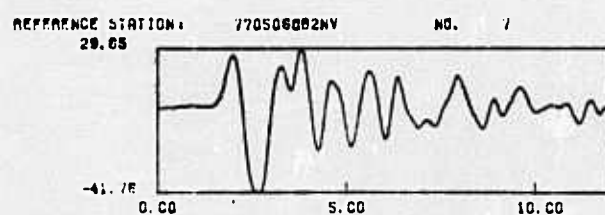
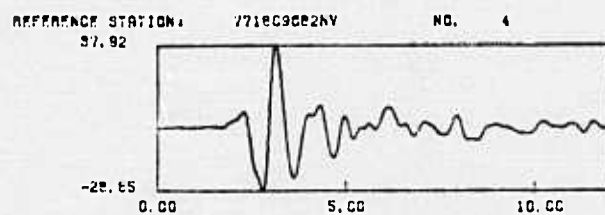
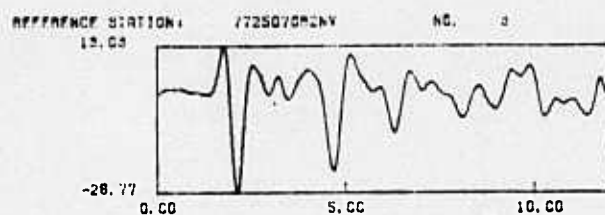
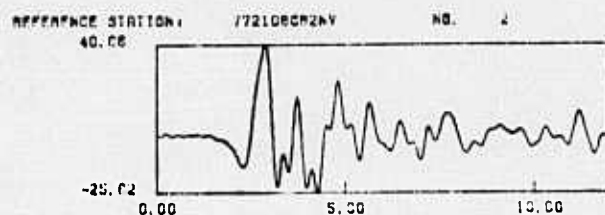
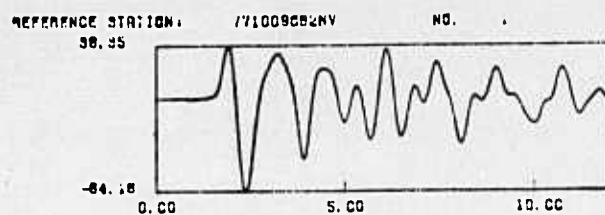
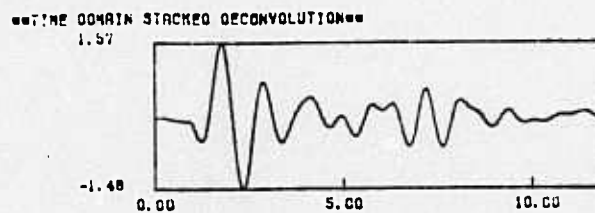
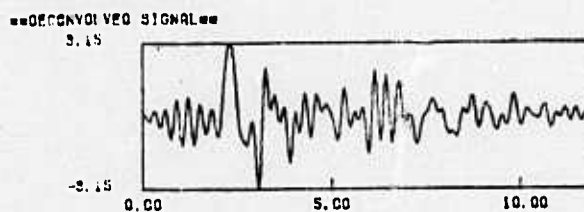
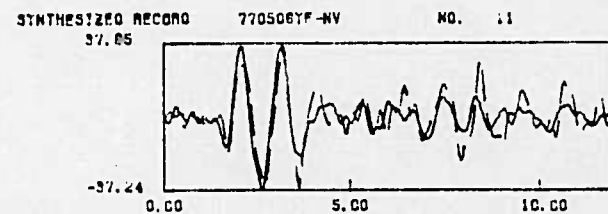
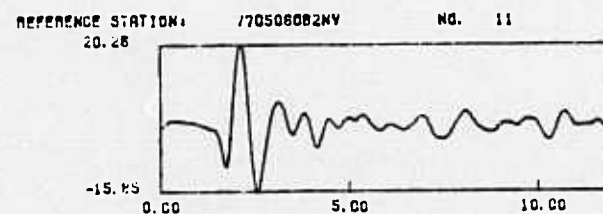
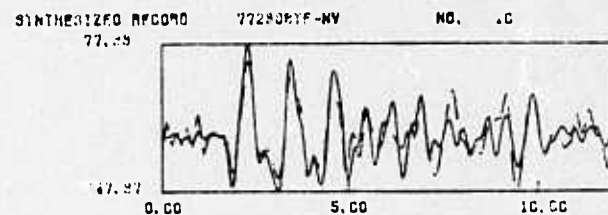
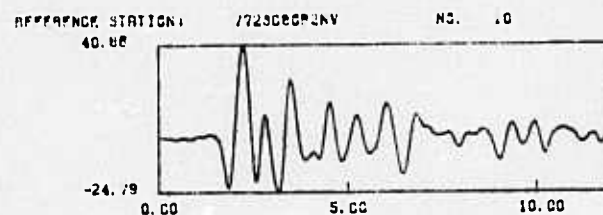
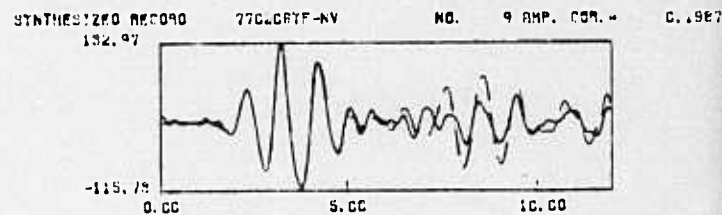
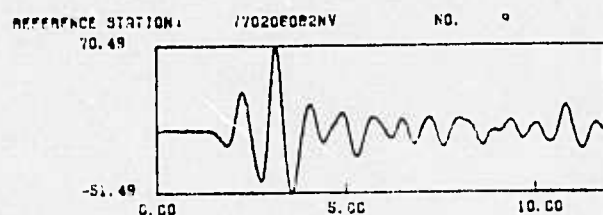
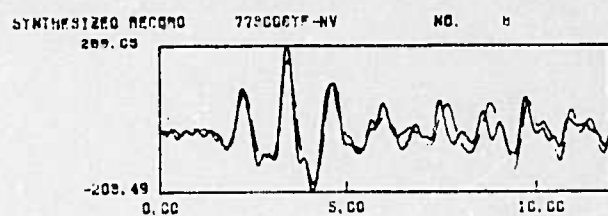
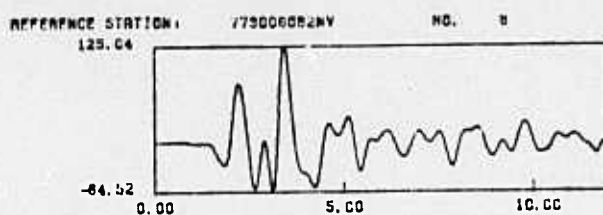


Figure 16. Same as Figure 14 but for events from the southeast and receiver function is adjusted accordingly.

THIS PAGE IS BEST QUALITY PRACTICABLE
FROM COPY FURNISHED TO DDC



THIS PAGE IS BEST QUALITY PRACTICABLE
FROM COPY FURNISHED TO DDC

Figure 16. (Continued)

The transfer functions obtained from the deconvolution and stacking procedure were then processed using the MED technique in order to obtain estimates of actual receiver functions. Receiver functions obtained in this manner are shown in Figures 17, 18, and 19. The small, precursory arrivals present in the YF receiver functions are largely the result of noise in the YF records. The finite width of the pulses in the receiver function is due to the band limited nature of the data and the presence of high frequency noise at the YF stations.

As expected, receiver functions for the station OB2 are considerably simpler than those for the YF stations. In general, receiver functions for the YF stations are characterized by three or possibly four moderately sized negative arrivals following the first large positive arrival. These, in turn, are consistently followed by a large positive arrival. The early negative arrivals appear to show some moveout and amplitude variation as we move from YF1 to YF4. These arrivals also exhibit significant amplitude variation as a function of azimuth. This azimuthal variation is sufficiently large that transfer functions derived for one azimuth do not, in general, act as particularly good predictors for other azimuths. Interpretation of these early arrivals, in light of the known average structure, will be done in the next section.

Due to the finite width of arrivals, it is not possible to predict the amplitude variations of incoming arrivals directly from the receiver function maximum amplitudes. We may, however, use the receiver functions and a synthetic incoming waveform to predict amplitude variations. Figure 20 shows the waveforms obtained using a synthetic underground explosion source convolved with a short period instrument and attenuation operator with $t^*=1$. As expected, the YF waveforms show considerably more complication than the

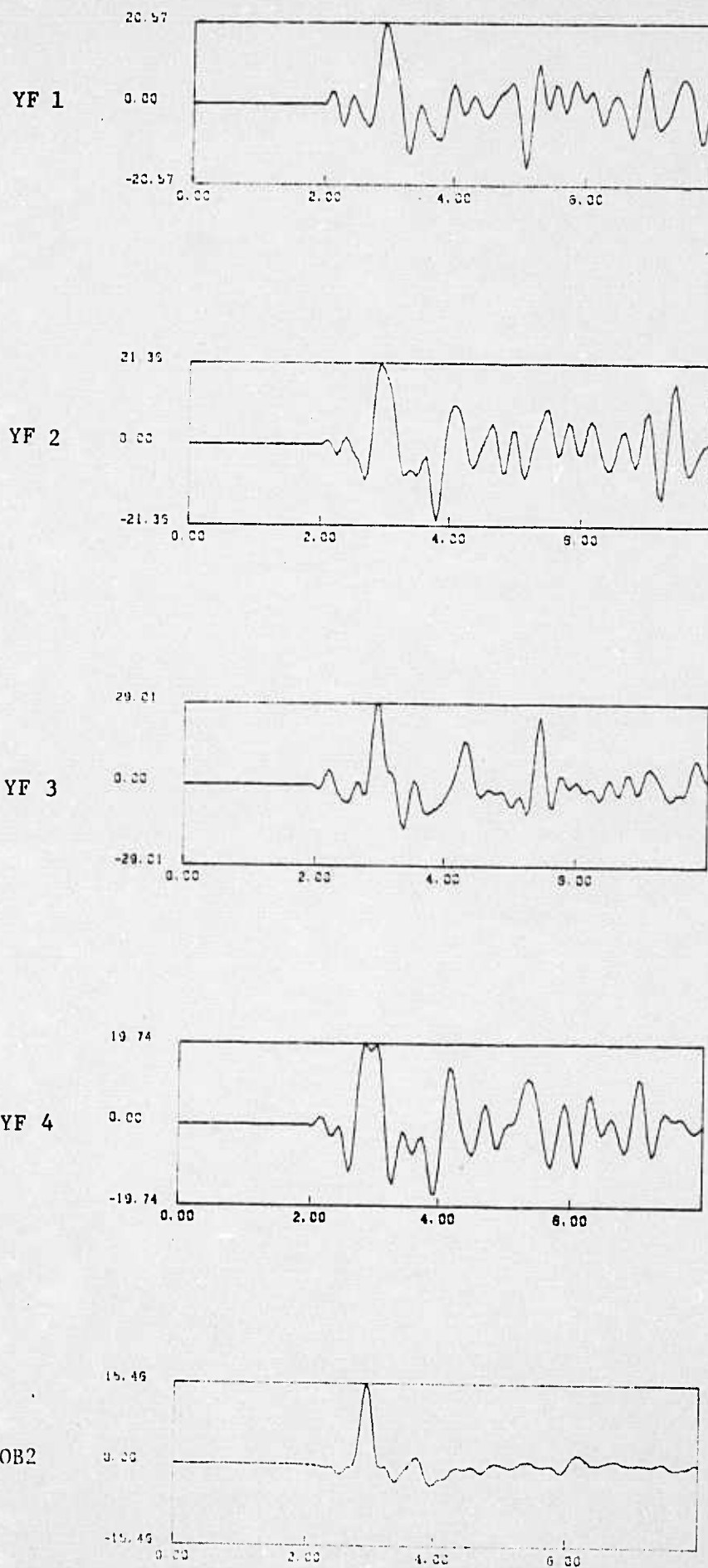


Figure 17. Receiver functions for the 4 YF array stations and the station OB2 appropriate to a northwest azimuth.

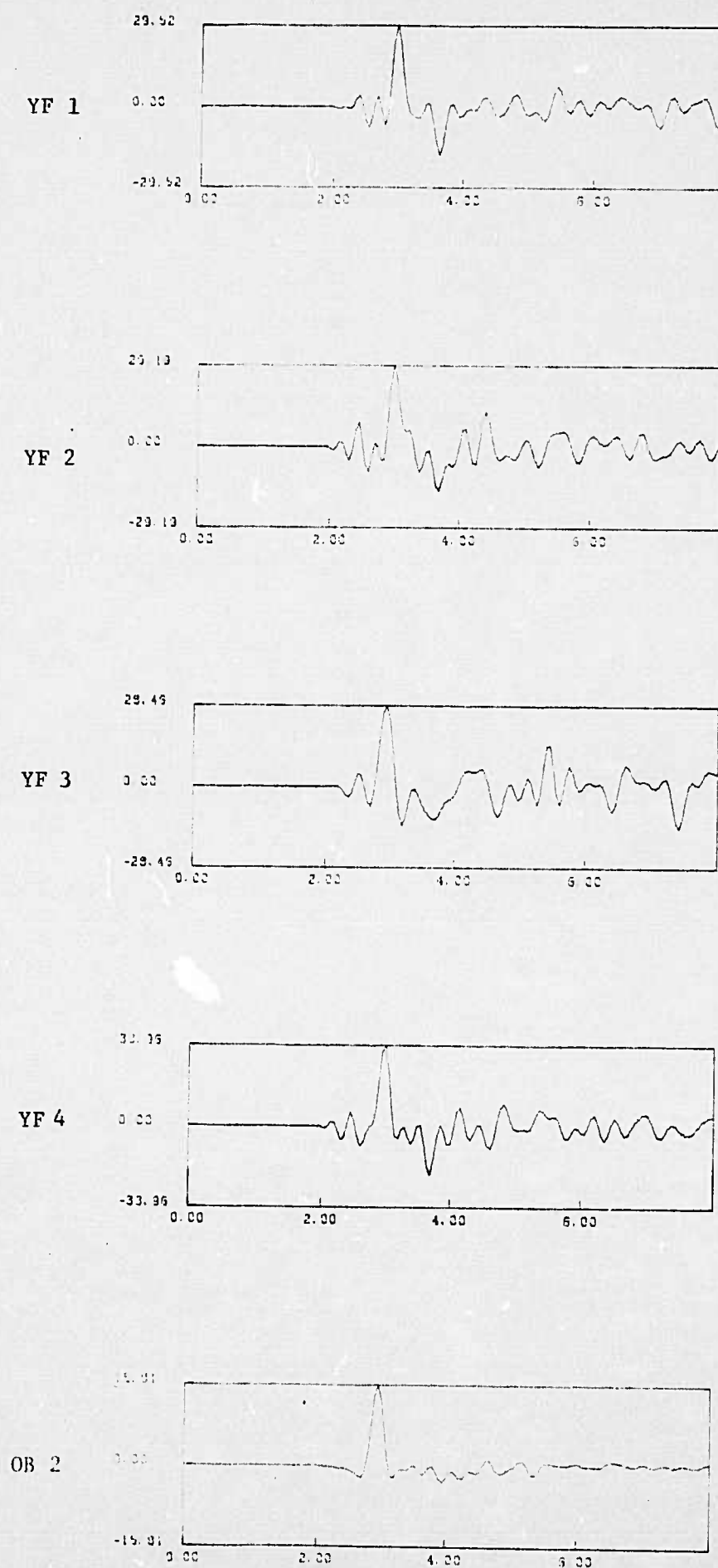


Figure 18. Receiver functions for the 4 YF array stations and the station OB2 appropriate to a southwest azimuth.

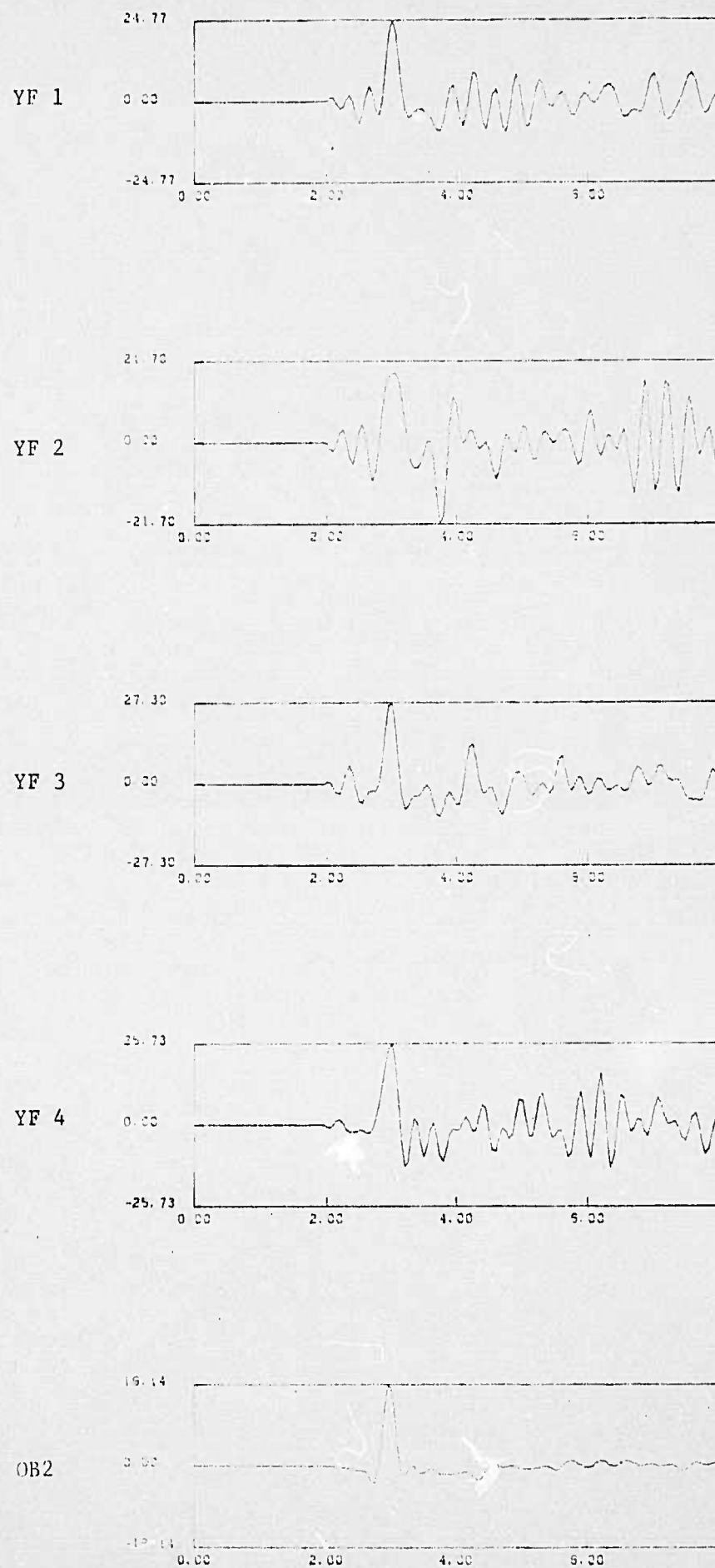


Figure 19. Receiver functions for the 4 YF array stations and the station OB2 appropriate to a southeast azimuth.

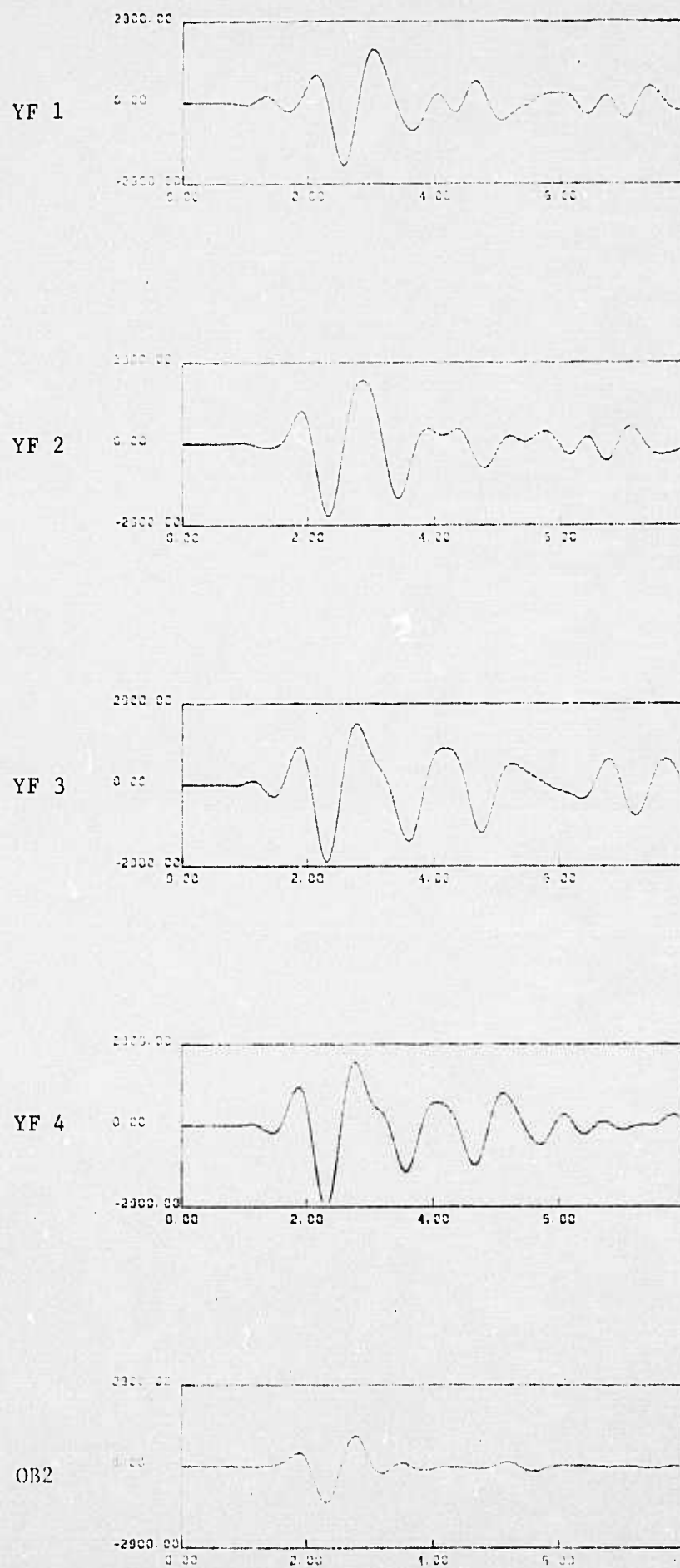
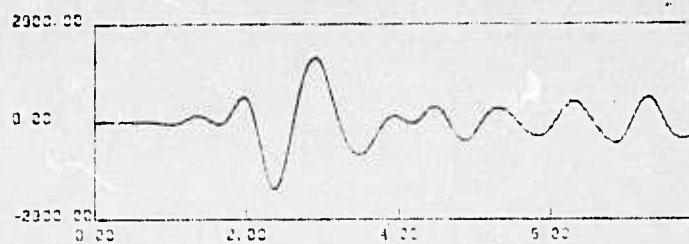
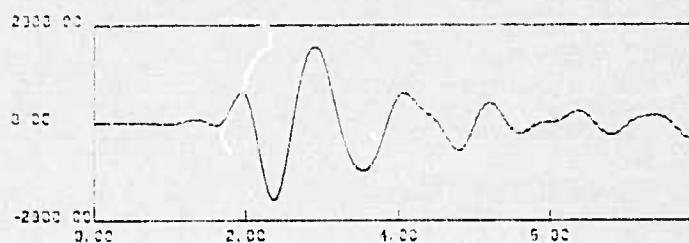


Figure 20a. Synthetic incoming P-waves computed by convolving receiver functions shown in Figure 17 (northwest azimuth)

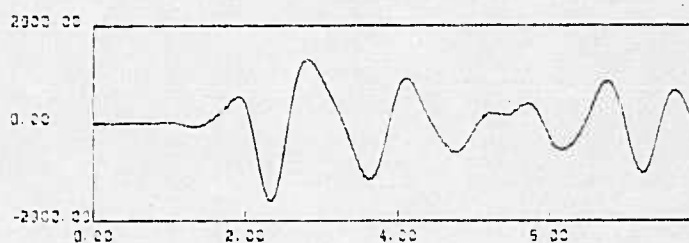
YF 1



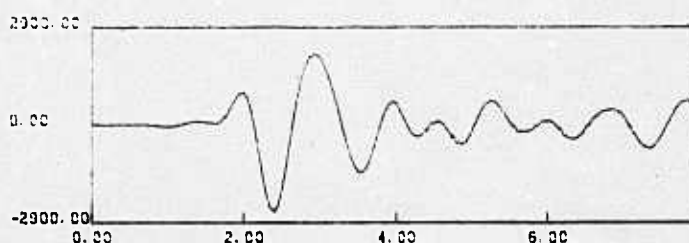
YF 2



YF 3



YF 4



OB2

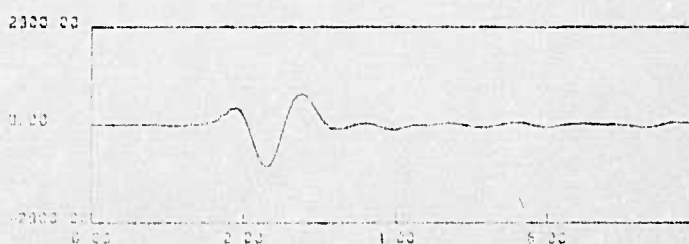


Figure 20b. Synthetic incoming P-waves computed by convolving the receiver functions shown in Figure 18 (southwest azimuth) with an explosion source.

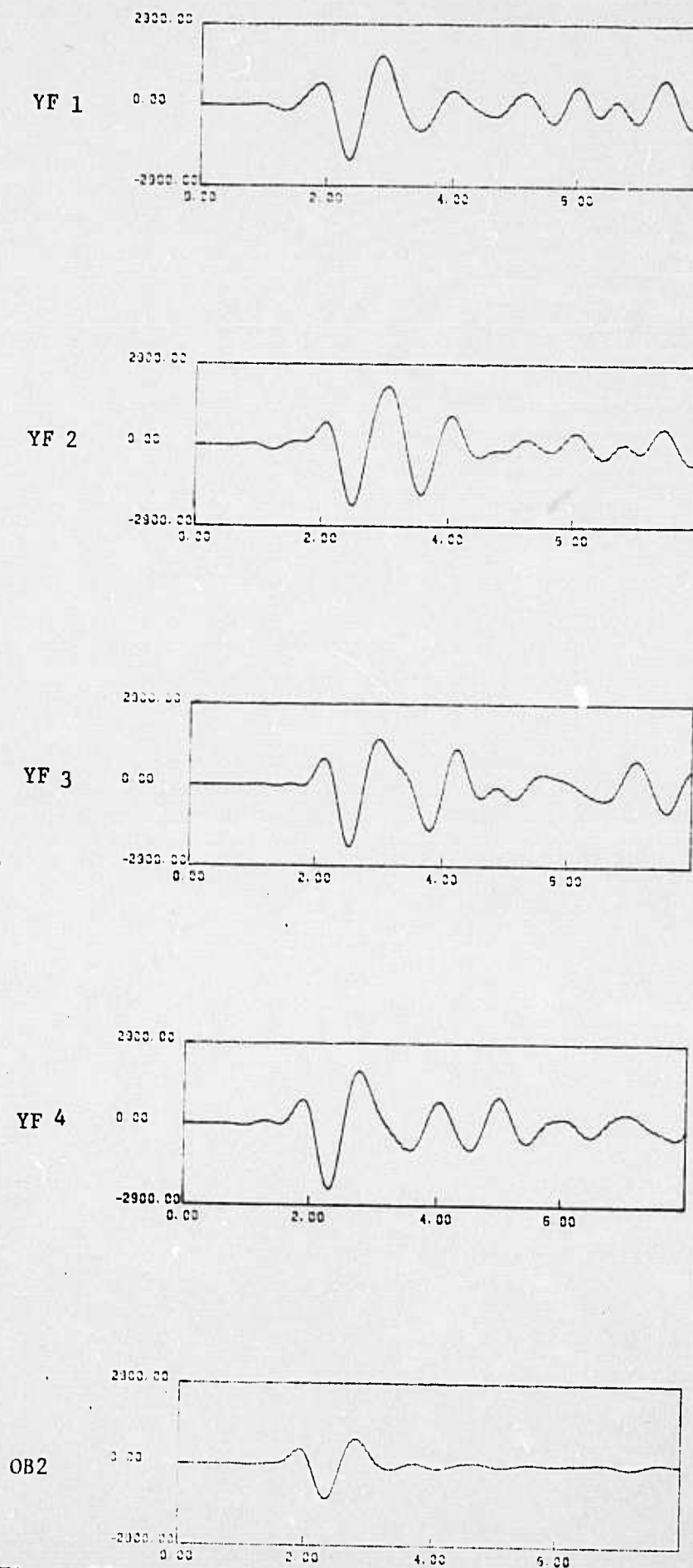


Figure 20c. Synthetic incoming P-waves computed by convolving the receiver functions shown in Figure 19 (southeast azimuth) with an explosion source.

OB2 waveforms. The YF receiver functions result in a factor of two amplification of the synthetic waveforms relative to OB2. This amplification is fairly well explained by the contrast in the shallow velocity structure between OB2 and the YF array. Figure 21 shows a range of waveforms and amplitudes that result from various near-surface velocity structures.

In order to compare the various synthetic amplitudes, we have normalized by the amplitude of the OB2 waveform at each azimuth. The log of the maximum amplitude for each station and azimuth, referenced to the maximum amplitude of the YF1 station for the northwest azimuth, is shown in Table 1. This table shows a 0.15 magnitude variation that is a function of both azimuth and station location.

It should be noted that azimuthal amplitude variation can be caused either by azimuthal variation at the YF stations or at OB2. With the present data set, there is no way of discriminating between these two possibilities. However, within each azimuth the data show a consistent, steady increase in amplitude from YF1 to YF4 corresponding to about .1 magnitude units. On the basis of reciprocity, this correlates with the east-west trend in magnitude bias observed by Alewine (1977), as shown in Figure 22, for nuclear events in the Yucca Flats region. The bias found in this study is less than that discussed by Alewine. However, the YF array extends across only the eastern portion of Yucca Flats. The bias reported here is based strictly on reciprocity and is clearly not related to any questions of lateral variation in near source material properties or source coupling. As discussed in the following section, the receiver functions are the result of complex wave propagation in the basin. The 0.1 magnitude bias across the YF array is most probably the result of elastic wave interference controlled by the shallow structure of the basin.

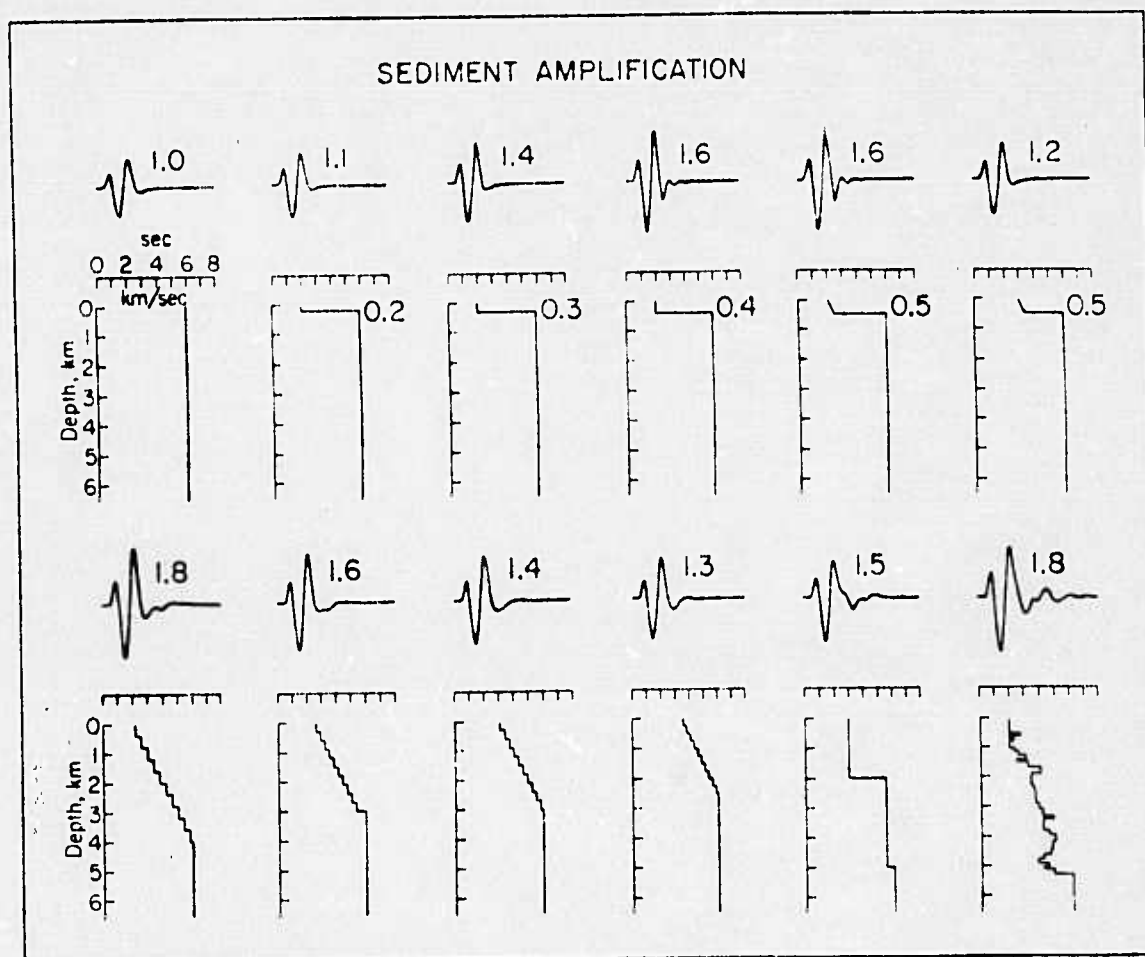


Figure 21. Amplification effects of shallow low velocity sediments upon crustal models. Amplitudes noted are relative to the bedrock model in upper left. Sediment thickness in kilometers is indicated in upper models.

Table 1

Magnitude Anomaly Associated with Receiver Functions
For Yucca Flats

	<u>NW</u>	<u>SW</u>	<u>SE</u>
YF1	0.0	-0.04	-0.05
YF2	0.05	0.02	0.00
YF3	0.08	0.03	0.01
YF4	0.10	0.07	0.03

JU

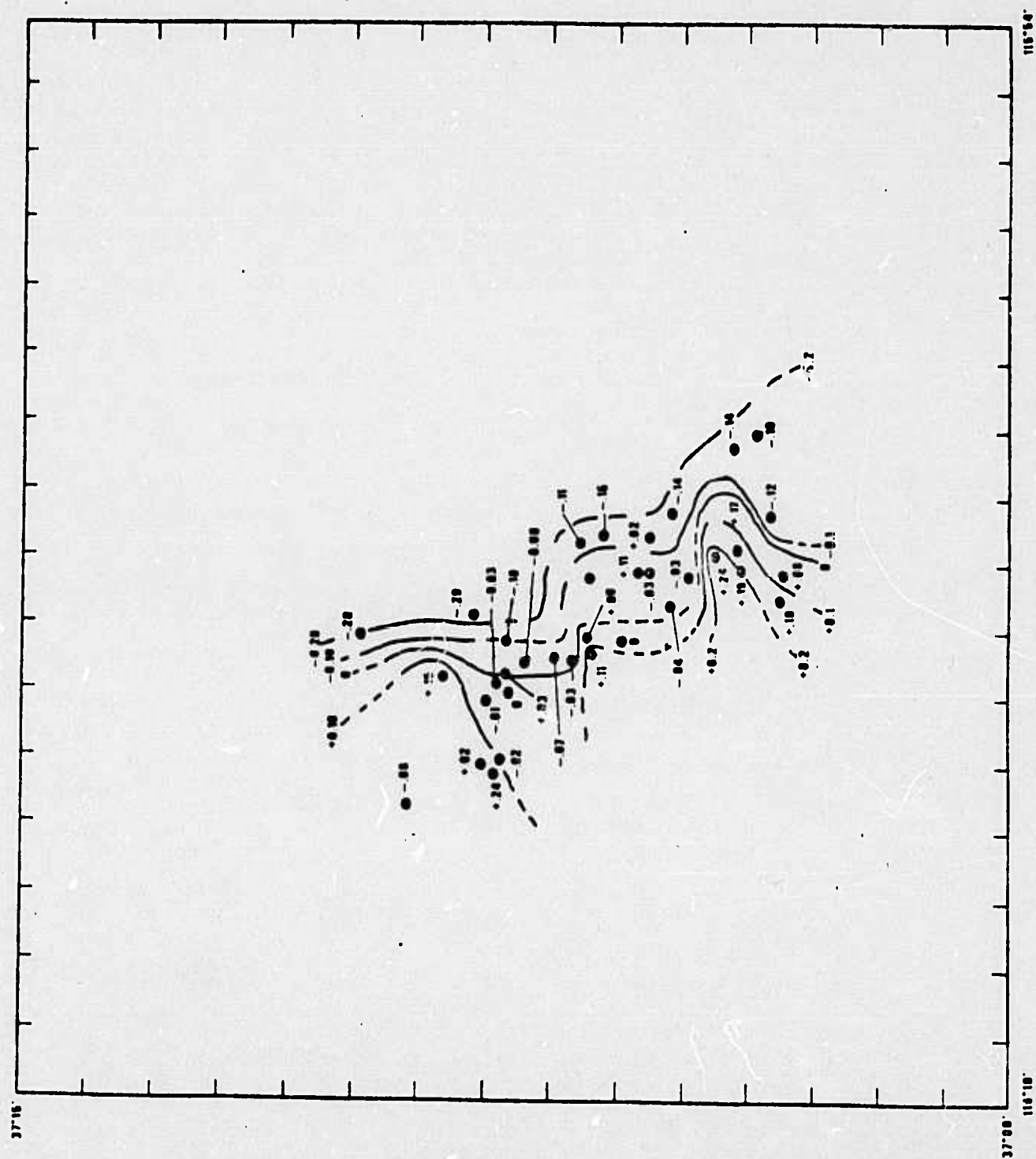


Figure 22. Spatial variations of NTS magnitudes at Yucca Flats.

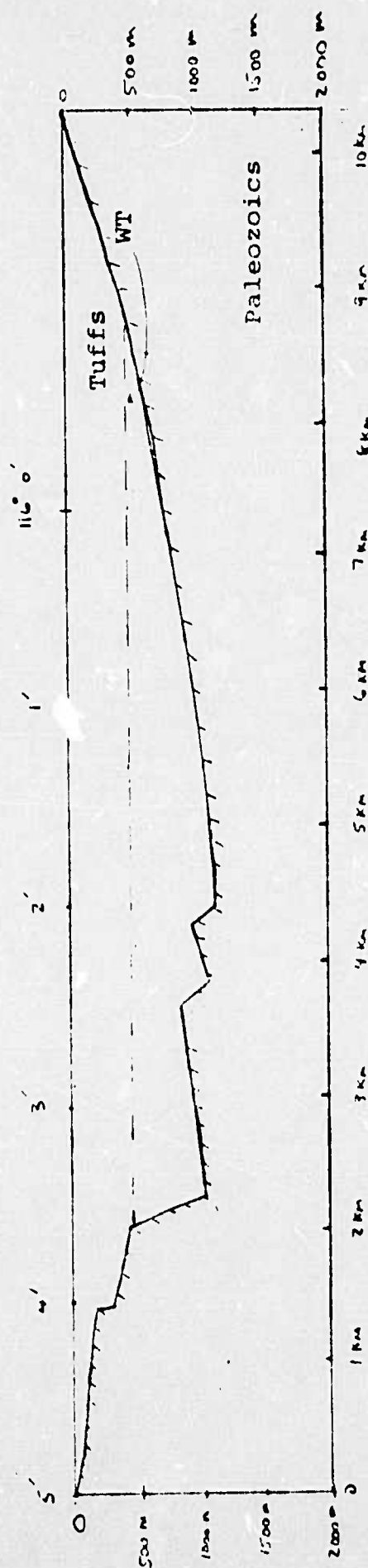
4.3 INTERPRETATION OF THE YF RECEIVER FUNCTIONS

The shallow crustal structure of Yucca Flats has been extensively studied by Herrin (1979) using a combination of gravity and seismic data. Based on this study, it is possible to develop a simplified crustal model for use in interpreting the receiver functions obtained in the previous section. The model used is shown in Figure 23. It consists basically of a tuff layer, dipping west, overlying a paleozoic basement. An additional, non-dipping discontinuity is introduced in the tuff layer by the presence of the water table. Further complications in the structure are introduced by the presence of faults near the westernmost station, YF4.

Both the glorified optics (G.O.) method of Hong and Helmberger (1978) and plane wave theory for simple dipping structure were used to derive synthetic receiver functions for this structure. The results of the G.O. calculations for one azimuth are shown in Figure 24. These results show reasonable qualitative agreement with the early portion of the observed receiver functions in Figure 17. The synthetics consist primarily of a direct arrival, a P reflection from free surface and then the water table, and a P reflection from the free surface and then the basement. Multiple reflections and converted phases are small and although included in Figure 24, the amplitudes are quite small. The amplitude of the water table and basement reflections agrees reasonably well with the average size of early negative reflections in the data, and the moveout exhibited by the basement reflection, relative to the water table reflection agrees with the data.

The application of the G.O. technique to the simplified basin structure produces a receiver function that approximates the early portion of the

East-West Profile Across Yucca Valley at 37 deg 1.6min North



Approximate velocities:

Tuffs above Water Table	1.5 Km/sec	density 2.0
Tuffs below Water Table	2.4 Km/sec	density 2.2
Paleozoics	5.0 Km/sec	density 2.6

Figure 23

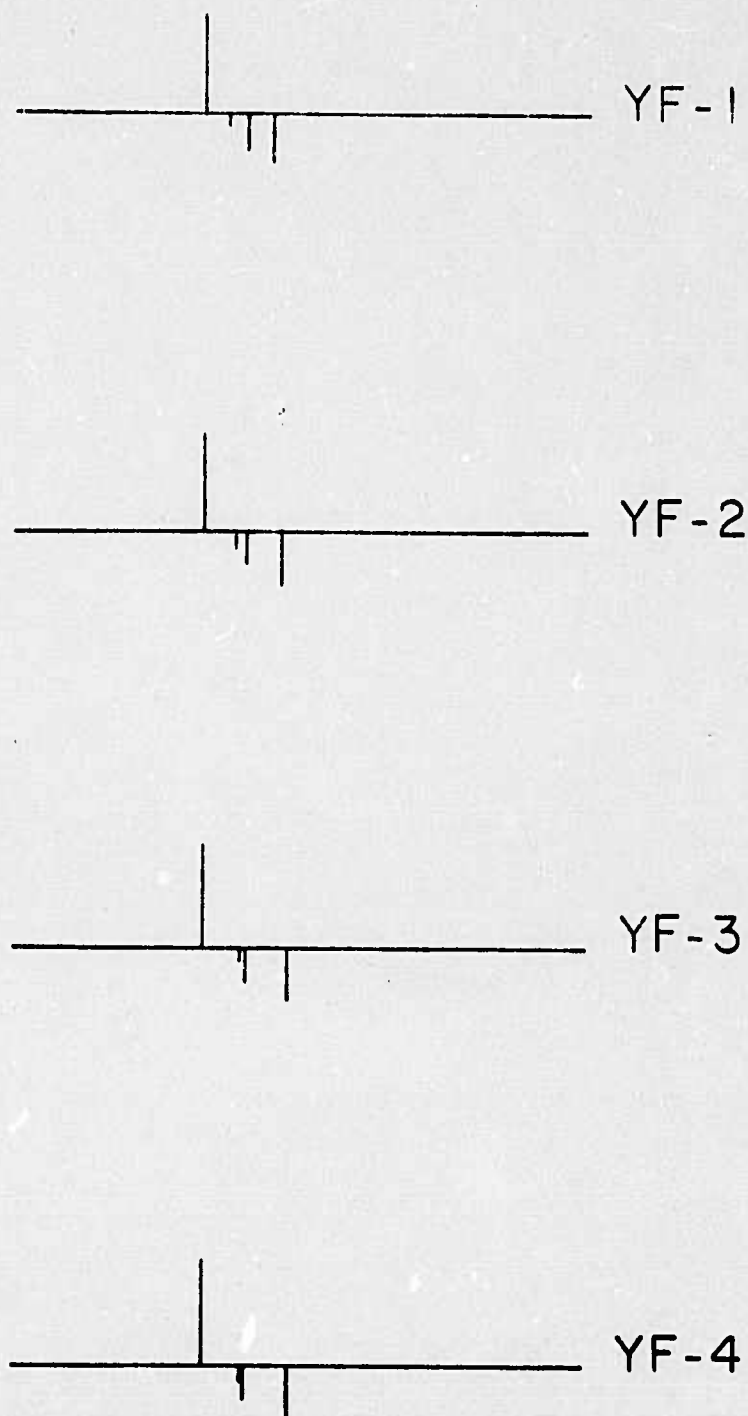


Figure 24. Delta function response for the 4 YF array stations calculated with the Glorified Optics technique for the structure shown in Figure 23.

observational receiver functions. However several details observed in the data are not predicted in the model. In particular, the simplified basin model does not predict at least one early negative reflection. Nor does this model correctly predict the timing between the first arrival and the water table reflection. Both of these discrepancies may be explained by the presence of a shallow sediment layer not included in the model. Somewhat more serious is the fact that the proposed model does not correctly predict the large observed station to station and azimuthal amplitude variations of the early reflected arrivals. Nor are any of the large arrivals following the early negative reflections predicted.

The failure of the model to account for the station to station amplitude variations of the receiver function is reflected by the failure to predict correct amplitude variations for synthetic seismograms constructed in a similar manner to those in Figure 20, but using a synthetic rather than an observed receiver function. As may be readily seen, seismograms in Figure 25 not only fail to show the structure of those in Figure 20, but also fail to show any significant station to station amplitude variation.

There are several possible causes for the discrepancies between observed and synthetic receiver functions. These include large lateral variations in alluvium and basement depth, irregularities in the basement, and systematic changes in the velocity of materials as a function of location in the basin. Several of these factors are known to exist. For instance, basement maps of Yucca Flats show a large closed depression in the basement several kilometers to the north of YFNV. Rays coming through this depression could well have their ray paths altered sufficiently to produce critical or near critical reflections from water table or basement layers. Similar effects may be associated with discontinuities

**Best
Available
Copy**

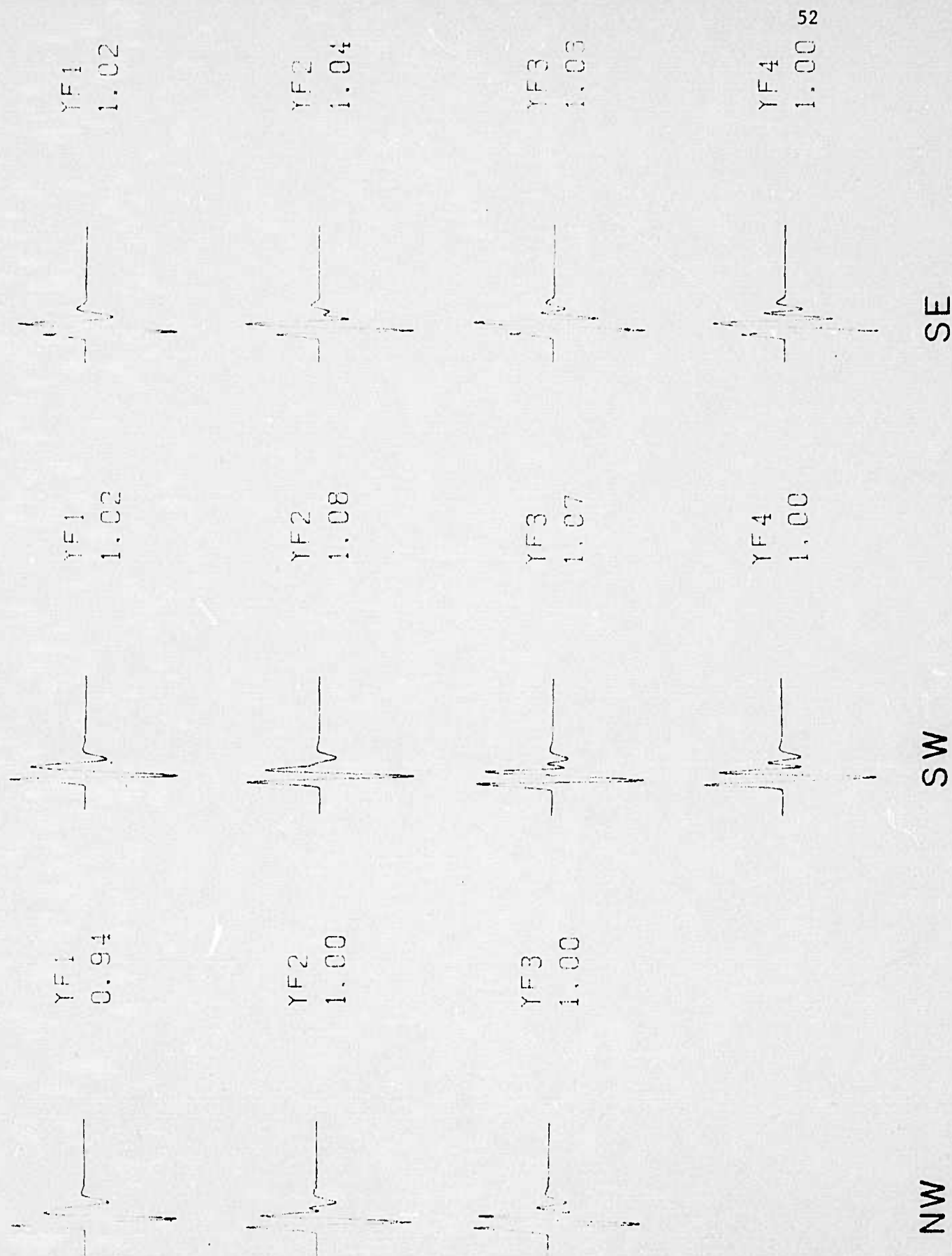


Figure 25. Synthetic short period P-wave predicted by the Glorified Optics receiver functions (e.g., see Figure 24) for an explosion source at three different azimuths (NW, SW, and SE). The seismograms are normalized independently for each azimuth. No arrivals can be seen at the YF 4 station from the northwest in the Glorified Optics calculation.

caused by faults which are known to occur in the region. In general, the only way to differentiate between these possible causes is to fully incorporate the detailed crustal models that are now being constructed into the modeling procedure.

V. STUDIES OF OUTGOING SEISMIC ENERGY FROM YUCCA FLATS, NTS

This section discusses waveform calculations for outgoing energy from sources located across the Yucca Flats basin and a comparison between some of these calculations with teleseismic observations Tijeras, Tan and Commodore. Earlier studies (Alewine, 1977) have detected an east-west magnitude variation for events located at Yucca Flats. In Section IV we demonstrated that the receiver functions for stations YF-1 through YF-4, computed from incoming teleseismic P-waves, result in a magnitude bias across the array of 0.1. It was the aim of this study to determine if the best current estimates of the shallow structure of the basin combined with the Glorified Optics (G.O.) technique of Hong and Helmberger (1978) could model the observed bias.

The basin structure shown in Figure 23 was used as the basis for computing the theoretical near source crustal response. This profile represents, in simplified form, the shallow basin structure near the YF array. The three-dimensional character of the basin was modeled by smoothly closing this structure to the north and south. The closure was based on data from stratigraphic maps of Yucca Flats. In the previous section receiver functions calculated from this structure were not in good agreement with the observational receiver functions. This model correctly predicts the relative amplitudes and moveout across the array of the first reflections from the water table and the basement complex. The calculated one way travel-time across the shallowest layer is systematically .15-.2 sec too long. In addition, one significant first multiple, negative polarity arrival is not predicted by the model. Finally, a large positive arrival, arrival time = 1.2 sec after the first P-wave is also not predicted by the model. The inadequacy of the model to

account for the complexity of the observed receiver function suggests the model may not describe in sufficient detail the structures that control the magnitude bias observed at Yucca Flats. The Glorified Optics technique has been shown in previous tests to adequately model wave propagation in smoothly varying three dimensional structures (Hong and Helmberger, 1978). The technique retains information on the amplitude, timing and phase distortion (critical reflections) of geometric rays. The technique does not model diffracted wave propagation. Hence, to the extent that diffracted energy is important to the complete modeling of the structure, G. O. will be inadequate. Within this project, discontinuous fault structures have been modeled as slightly smoothed structures. The normal faults in the center of the basin have been replaced with half cosine functions that deviate from the structure shown in Figure 23 by less than a hundred meters. The structure used in the computer program and the ray paths for the four most significant rays are shown in Figure 26.

In the initial stages of calculating the elastic response of the basin, for both the vertical component for incoming teleseismic energy and outgoing P-waves from local sources, a large family of rays was examined. For the Yucca Flats structure, G.O. predicts that converted phases (e.g. P-waves converted at a boundary to S-waves and then later converted back to P-waves) are relatively unimportant. This suggests that the receiver functions calculated from incoming teleseismic P-waves should provide a good estimate of the outgoing wave shapes provided the function is corrected for the effect of source depth. To a first approximation, this can be accomplished by adding in the phase pP . This approximation clearly assumes that reflections from layers between the source and the surface are negligible. The event

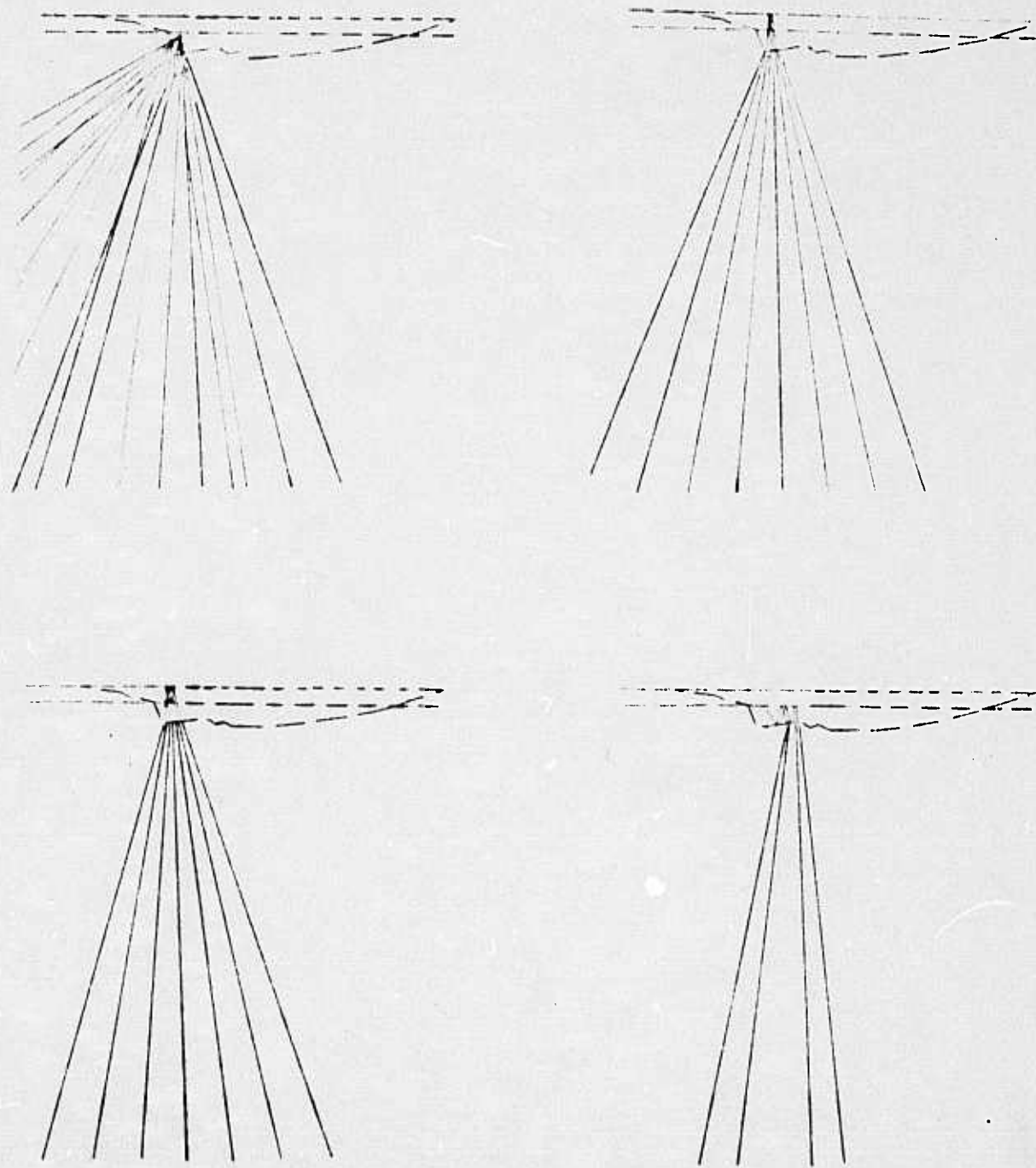


Figure 26. Four principal rays used in the Glorified Optics analysis of outgoing seismic energy from Yucca Flats.

Tijeras was located midway between stations YF-1 and YF-2. Synthetic waveshapes have been calculated using the receiver functions from Section IV for the WWSSN stations COL, MAT and ARE, Figure 27. The receiver function for the northwest azimuth from YF-1 was used for COL and the receiver function for YF-2 was used for MAT. The ARE waveform was generated with the south-east function for YF-1. As may be seen in Figure 27, the timing and amplitude of the first four peaks and the approximate amplitudes and timing of later arrivals fit quite well. This result confirms the predictions from the G.O. calculations that for a simple or smooth structure such as exists in the eastern portion of Yucca Flats, converted phases are not important.

An example of the waveshape calculated with G.O. for a source located approximately at YF-1 is shown at the top of Figure 25. This synthetic contains a von Seggern and Blandford (1972) source, a WWSSN short period instrument response and an attenuation operator ($t^* = 1.0$). The relative amplitudes of the first five peaks are in fair agreement with the synthetics calculated from the receiver function for YF 1, Figure 27, COL.

The event Tan was located about 1 km south of the station YF 4 and was juxtaposed to the Yucca fault system. The source depth was roughly the same as Tijeras and the emplacement media was similar. As seen in Figure 28, the teleseismic waveforms from Tan are considerably more complex than was observed for Tijeras. Further, this degree of complexity cannot be obtained from any of the receiver functions from Section IV. The event Commodore is located well north of the YF stations, on the opposite side of the mapped Yucca fault and shows marked similarity in waveform to Tan, Figure 28. This argues strongly that the complex waveforms that characterize events located in the western portion of the basin are not simply associated with geometric rays. Calculated amplitudes and waveforms from G.O. for

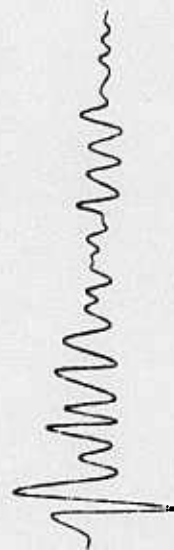
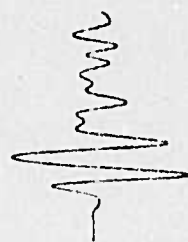
TIJERAS

DATA

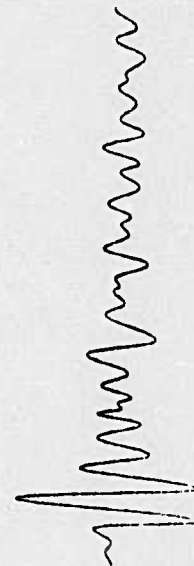
SYNTHETIC



COL



MAT



ARE

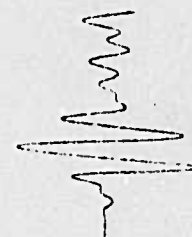


Figure 27. Short period P waves observed at three WSSN stations from the NTS event Tijeras and synthetic P waves generated by convolving a von Seggern and Blandford source with the appropriate YF receiver function.

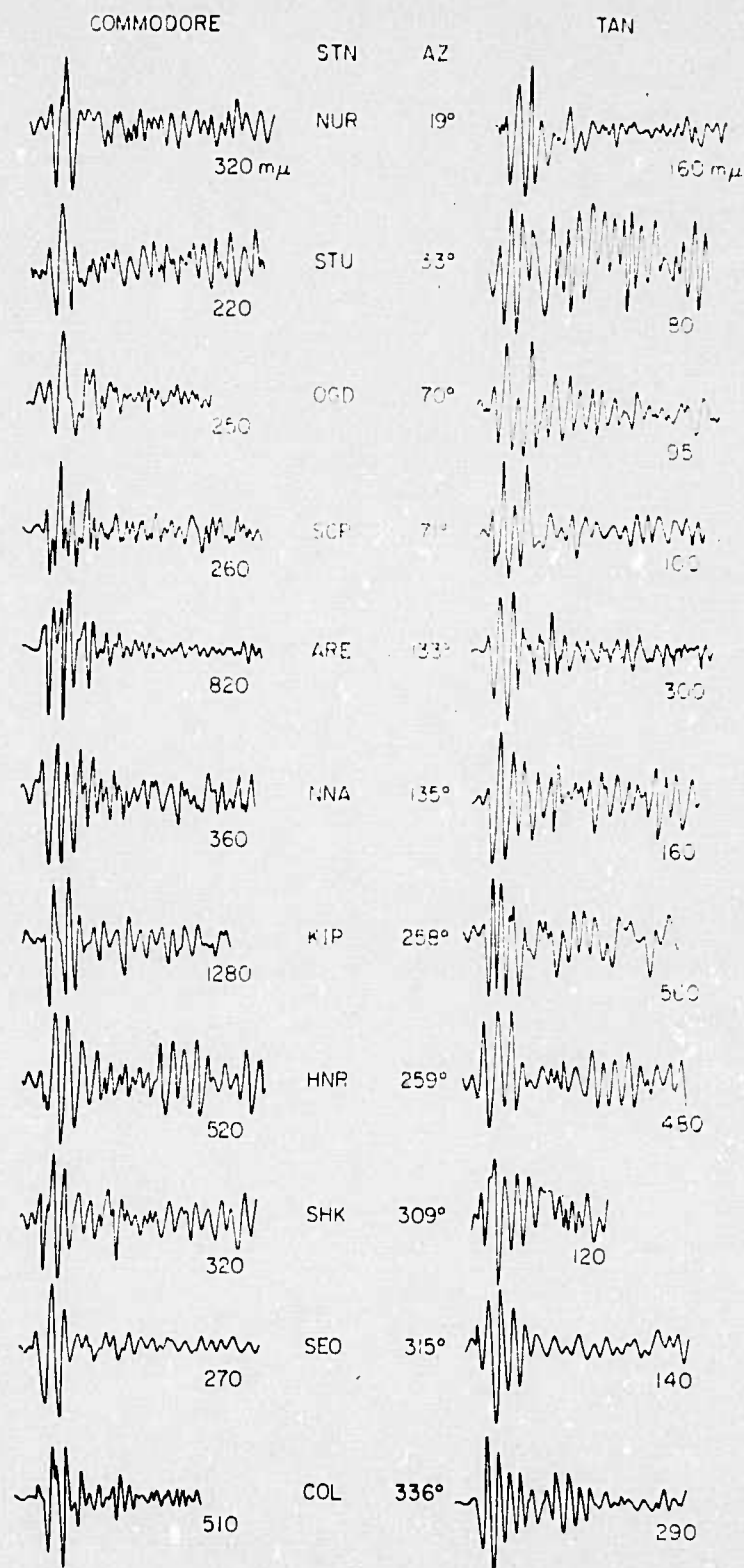


Figure 28. Observed short period P-waves from the NTS events Commodore and Tan.

sources located in the vicinity of the faults change rapidly with small changes in position and azimuth, Figure 25. This is in conflict with the apparent similarity of the waveshapes for events Tan and Commodore and with the general pattern of magnitude bias discussed by Alewine (1977).

The goal of this task has been to combine the available computer code for three-dimensional wave propagation with the velocity model for Yucca Flats in order to investigate the origins of the magnitude bias discussed by Alewine (1977). The general conclusion at this time is that the forward calculations with G.O. and the basin model shown in Figure 23 cannot explain the observed magnitude bias. At least three possible causes for this failure exist. First, the model may be inadequate. The discussions in Section IV show that several arrivals observed in the receiver functions are not predicted by the model. If the magnitude bias is controlled by elastic wave propagation in the basin, then the apparent inadequacy of the model is very disappointing. It seems unlikely that we will have information even as detailed as that shown in Figure 23 for Russian test sites. A second possible explanation is that magnitude bias may be to first order the result of coupling at the source and not strongly dependent upon the basin structure. Material properties within the basin could grade from east to west. However, the receiver functions calculated from the observed teleseismic P-waves predict a 0.1 magnitude bias across the YF array that is consistent with the results from Alewine (1977). This leads us to believe that the basin structure does play an important role in the observed magnitude bias. As a third explanation, G.O. does not include diffracted wave propagation effects. The attempts to model teleseismic waveforms for sources located near the Yucca fault show that the technique is inadequate for such complex structures and further

suggests that diffraction is an important aspect of this problem. During FY 80, Sierra Geophysics is developing a more advanced technique for wave propagation in complex media that retains diffracted effects.

VI. AMPLITUDE STUDIES OF THE STATIONS OB2, RKON AND HNME RELATIVE TO THE WWSSN MEAN

This section examines in detail the amplitude anomalies at the SDCS stations HNME at Houlton, Maine; RKON at Red Lake, Ontario; and OB2-NV at the Climax Stock, NTS. These amplitude anomalies are determined relative to the suite of WWSSN stations in the coterminous United States. A complete study of amplitude anomalies associated with these WWSSN stations is presented in the technical report SGI-R-79-011. This section will deal only with the three aforementioned SDCS stations and their relationship with the WWSSN stations in the United States.

Figure 29 shows the location of WWSSN stations in the United States relative to the approximate physiographic provinces. Relative amplitude anomalies were determined for these stations for seismic sources from three separate azimuths. To the north, Russian nuclear explosions located in five separate Russian test sites were utilized. In all, high quality data from thirty-six Russian explosions were obtained. The events and their locations are listed in Table 2. The amplitude measurement utilized in this study was the peak-to-peak amplitude of the first cycle of P-wave motion as measured on the short period vertical component of each seismogram. As explosions have theoretically spherically symmetric radiation patterns, no corrections for source radiation were necessary. To obtain amplitude coverage in other azimuths for receivers in the United States, earthquake sources must be utilized. However, earthquakes have an amplitude radiation pattern due to the double couple nature of the source and may also exhibit directivity effects due to the propagation of the fault. To minimize these effects, earthquakes were sought which were simple and short-

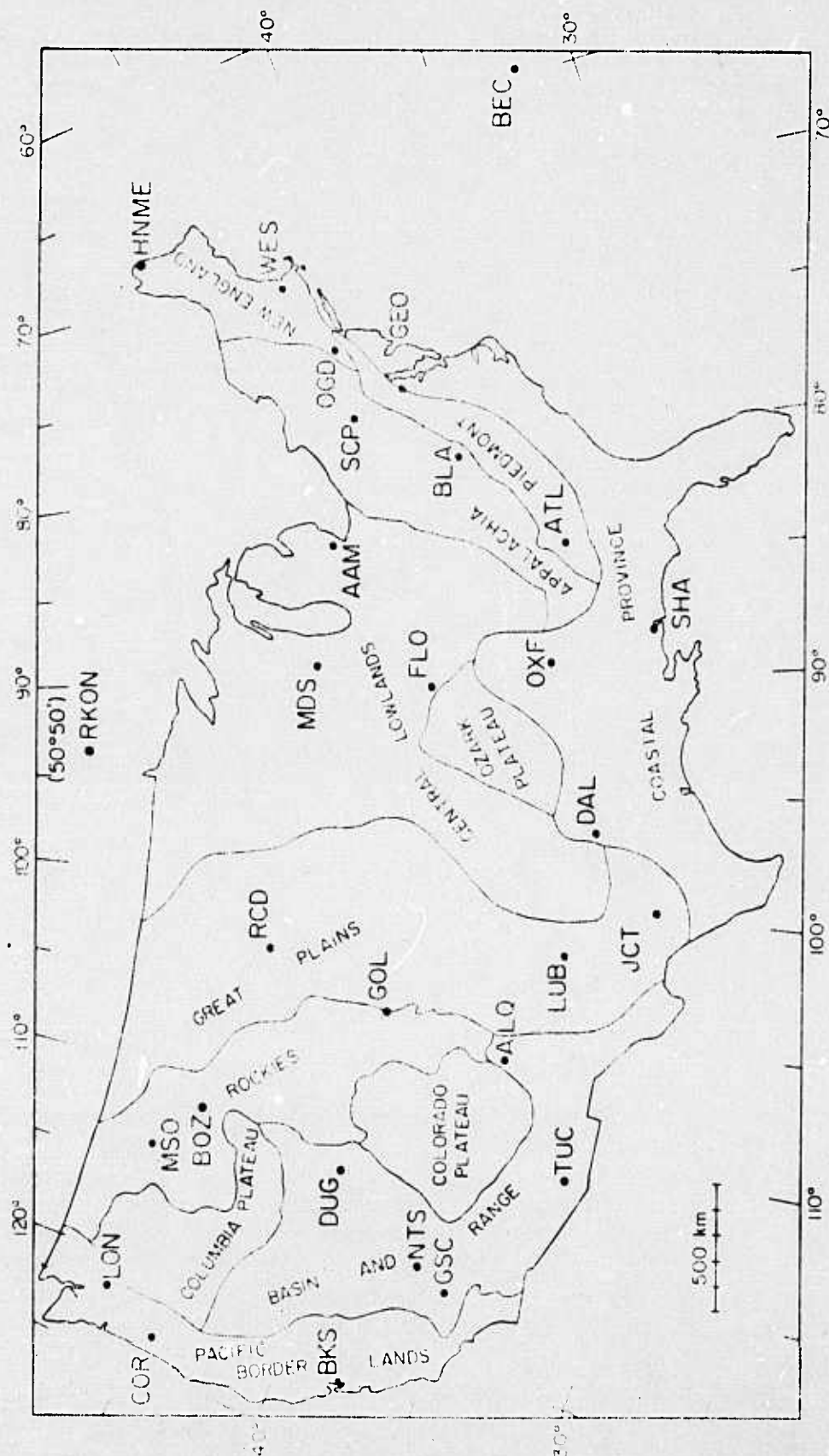


Figure 2j. Locations of WSSN and SDCS stations in the United States relative to approximate physiographic provinces. SDCS station OB2 is located at the point labeled NTS.

Table 2

Explosion Data Set*

Northern Novaya Zemlya

27 Oct 66	5:57:58	73.44N	54.75E
21 Oct 67	4:59:58	73.37N	54.81E
7 Nov 68	10:02:05	73.40N	54.86E
14 Oct 69	7:00:06	73.40N	54.81E
14 Oct 70	5:59:57	73.31N	55.15E
27 Sept 71	5:59:55	73.39N	55.10E
28 Aug 72	5:59:57	73.34N	55.08E
12 Sept 73	6:59:54	73.30N	55.16E
29 Aug 74	9:59:56	73.37N	55.09E
23 Aug 75	8:59:58	73.37N	54.64E
21 Oct 75	11:59:57	73.35N	55.08E

Southern Novaya Zemlya

27 Sept 73	6:59:58	70:76N	53.87E
2 Nov 74	4:59:57	70:82N	54.06E
18 Oct 75	8:59:56	70:84N	53.69E

Semipalatinsk East

15 Jan 65	5:59:59	49.89N	78.97E
30 Nov 69	3:32:57	49.92N	79.00E
2 Nov 72	1:26:58	49.91N	78.84E
23 Jul 73	1:22:58	49.99N	78.85E
14 Dec 73	7:46:57	50.04N	79.01E
31 May 74	3:26:57	49.95N	78.84E
4 Jul 76	2:56:58	49.91N	78.95E

Semipalatinsk East-Additional Data

23 Nov 76	5:03:00	50.00N	79.00E
7 Dec 76	4:57:00	49.90N	78.90E
29 May 77	2:59:00	49.90N	78.90E

Table 2 (continued)

Semipalatinsk West

19 Oct 66	3:57:58	49.75N	78.03E
20 Apr 67	4:07:58	49.74N	78.12E
17 Oct 67	5:03:58	49.82N	78.10E
29 Sept 68	3:42:58	49.77N	78.19E
28 Jun 70	1:57:58	49.83N	78.25E
22 Mar 71	4:32:58	49.74N	78.18E
25 Apr 71	3:32:58	49.82N	78.09E
30 Dec 71	6:20:58	49.75N	78.13E
20 Feb 75	5:32:58	49.82N	72.08E

Kazakh

6 Dec 69	7:02:57	43.83N	54.78E
12 Dec 70	7:00:57	43.85N	54.77E
23 Dec 70	7:00:57	43.83N	54.85E

*Locations and origin times from Dahlman and Israelson (1977), or Bulletin of the International Seismological Centre.

duration in character. That is, the pulses as observed on short period records across the United States were similar in waveform, short in duration, all had the same first motions, and were similar in frequency content.

Table 3 lists earthquakes at a northwest azimuth. These earthquakes occur in the Kurile Islands region, in Japan, the Izu-Bonin Islands, the Alaskan peninsula, and other places in Northeast Asia. Earthquake data from a southeast azimuth are listed in Table 4 and are comprised of South American events.

Earthquake data in two time periods were used in this study. Simple earthquakes in the Kurile Islands region and in South America were obtained for the period 1966 through 1968. A second selection of simple earthquakes were chosen from the period September 1976 and August 1977. Table 5 lists the events and SDCS seismograms utilized in the tie to the WWSSN stations.

Figure 30 plots the amplitude response of the WWSSN short period instrument. Figures 31, 32, and 33 plot the amplitude responses of the SDCS stations utilized in this study. To provide a standard basis of comparison of these data, appropriate filters were constructed to change the instrument response of the SDCS stations to the response of the WWSSN stations. To illustrate the band response of the instruments relative to sources used in this study, Figure 34 plots the power of the Piledriver explosion source at NTS relative to frequency. Figure 35 illustrates the effect of filtering the SDCS seismogram at OB2-NV to have the same response as a WWSSN short period instrument.

Three examples of the earthquake data utilized in this study are shown in Figures 36, 37, and 38. Figure 36 plots a deep focus earthquake in Kamchatka on April 22, 1977. The frequency content of the record at RKON is slightly

TABLE 3
Earthquakes in a Northwest Azimuth*

<u>Date</u>	<u>Origin Time</u>	<u>Location</u>	<u>Depth (km)</u>
<u>Kurile Islands Earthquakes</u>			
11/22/66	6:29:52.4	48.0N 146.8E	443
3/20/67	12:31:34.0	45.6N 151.4E	51
8/10/67	11:21:22.3	45.4N 150.3E	37
2/10/68	10:00:05.8	46.0N 152.3E	87
4/28/68	4:18:15.7	44.8N 174.5E	39
7/25/68	10:50:31.5	45.7N 146.7E	16
10/26/76	5:58:56	46.1N 159.7W	130
3/19/77	10:56:06	43.0N 149.0E	0
<u>Japanese Earthquakes</u>			
1/1/77	11:33:42	30.6N 137.2E	483
1/5/77	22:44:57	23.3N 143.8E	0
2/18/77	20:51:26	34.0N 143.0E	0
6/12/77	8:48:05	43.0N 142.3E	241
<u>Bonin Islands Earthquakes</u>			
9/22/76	8:20:28	23.3N 142.1E	110
12/5/76	22:01:22	23.0N 140.0E	393
12/22/76	1:01:42	24.0N 145.0E	0
1/5/77	22:44:57	23.3N 143.8E	0

TABLE 3 continued
Earthquakes in a Northwest Azimuth*

<u>Date</u>	<u>Origin Time</u>	<u>Location</u>	<u>Depth (km)</u>	<u>Region</u>
<u>Other Events</u>				
10/22/76	18:35:24	56.1N 153.3W	0	Kodiak Islands
4/22/77	0:58:56	52.5N 138.8E	408	Kamchatka
4/23/77	14:49:06	75.0N 134.9E	0	New Siberian Is.
7/20/77	13:24:21	50.6S 161.9W	0	Alaska Pen.
8/7/77	23:26:55	52.2N 176.2W	125	Andreanof Is.

*Locations Before 1975 from International Seismological Centre, after 1975 from Seismic Data Analysis Center.

TABLE 4
South American Earthquakes*

<u>Date</u>	<u>Origin Time</u>	<u>Location</u>	<u>Depth (km)</u>
4/25/67	10:26:14.3	32.6N 69.0W	39
11/15/67	21:35:51.5	28.7S 71.2W	15
2/6/68	11:19:23.1	28.5S 71.0W	23
4/21/68	9:24:35.5	23.4S 70.5W	41
4/30/68	23:51:17.9	38.4S 71.1W	40
9/30/76	8:04:11	24.2S 68.2W	0
12/3/76	5:27:34	21.0S 69.0W	79
12/4/76	12:32:35	20.0S 69.0W	103
3/8/77	22:46:44	8.0S 63.0W	0
3/13/77	4:55:55	2.0S 58.0W	0
4/15/77	23:35:38	22.9S 68.8W	109
6/2/77	16:50:36	29.9S 68.6W	94
6/5/77	2:46:07	24.0S 70.5W	30
6/8/77	13:25:16	22.1S 67.3W	135
6/18/77	16:49:42	21.0S 68.7W	125

*Locations Before 1975 from International Seismological Centre, after 1975 from Seismic Data Analysis Center.

Table 5

SUMMARY OF EVENTS & SEISMOGRAMS USED IN TYING SDGS
STATIONS TO WWSSN

Event	SDAC Seismogram Number		
	<u>OB2NV</u>	<u>RKON</u>	<u>HNME</u>
11/23/76		34029	34031
12/4/76		33789	
12/7/76		33857	33859
12/5/76		33797	
12/22/76	33923		
12/31/76	33947	33943	
4/15/77	34657	34659	35147
4/22/77	34695		
4/23/77	34705	34703	
5/29/77	35231	35229	35233
6/2/77	35206	35205	
6/5/77	35168	35169	35170
6/8/77	35191		
6/12/77	35285	35287	
6/18/77	36493		
6/21/77	35425		
7/20/77	35483	35485	35487
8/7/77	35841		

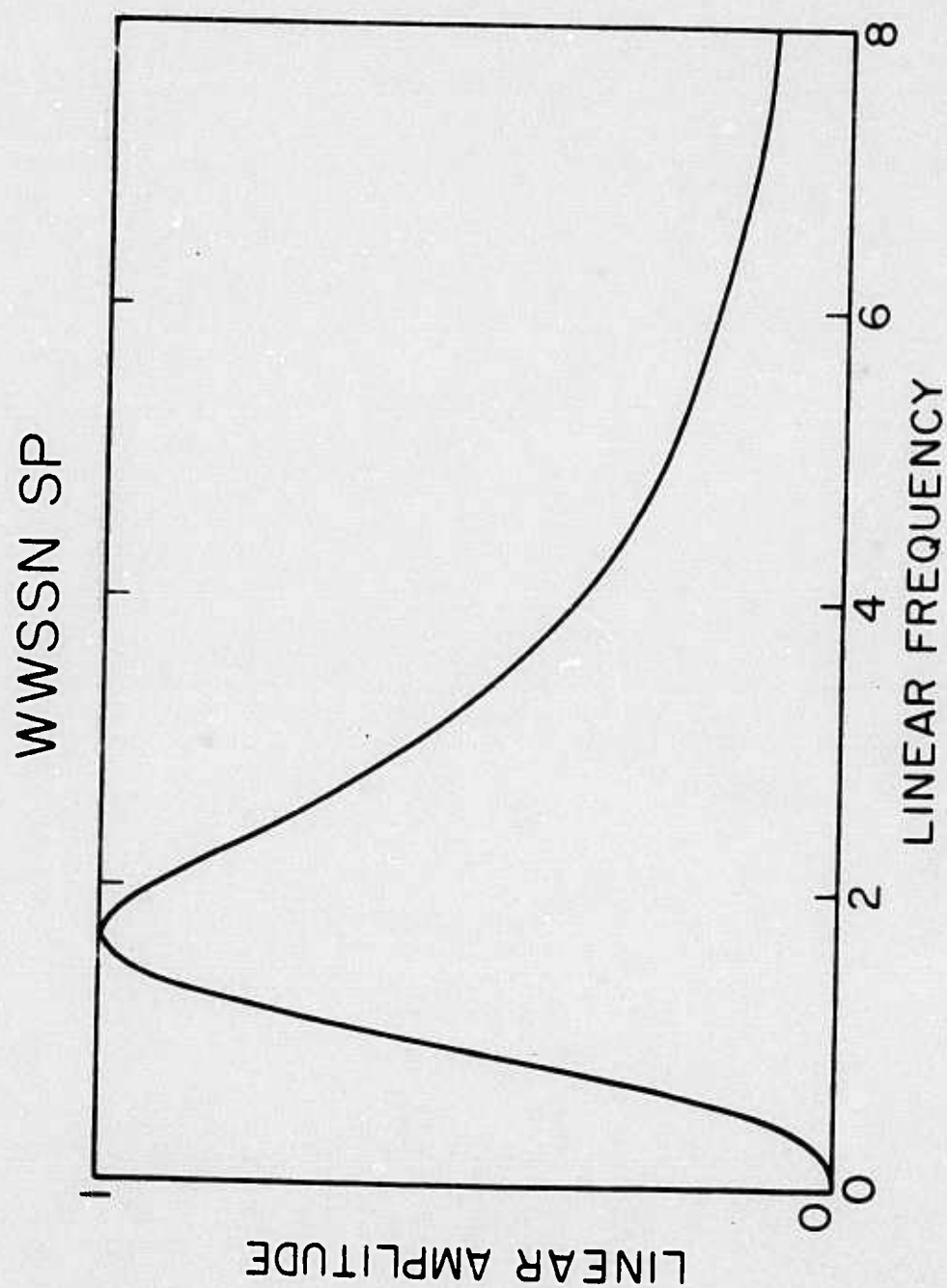


Figure 30. The amplitude response of the WWSSN short period instrument.

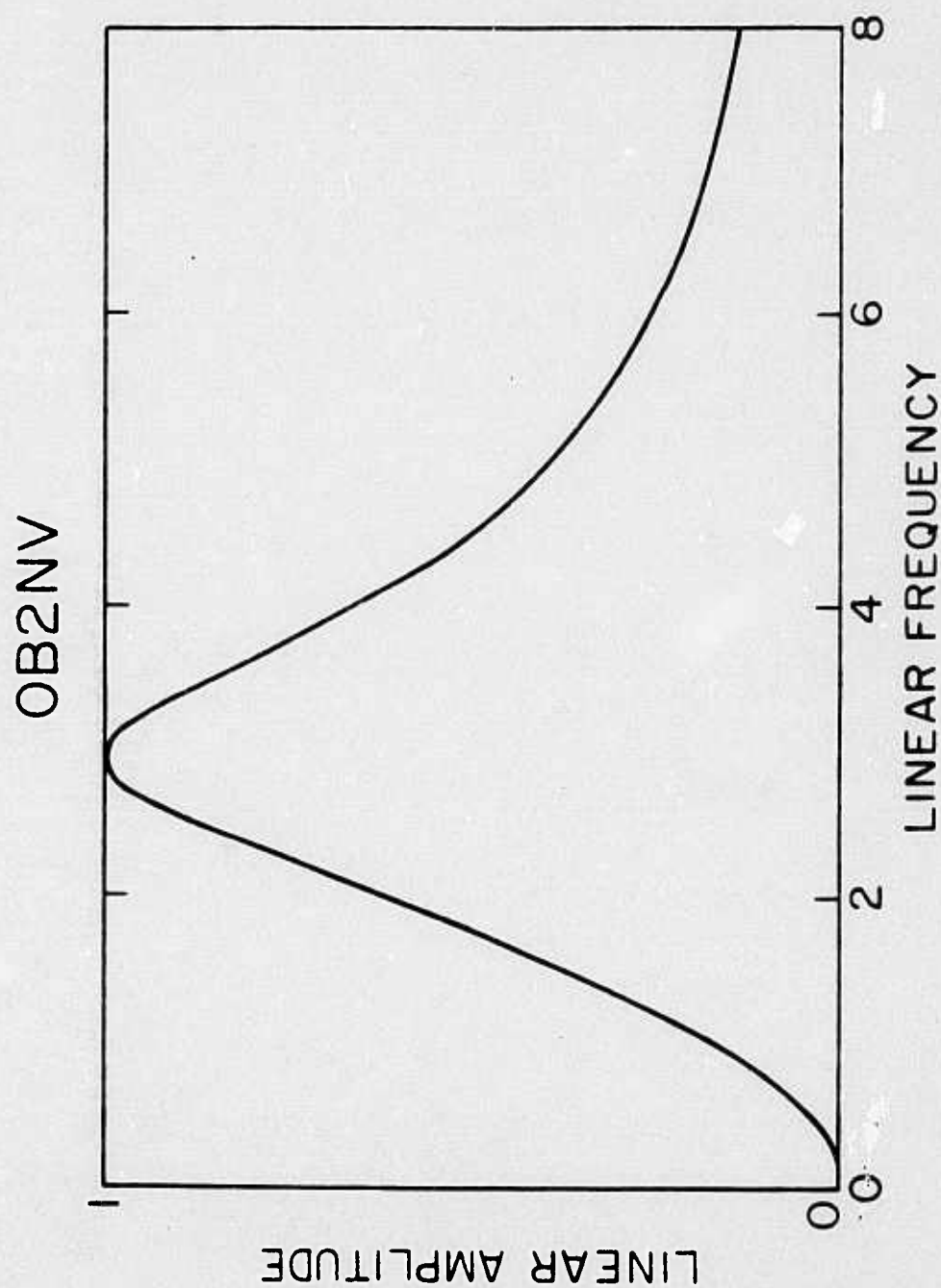


Figure 31. The amplitude response of the SDCS station OB2-NV, located at Climax Stock in the Nevada Test Site.

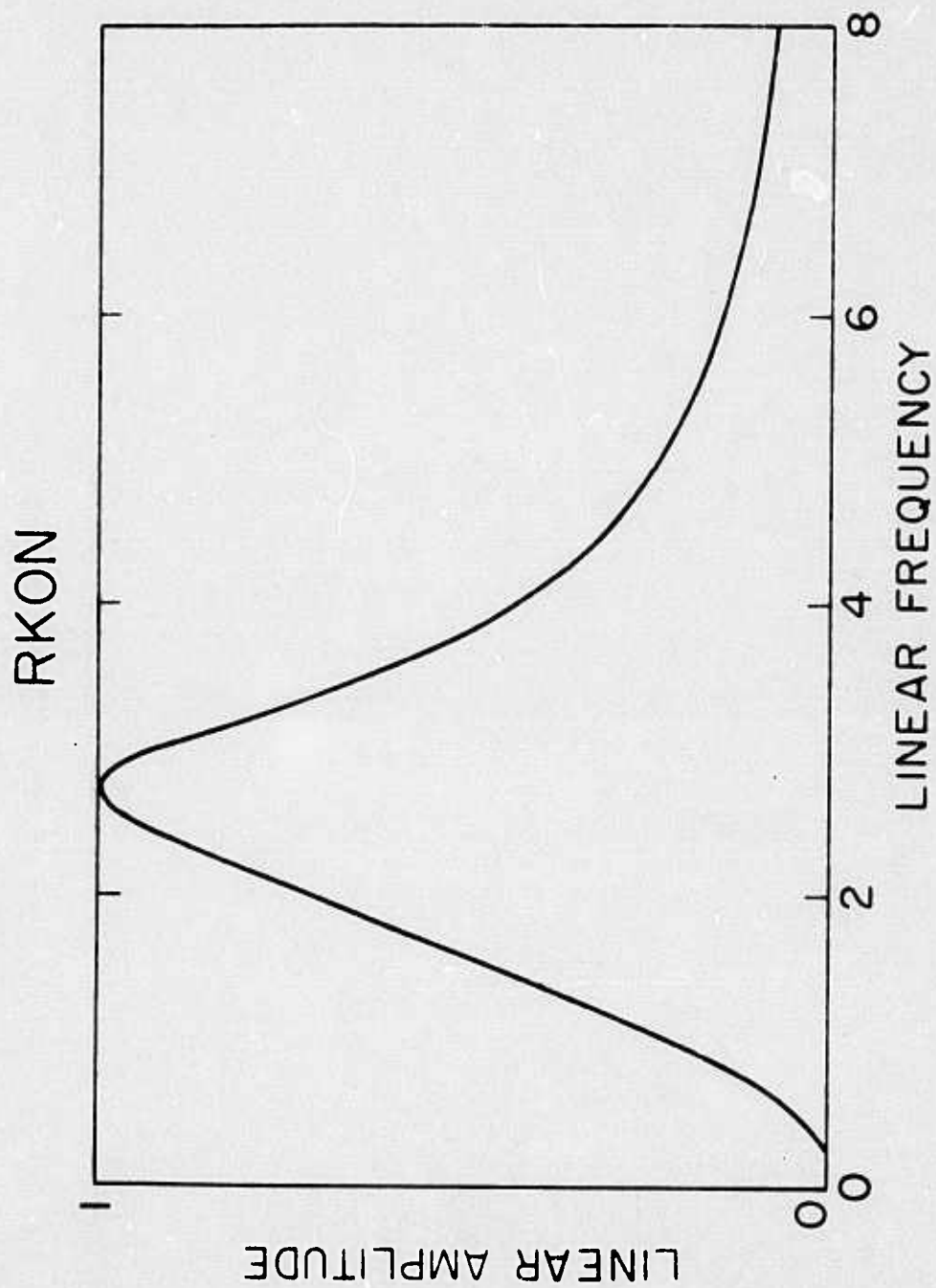


Figure 32. The amplitude response of the SDCS station RKON located at Red Lake, Ontario.

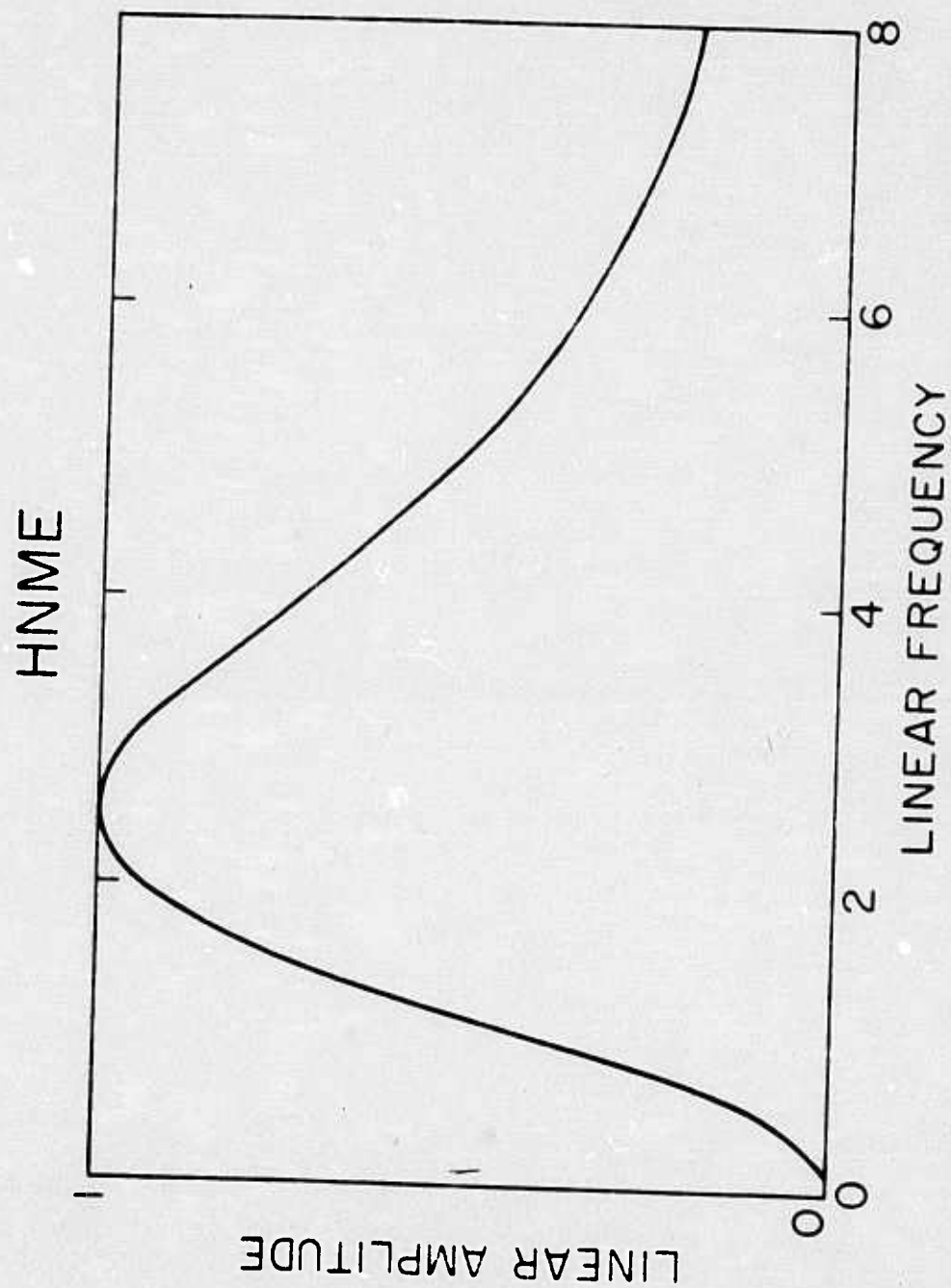


Figure 33. The amplitude response of the SDCS station HNME located at Houlton, Maine.

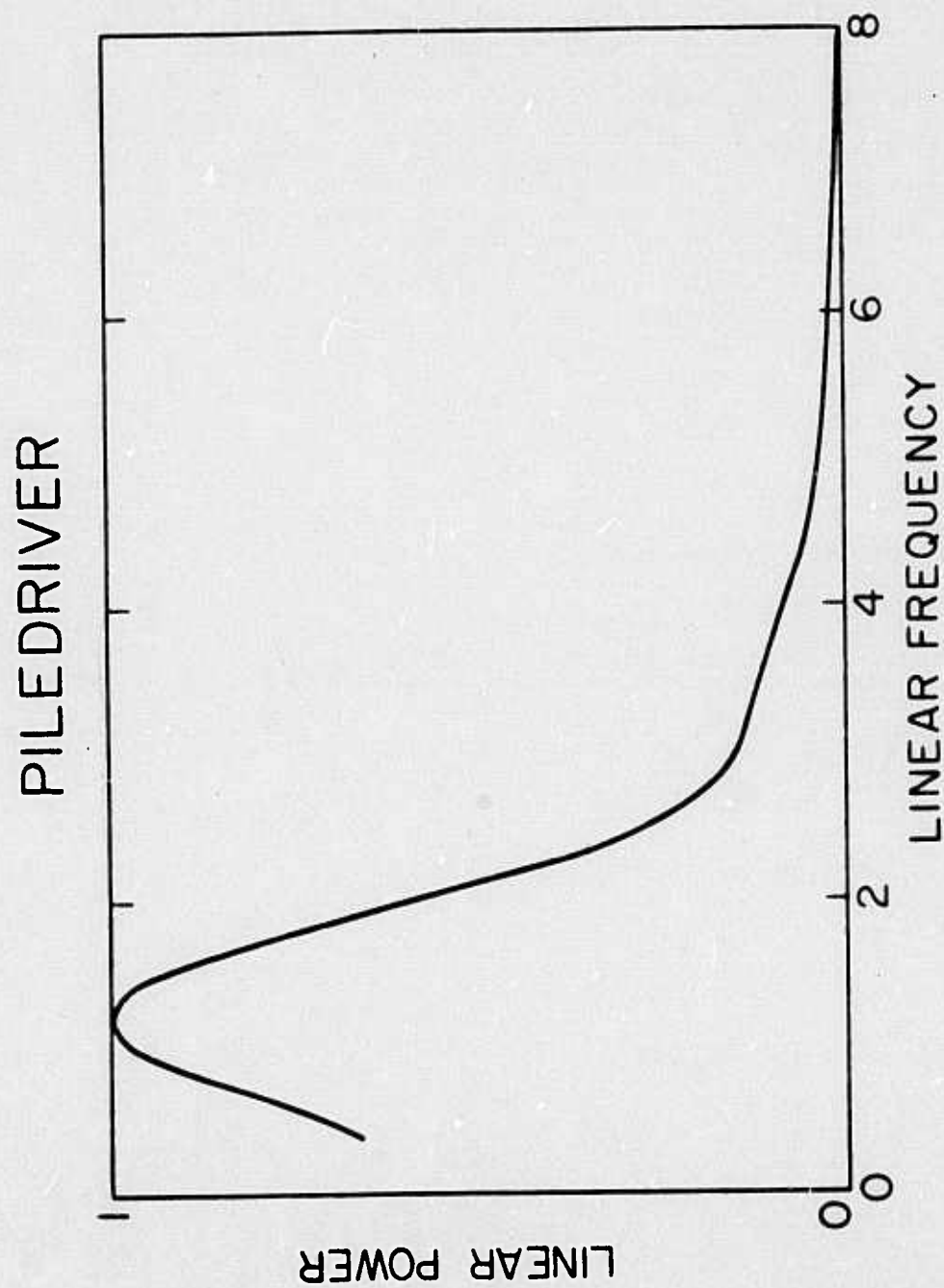


Figure 34. The teleseismic power response of the Piledriver explosion source.

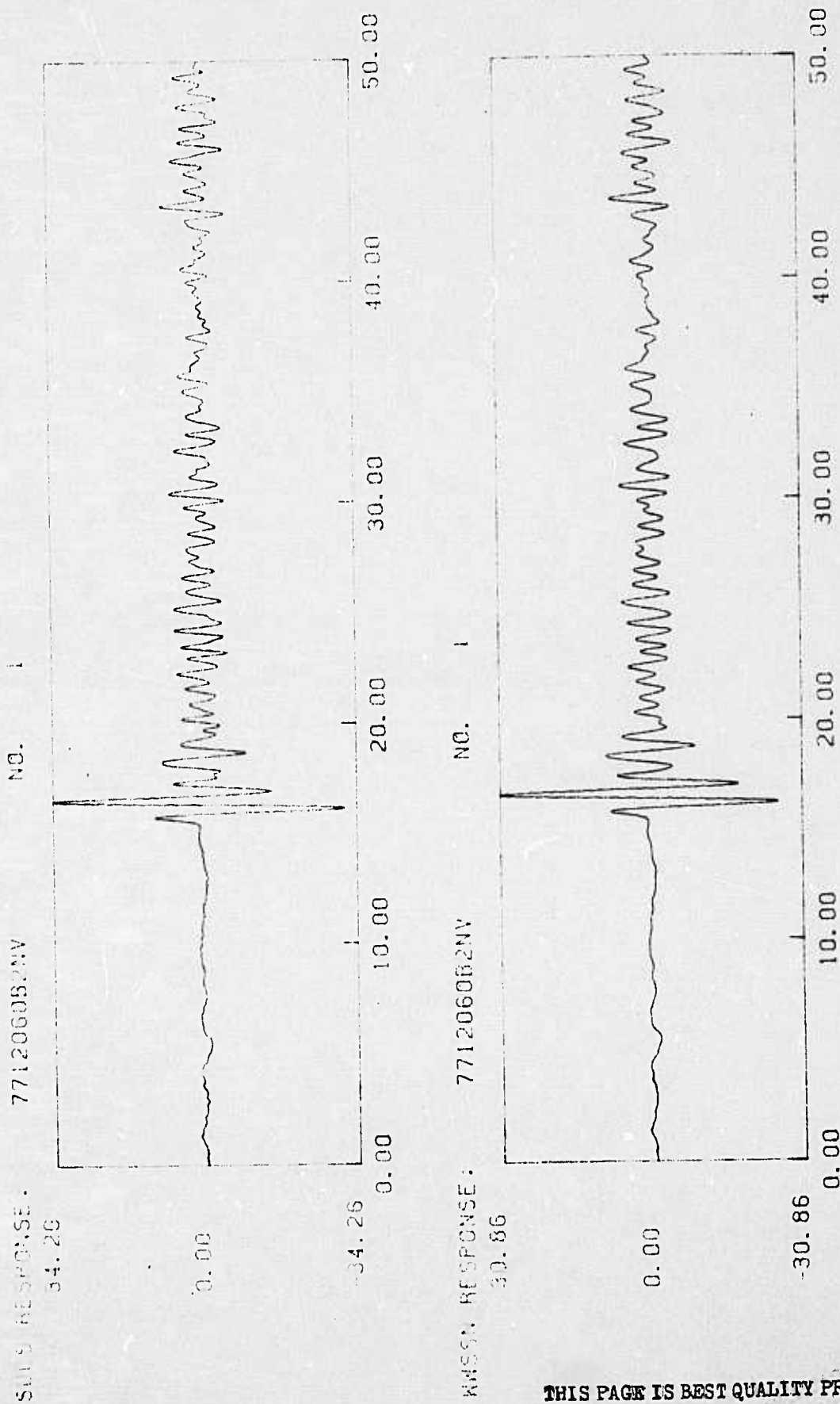


Figure 35. The effect of filtering an SDCS seismogram to have the same instrument response as a WSSN instrument.

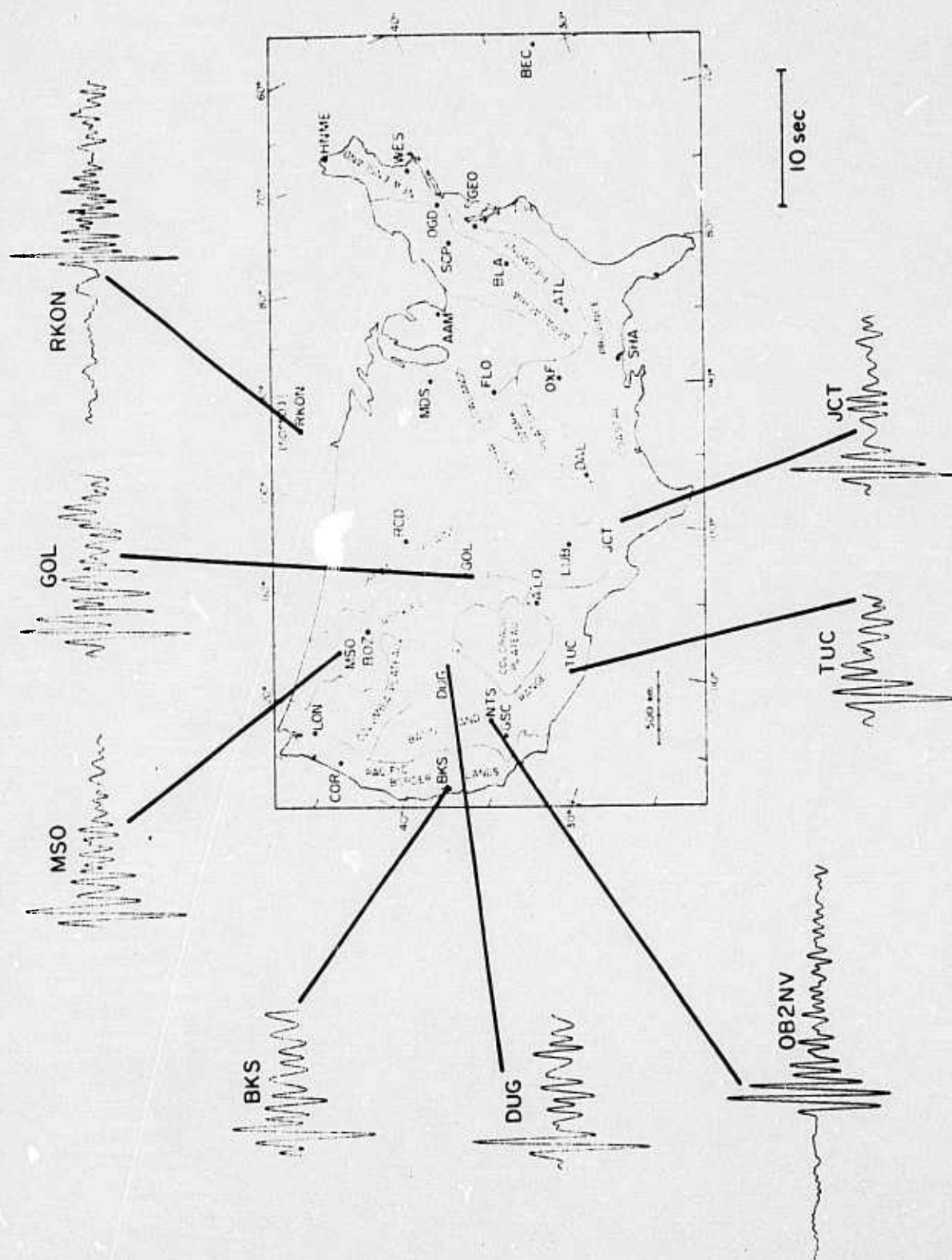


Figure 36. WSSN seismograms and filtered SDCS seismograms for a deep-focus earthquake in Kamchatka occurring on April 22, 1977.

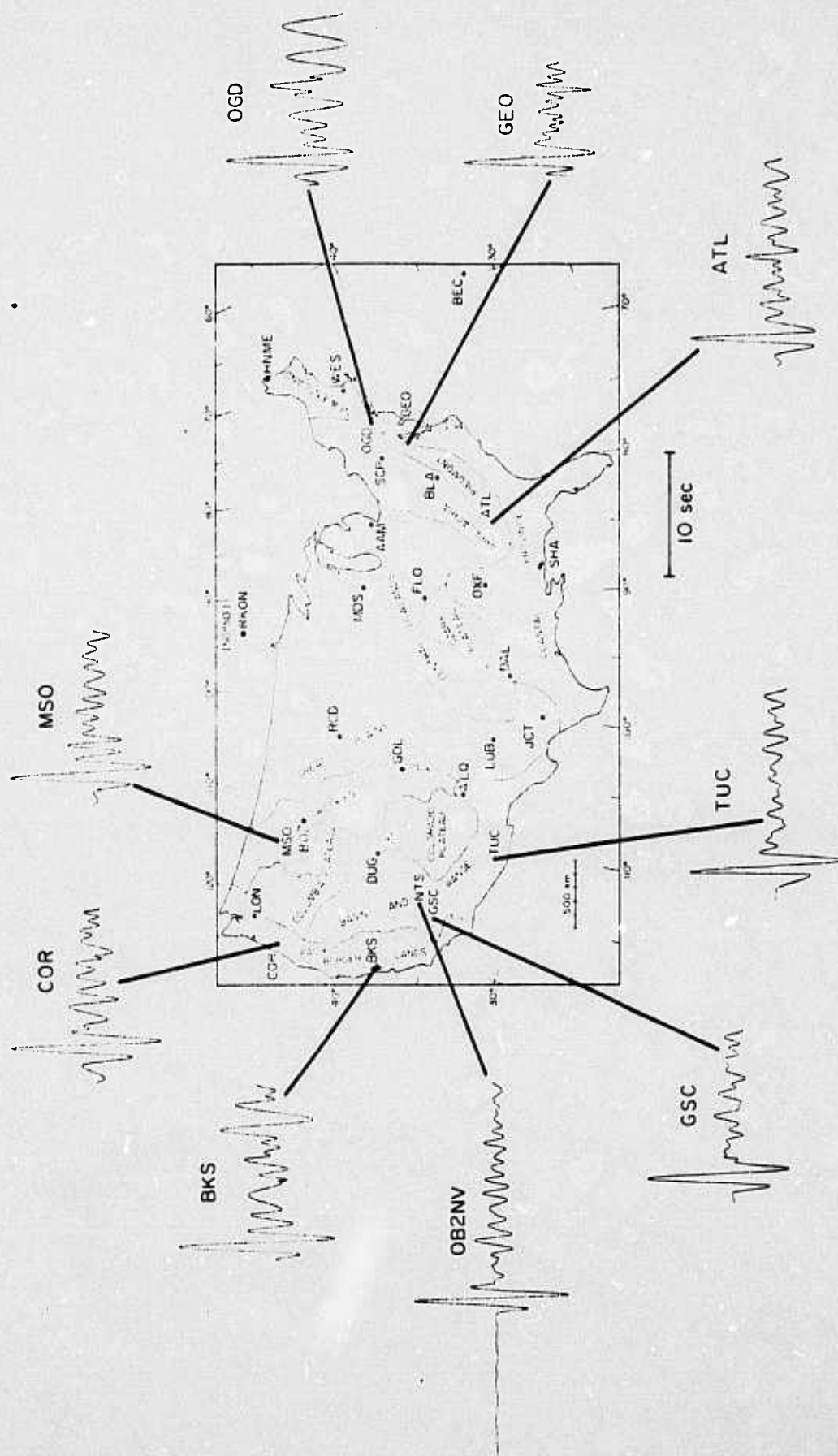


Figure 37. WSSN seismograms and filtered SDCS and a filtered SDCS seismogram for an intermediate depth earthquake in South America on June 8, 1977.

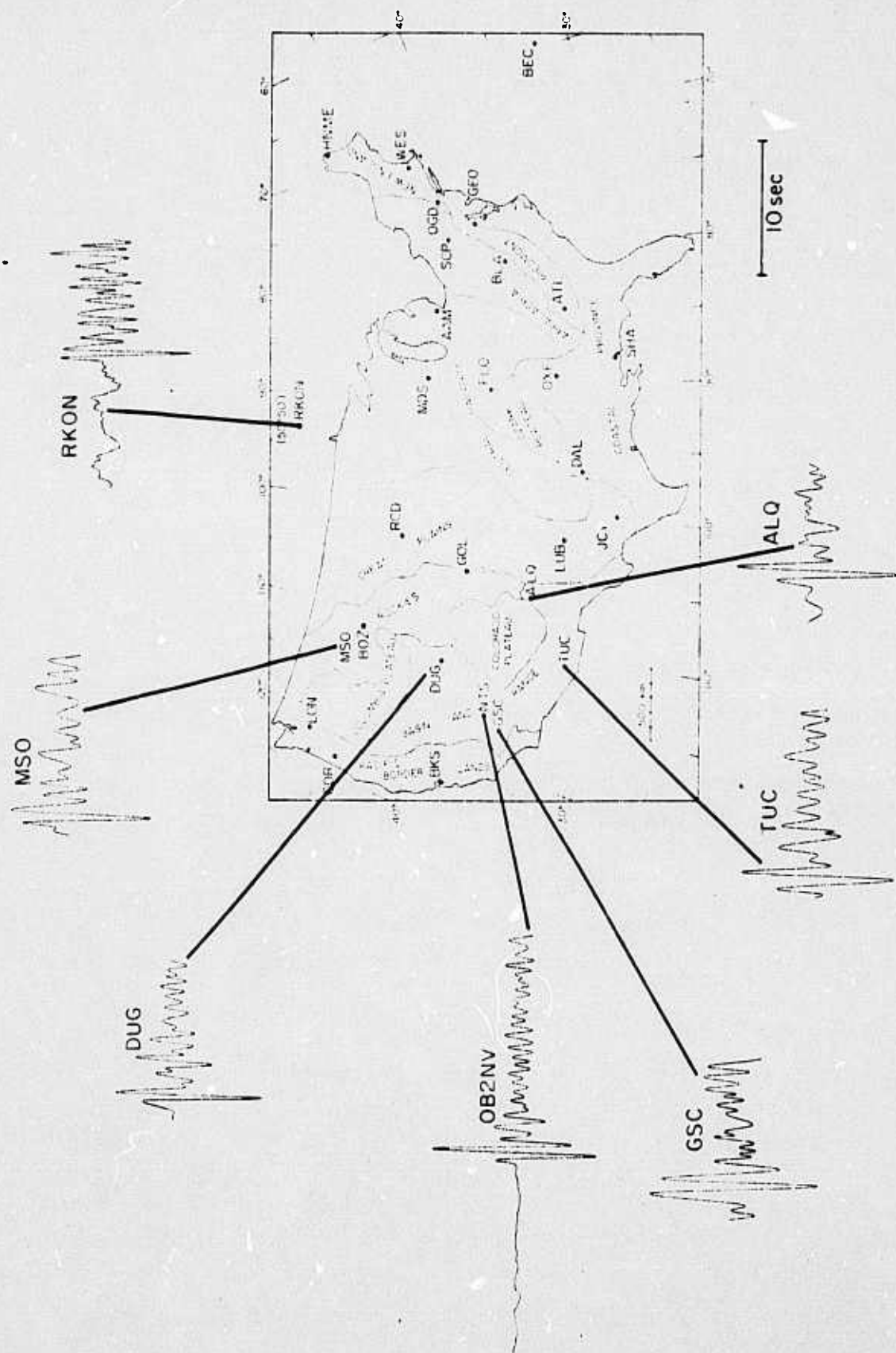


Figure 38. WSSN seismograms and filtered SDCS seismograms for a deep-focus event in Japan occurring on June 12, 1977. The noise level at station GSC was somewhat larger than usual for this event.

greater than the other stations shown in the figure. A systematic study of the waveforms observed at RKON indicated that this station occasionally shows anomalously different frequency content than other WWSSN or SDCS stations used in this study. Figure 37 plots an intermediate-depth earthquake in South America which occurred on June 8, 1977. The event was simple and shows similar waveshapes at stations across the United States. Figure 38 plots a deep-focus earthquake located in Japan which occurred on June 12, 1977.

The following series of figures plot the amplitude data for the WWSSN and corrected SDCS stations. Figure 39 plots amplitude data obtained from explosions at the five Russian test sites. The data at each test site were averaged separately, and the mean for each site and each station are plotted in Figure 39. Amplitude data for the SDCS stations were obtained only from the Semipalatinsk east test site. Some of the WWSSN stations in the United States are located at distances from the Russian test sites as to be affected by the core-mantle boundary. Those stations which suffer from the effects of diffraction at the core-mantle boundary have not been plotted in this study or included in the analysis of relative station amplitudes. Figure 40 plots the mean and standard error of the mean for all of the explosion data from the Russian test sites. The vertical scale in the plot is a logarithmic scale ranging from $1/10$ of the mean to a factor of 10 greater than the mean. The stations listed horizontally are arranged in roughly a west to east arrangement. This format is utilized in all figures of this type in this section. The solid line in the center of the graph represents the geometric mean of all the stations used in the study. Station OB2-NV (listed as OB2N) shows slightly greater amplitudes than the

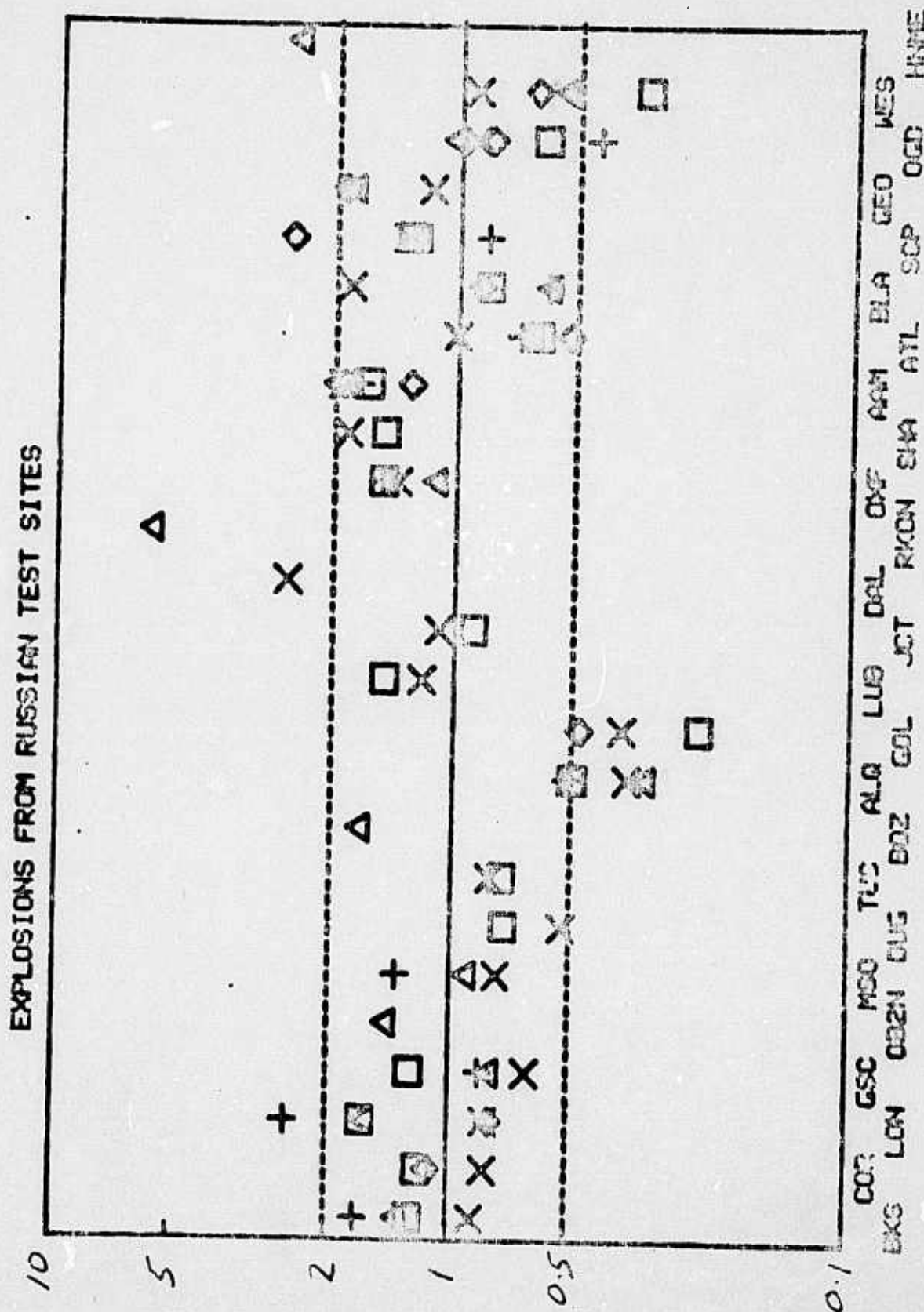


Figure 39. Amplitude data for WSSN and SDCS stations for explosions from five Russian test sites. Vertical scale is a logarithmic scale, the horizontal bar in center of the graph indicates the mean of the data in the United States. The stations listed on the abscissa are arranged in west to east order. Box = SNZ, X = NNZ, Diamond = KAZ, Triangle = Semi E, Cross = Semi W.

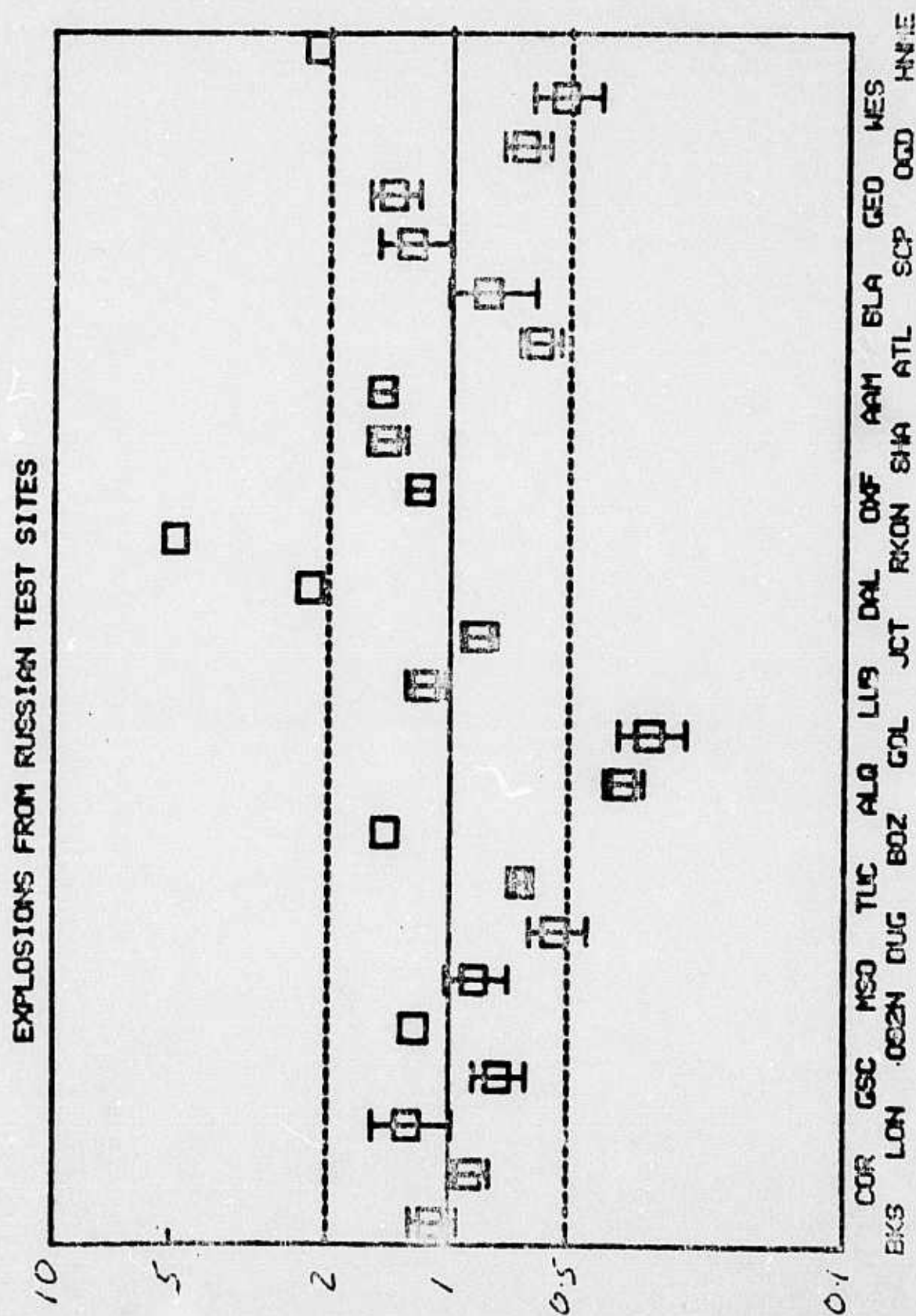


Figure 40. The mean and standard error of the mean of the data plotted in Figure 39 are shown.

mean. RKON shows amplitudes that are nearly a factor of 5 greater than the mean and HNME shows amplitudes roughly a factor of 2 greater than the mean. Figure 41 plots earthquake data from the northwest azimuth. The data show greater scatter than the explosion data, but the means for each source region are well determined. Figure 42 plots the mean and standard error of the mean of the data shown in Figure 41. Station OB2-NV shows a value slightly lower than the mean: RKON shows a value approximately a factor of 2 greater than the mean and HNME shows a value at the mean. Figure 43 plots data from South American earthquakes. The mean and standard error of the mean of these data are plotted in Figure 44. Station OB2-NV shows a value slightly greater than the mean. Table 6 shows the mean, standard error of the mean, and the number of determinations in the calculations for each station for a northern azimuth to the Russian test sites. It should be noted that N in this case indicates the number of test sites utilized in the determination of the mean. As the primary SDCS data were obtained only for the Semipalatinsk east site, a separate listing is indicated in Table 7 for this test site alone. It should be noted that diffracted data is included in this list and that the mean of these data will be different than the mean for all of the Russian test sites that exclude the diffracted data. The P-waves measured at the SDCS stations for this test area are not diffracted and the relative mean amplitudes are not affected by the more distant, diffracted arrivals. Tables 8 and 9 list the mean, standard error of the mean, and number of data used for earthquakes located along azimuths to the northwest and earthquakes from South America, respectively.

Before comparisons of a more quantitative nature can be considered, effects due to differences in the geologic siting of the stations must be evaluated. Gutenberg (1956, 1957) and Borchardt (1970) have noted that

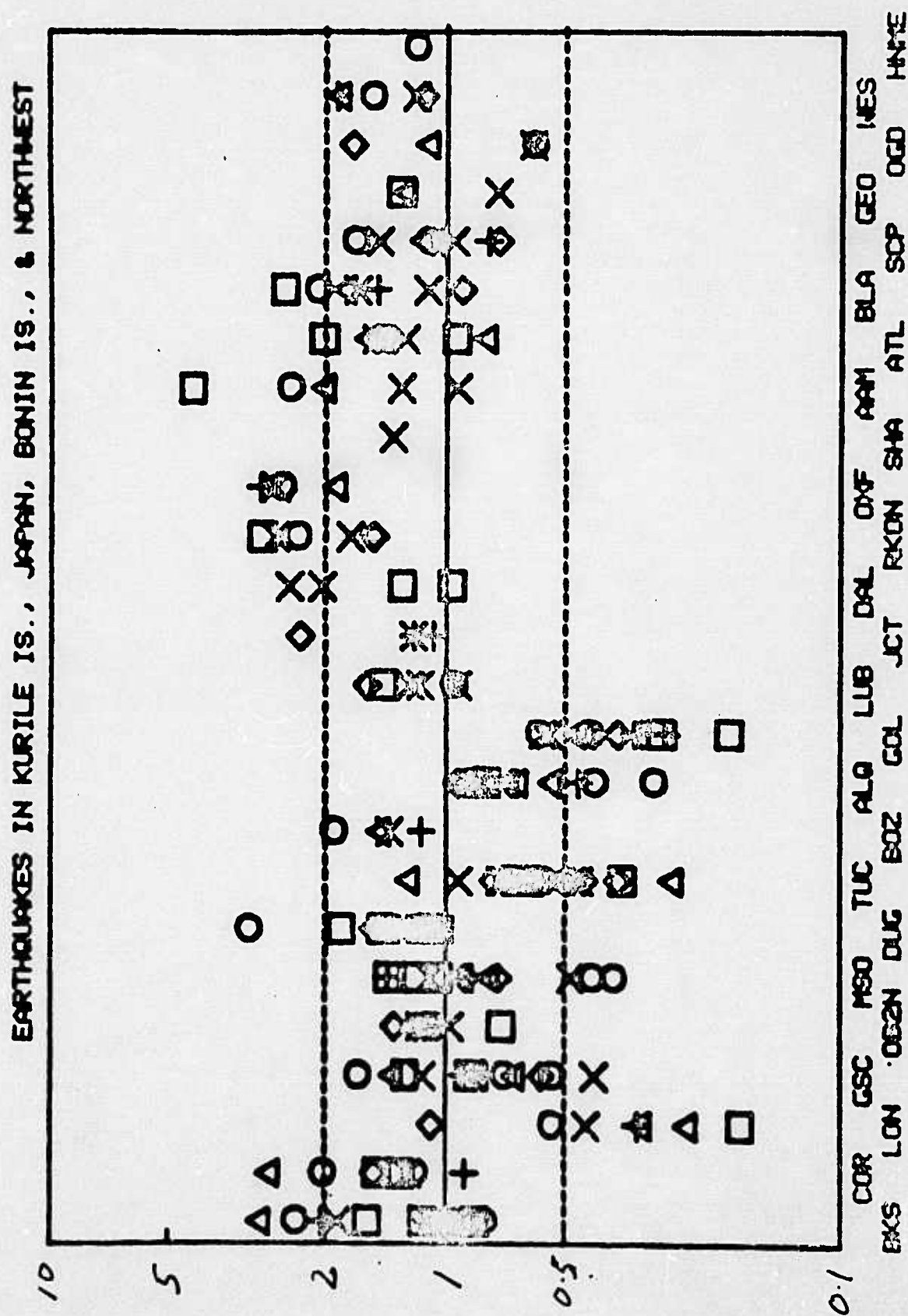


Figure 41. Relative amplitude data from earthquakes in the Kurile Islands region and other areas of Northeast Asia are plotted relative to the mean value in the United States represented by the solid line.

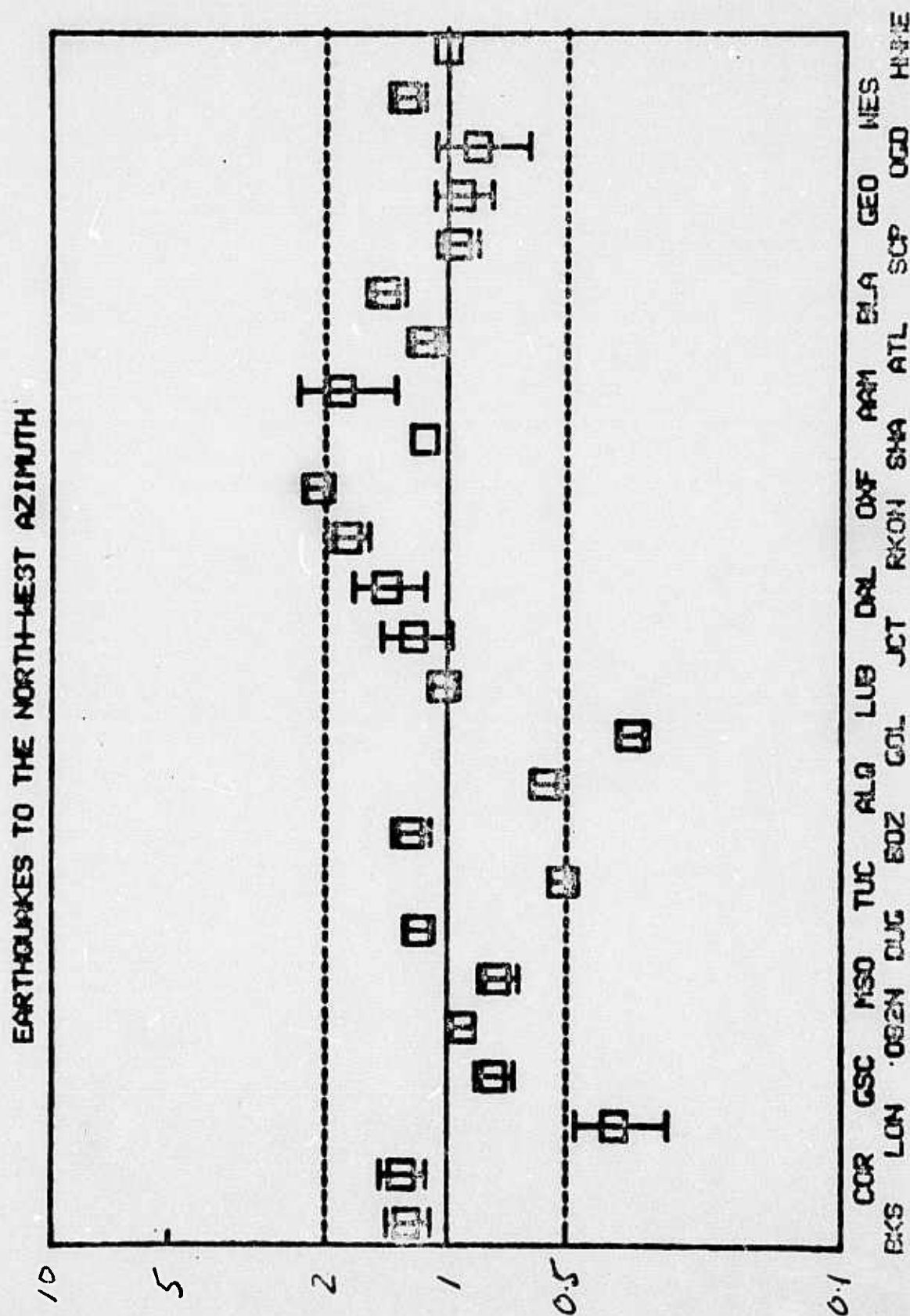


Figure 42. The mean and standard error of the mean are shown for the data in Figure 47.

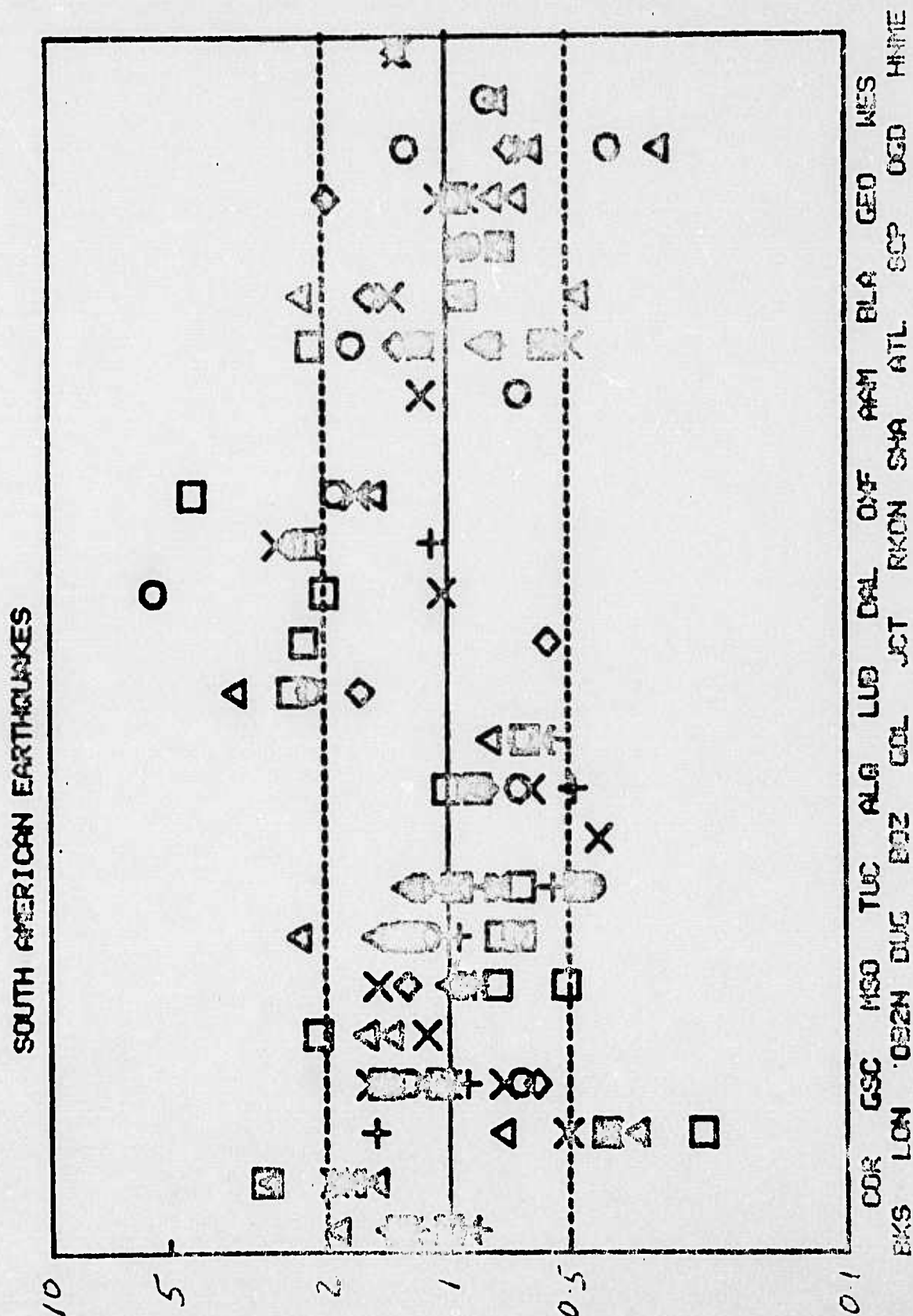


Figure 43. Relative amplitude data from South American earthquakes are plotted relative to the mean value observed in the United States - the solid line.

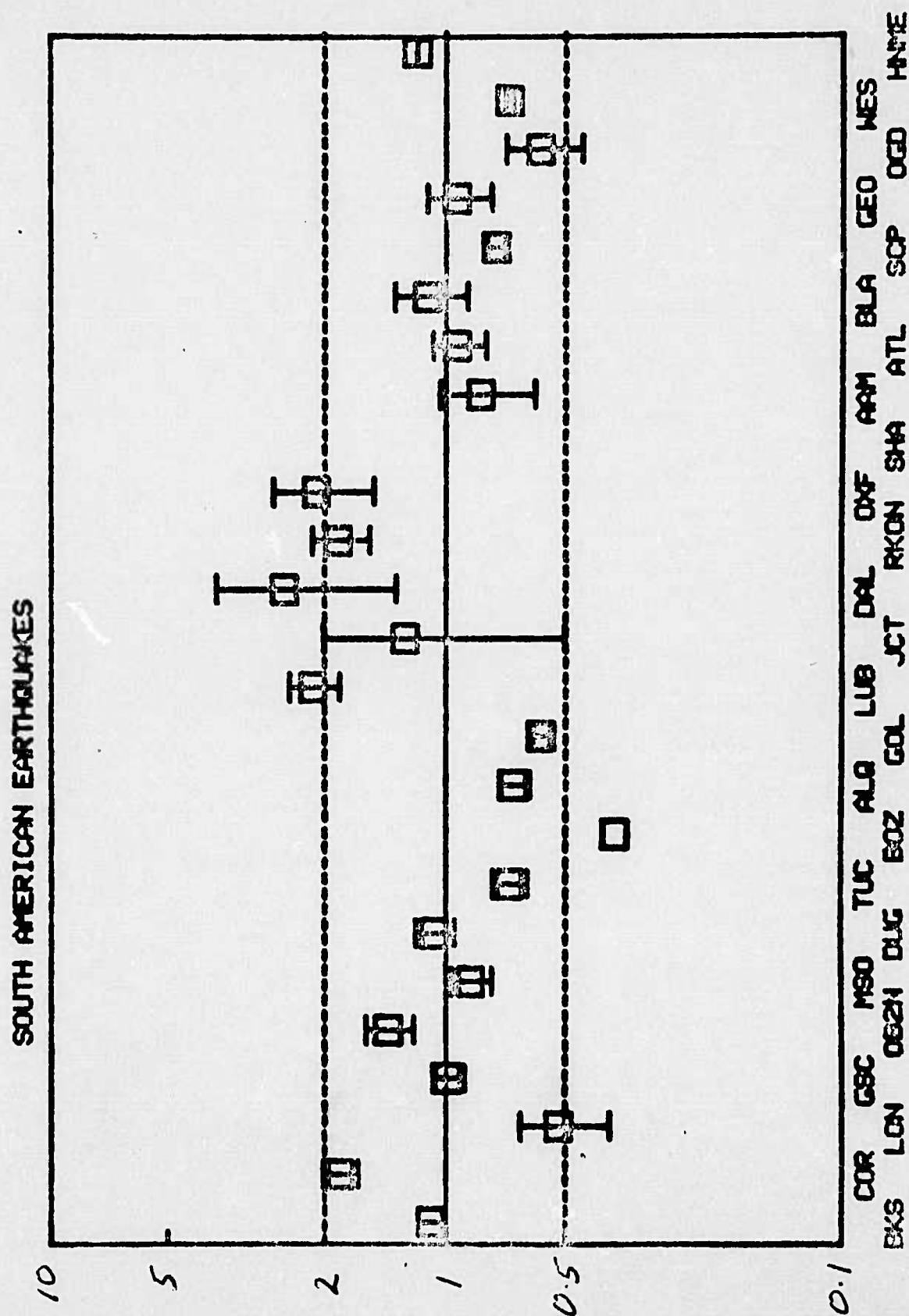


Figure 44. The mean and standard error of the mean of the data from Figure 43 are plotted.

Table 6
Five Russian Test Sites

<u>STATION</u>	<u>MEAN</u>	<u>S.E.M.</u>	<u>N</u>
BKS	1.10	0.14	4
COR	0.89	0.10	3
LON	1.27	0.29	5
GSC	0.75	0.11	4
OB2NV	1.22		1
MSO	0.87	0.16	3
DUG	0.54	0.09	2
TUC	0.66	0.02	2
BOZ	1.44		1
ALQ	0.37	0.04	4
GOL	0.32	0.06	3
LUB	1.15	0.12	2
JCT	0.85	0.08	2
DAL	2.23		1
RKON	4.89		1
OXF	1.19	0.08	4
SHA	1.44	0.15	2
AAM	1.48	0.10	5
ATL	0.60	0.07	5
BLA	0.81	0.20	5
SCP	1.26	0.25	5
GEO	1.40	0.20	3
OGD	0.65	0.09	5
WES	0.52	0.10	4
HNME	2.14		1

The amplitude response of the SDCS station HNME.

Table 7

Semipalitinsk East Including Additional Events

<u>STATION</u>	<u>MEAN</u>	<u>S.E.M.</u>	<u>N</u>
BKS	1.26	0.05	8
COR	3.26	0.50	8
LON	1.52	0.06	5
GSC	0.77	0.03	7
OB2NV	1.34		1
MSO	0.82	0.05	5
DUG	2.83	0.12	3
TUC	0.15	0.01	8
BOZ	1.47		1
ALQ	0.32	0.02	8
GOL	0.89	0.04	7
LUB	0.67	0.05	3
JCT	0.12	0.03	4
DAL	1.21	0.13	2
RKON	5.75	0.37	3
OXF	1.14	0.13	3
SHA			
AAM	1.90	0.18	6
ATL	0.62	0.03	6
BLA	0.59	0.05	9
SCP	1.16	0.09	5
GEO	1.69	0.21	5
OGD	0.99	0.05	8
WES	0.53	0.05	4
HNME	2.38	0.02	2

Table 8

All Earthquakes to Northwest

STATION	MEAN	S.E.M.	N
BKS	1.26	0.16	13
COR	1.30	0.17	8
LON	0.38	0.10	7
GSC	0.76	0.09	13
OB2NV	0.91	0.06	7
MSO	0.75	0.09	12
DUG	1.18	0.10	17
TUC	0.51	0.04	19
BOZ	1.24	0.13	4
ALQ	0.57	0.05	12
GOL	0.34	0.03	12
LUB	1.02	0.09	6
JCT	1.22	0.24	4
DAL	1.42	0.28	4
RKON	1.77	0.20	6
OXF	2.09	0.18	4
SHA	1.14		1
AAM	1.84	0.49	5
ATL	1.14	0.11	8
BLA	1.44	0.16	8
SCP	0.95	0.11	7
GEO	0.92	0.15	3
OOD	0.85	0.22	4
WES	1.27	0.13	5
HNME	1.00		1

Table 9
South American Earthquakes

STATION	MEAN	S.E.M.	N
BKS	1.09	0.08	10
COR	1.83	0.18	7
LON	0.52	0.13	8
GSC	0.99	0.09	12
DB2NV	1.39	0.18	4
MSO	0.87	0.10	8
DUG	1.07	0.12	12
TUC	0.69	0.07	14
BOZ	0.38		1
ALQ	0.68	0.06	7
GOL	0.58	0.03	6
LUB	2.15	0.31	4
JCT	1.26	0.76	2
DAL	2.53	1.20	3
RKON	1.85	0.30	4
OXF	2.10	0.59	4
SHA			
AAM	0.81	0.22	2
ATL	0.94	0.14	11
BLA	1.11	0.23	6
SCP	0.75	0.04	5
GEO	0.94	0.17	6
QGD	0.58	0.12	6
WES	0.69	0.02	3
HNME	1.18	0.00	2

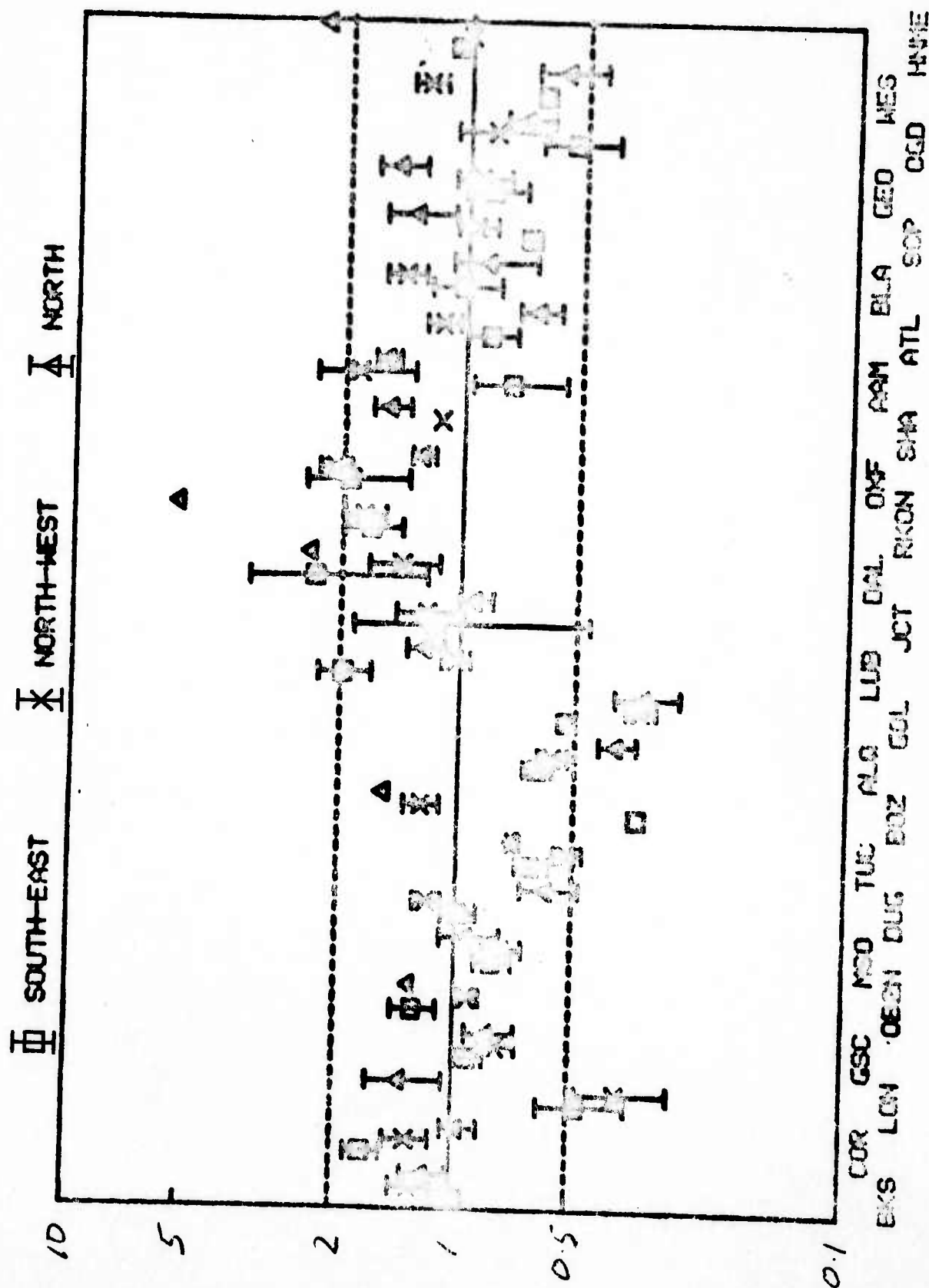


Figure 45. A composite plot of the data from Figures 40, 42, and 44.

stations situated on low velocity sediments are amplified relative to nearby stations situated on bedrock. Booth, et al. (1974) invoked sediment amplification to explain high magnitude residuals for long period LRSM stations along the Gulf coast. This sediment amplification effect is illustrated in Figure 21. The receiver effect of a variety of different sediment structures overlying bedrock are compared with simple bedrock site (upper left) using Thompson-Haskell propagator matrices and a synthetic explosion waveform assuming Poisson's ratio for the shear velocity and a 0.2 g/cm^3 bedrock-sediment density contrast. Sediment thickness of 300 meters show appreciable amplification. Near surface P wave velocities of 2 km/sec amplify a factor 1.6 to 1.8 relative to bedrock; surface velocities of 3 km/sec amplify by 1.4 to 1.5. As stations in the central United States (from RCD to AAM) are situated on slower sedimentary materials in contrast to the hard rock siting of the west and eastern coastal stations, some amplitude corrections must be made. The handbook of the WWSSN contains a short description of the local geology at each station: RCD, 2700 feet of shale, sandstone, and some limestone; LUB, Pliocene terrestrial deposits; JCT, Cretaceous Edwards limestone; FLO, 50 to 60 feet of recent clay overlying Mississippian bedrock; OXF, 2100 feet of Cenozoic and Mesozoic sediments; SHA, sands and gravels of Plio-Pleistocene age underlain by clays and sand of Miocene age; AAM, 200 feet gravel, 800 feet of shale, 4800 feet of limestone. Composing a velocity section from the geologic descriptions is pretty much creative guesswork. Shallow lying sandstones and shales have compressional velocities from 1.4 to 3.3 km/sec. Limestones velocities are sensitive to the extent of crystallization and range between 1.7 and 6.1 km/sec. Seismic refraction surveys provide only general control as sediments are grouped in a single layer characterized by the highest velocity arrival. Well log velocity depth

data provide the only accurate control, but such information was obtainable only from SHA. The lower right velocity-depth section in Figure 21 was simplified from a well log 25 km from SHA, and shows a factor of 1.8 amplification relative to bedrock. Given the lack of velocity control in the surface layers at RCD, LUB, JCT, DAL, and AAM, only an approximate sediment amplification correction of a factor of 1.4 to 1.8 may be estimated.

Figure 45 summarizes the amplitude data obtained in this study. These data are uncorrected for the sedimentary amplification effects discussed above. Data from three azimuths are all plotted on the same figure to illustrate the extent of variations observed in the data. The SDCS station at OB2-NV shows a value that averages slightly greater than the mean value of all data. RKON on the other hand shows values that are consistently greater than the mean value. HNME shows values from the north which are larger than the mean but shows values similar to the mean for earthquakes from the northwest or south. These data are replotted in Figure 46 relative to station location and physiographic provinces in the United States. The symbol size indicates the amplitude factor greater or less than the mean. Upward pointing triangles indicate values greater than the mean, downward pointing triangles indicate values less than mean. The location of the triangle relative to the point indicating the station represents the azimuth to the events used in the study.

In summary, a collection of 36 nuclear explosions from the Soviet Union, 22 simple earthquakes from the Kurile Islands and surrounding regions of northeast Asia and 16 simple earthquakes in South America have been studied to obtain relative amplitude patterns for WWSSN stations in the United States. SDCS stations at OB2-NV, RKON and HNME were analyzed and tied to the amplitude patterns observed for the WWSSN stations by using a

SHORT PERIOD P WAVE AMPLITUDE ANOMALIES

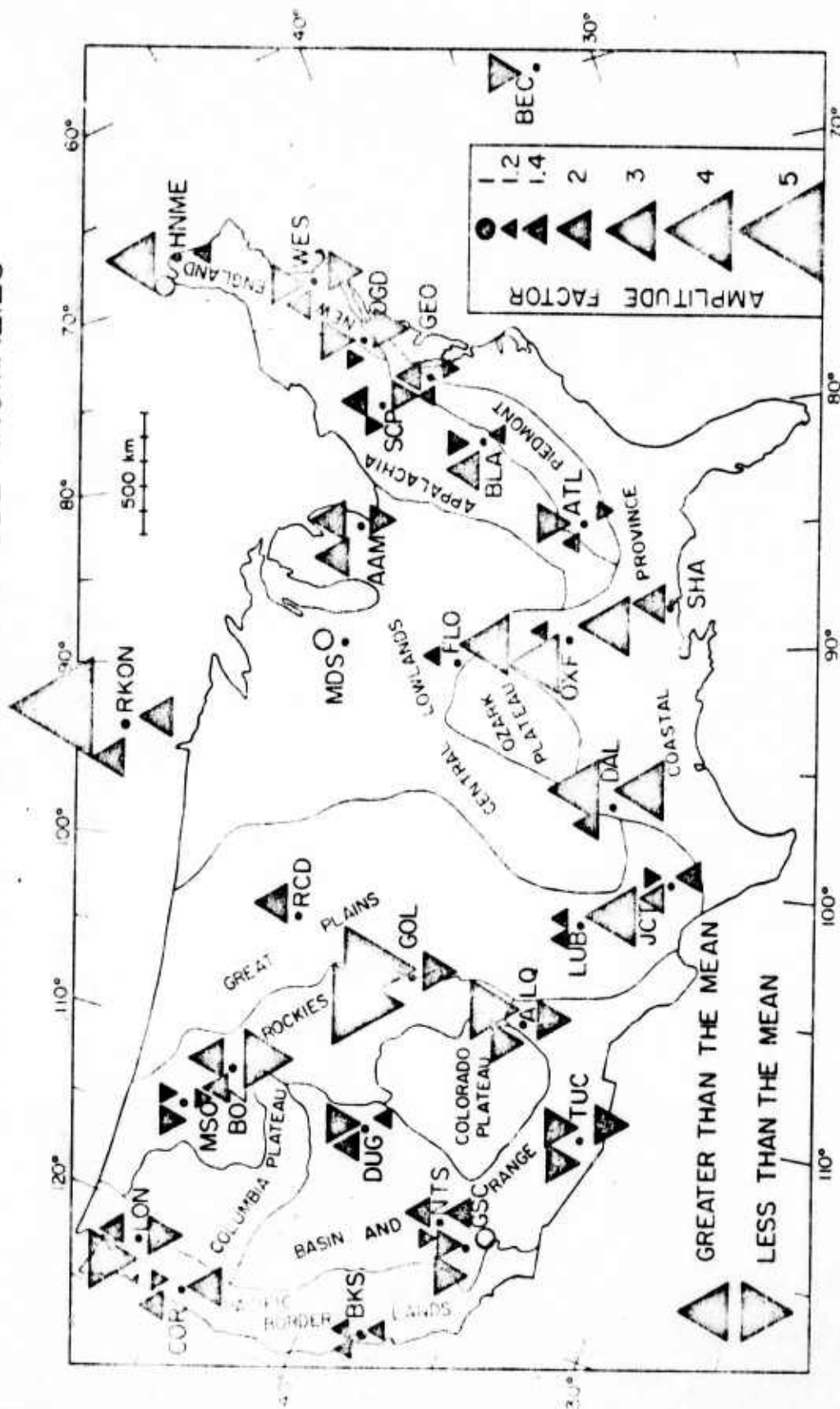


Figure 46. Short period P-wave amplitude anomalies are plotted relative to station location and approximate physiographic provinces within the United States. Upward pointing triangles are values greater than the mean, downward pointing triangles are values less than the mean. A circle indicates a mean amplitude. The amplitude factor relative to the mean is noted at the lower right. The position of each triangle relative to each station, indicates azimuth: north, northwest and southeast.

subset of the explosion and earthquake data. The results indicate that station OB2-NV at the Nevada Test Site shows amplitudes that are systematically slightly greater than the mean amplitude in the United States for sources in the Soviet Union or earthquakes in South America and shows amplitudes that are slightly smaller than mean for earthquakes in northeast Asia. RKON shows amplitudes that are consistently greater than the mean for all azimuths, and are significantly greater by a factor of five for explosions at the Semipalatinsk east test site. Station HNME shows amplitudes which are very near the mean for earthquakes from the northeast and from South America and shows amplitudes about a factor of two greater than the mean value observed in the United States for explosions at the Semipalatinsk.

References

- Alewine, R. W., G. B. Young, D. L. Springer and R. W. Klepinger (1977).
Teleseismic P-wave magnitude-yield relations for well-coupled
Nevada Test Site explosions. AFTAC-TR-77-22 (SECRET).
- Anderson, D. L. and R. S. Hart (1978). The Q of the earth, J. Geophys. Res., 83, 58-69.
- Anderson, D. L. and R. S. Hart (1978). Attenuation models of the earth,
Physics of the Earth and Planetary Interiors, 16, 289-306.
- Anderson, D. L., H. Kanamori, R. S. Hart, and H-P Liu (1977). The earth
as a seismic absorption band, Science, 1104.
- Booth, D. C., Marshall, P. D., and J. B. Young (1974) Long and short
period P-wave amplitudes from earthquakes in the range 0° - 114° ,
Geophys. J. R. Astr. Soc., 39, 523-537.
- Borcherdt, R. D (1970). Effects of local geology on ground motion near
San Francisco Bay, Bull. Seism. Soc. Am., 60, 29-61.
- Butler, R. (1979). An amplitude study of Russian nuclear events for
WWSSN stations in the United States, AFOSR Quarterly Technical
Report, Sierra Geophysics, Inc. SGI-R-79-001.
- Dahlman, O. and H. Israelson (1977). "Monitoring Underground Nuclear
Explosions", Elsevier, New York, 440.
- Der, Z. A. and T. W. McElfresh (1975). Short period P-wave attenuation
along various paths in North America as determined from P-wave
spectra of the Salmon explosion, Teledyne Geotech., Report No.
SDAC-TR-75-16.
- Evernden, J. F. and D. M. Clark (1970). Study of teleseismic P. II
amplitude data, Phys. Earth Planet. Int., 4, 24-31.

- Gutenberg, B. (1956). Effects of ground on shaking in earthquakes, Transactions, A.G.U., 37, 757-760.
- Gutenberg, B. (1957). Effects of ground on earthquake motion, Bull. Seism. Soc. Am., 47, 221-250.
- Hadley, D. M. (1979). Seismic source functions and attenuation from local and teleseismic observations of the NTS events Jorum and Handley, Sierra Geophysics, Inc. SGI-R-79-002.
- Hadley, D. M. and R. S. Hart (1979). Seismic studies of the Nevada Test Site. Sierra Geophysics, Inc. SGI-R-79-003.
- Hart, R. S. (1977). "The distribution of seismic velocities and attenuation in the earth", Ph.D. Thesis, California Institute of Technology, p. 354.
- Hong, T. L. and D. V. Helmberger (1978). Glorified optics and wave propagation in non-planer structure, Bull. Seism. Soc. Amer., 68, 1313.
- Kanamori, H., and D. L. Anderson (1977). Importance of physical dispersion in surface-wave and free oscillation problems-review, Rev. Geophys. Space Phys., 15, 105.
- Liu, H-P, D. L. Anderson, and H. Kanamori (1976). Velocity dispersion due to anelasticity; implications for seismology and mantle composition. Geophys. J. R. Astr. Soc., 47, 41.
- Minster, J. B. (1978). Transient and impulse response of a one-dimensional linearly attenuating medium, Part I: Analytic results, Geophys. J. R. Astr. Soc., 52, 479-501.
- Peppin, W. A. (1974). "The cause of the body wave - surface wave discriminant between earthquakes and underground nuclear explosions at near-regional distances", Ph.D. Thesis, University of California at Berkeley.

- Springer, D. L. and R. L. Kinnaman (1971). Seismic source summary for U.S. underground nuclear explosions 1961-1970, Bull. Seism. Soc. Am., 61, 1073.
- von Seggern, D. and R. Blandford (1972). Source time functions and spectra for underground nuclear explosions, Geoph. J. Roy. Astr. Soc., 31, 83-98.
- Wiggins, R. A. (1978). Minimum entropy deconvolution, Geoexploration, 16, 21-35.